

THÈSE

En vue de l'obtention du : *DOCTORAT*

Structure de Recherche : Physique des Hautes Énergies- Modélisation et Simulation

Discipline : Physique

Spécialité : Physique mathématique et Information quantique

Présentée et soutenue le : 23/09/2023 par :

Hamid SAKHOUF

Quantum information processing with superconducting circuits :
realizing and characterizing quantum gates and algorithms in open quantum systems

JURY

Mohammed Loulidi	PES, Université Mohammed V, Faculté des sciences-Rabat.	Président/Rapporteur
Lahoucine Bahmad	PES, Université Mohammed V, Faculté des sciences-Rabat.	Rapporteur/Examineur
Abderrahim El Allati	PH, Université Abdelmalek-Essaadi, Faculté des sciences et techniques- Al-Hoceima	Rapporteur/Examineur
Mohammed DAOUD	PES, Université Ibn Tofail, Faculté des sciences-Kénitra.	Directeur de thèse
Rachid Ahl Laamara	PES, Université Mohammed V, Faculté des Sciences-Rabat.	Directeur de thèse

Année Universitaire : 2022/2023

☒ Faculté des Sciences, avenue Ibn Battouta, BP. 1014 RP, Rabat –Maroc

☎ 00212(0) 37 77 18 76, ☎Fax : 00212(0) 37 77 42 61 ; <http://www.fsr.um5.ac.ma>

DEDICATION

First and foremost, I want to express my deep appreciation to my family. I am immensely grateful to my parents, siblings, and extended family for their unwavering support, encouragement, and motivation throughout my academic journey. Their belief in me and their constant presence in my life were the driving forces behind the completion of this thesis.

In addition, I would also like to thank all members, past and present, of the LPHE-MS, with whom I have had the pleasure to interact, for the many valuable discussions and shared moments.

ACKNOWLEDGMENT

During the preparation of this thesis, many things changed in my life, both personally and scientifically. Before diving into the content of this thesis, I would like to express my gratitude and thanks to those who have been present in this period of my life and have contributed directly or indirectly to this final work.

*First, I would like to thank **Mr. El Hassan SAIDI** Professor at the Faculty of Science of Rabat for giving me the opportunity to enroll in a Master's degree in mathematical physics, which in turn allowed me to enroll in the Ph.D. program at the Laboratory of High Energy Physics, Modelisation, and Simulation (LPHE-MS). I appreciate their advice and encouragement throughout this work. My sincere thanks for their availability as well as the efforts they have always made for the success of several activities of the LPHE-MS.*

*In addition to the director of LPHE-MS laboratory, I would like to warmly thank my supervisor **Mr. Rachid AHL LAAMARA**, professor at the Faculty of Sciences of Rabat for welcoming me to the LPHE-MS. His continuous encouragement gave me the strength and courage to complete this thesis as well as for his teaching of the group theory course and Lie algebra course.*

*Additionally, I would like to warmly thank my supervisor **Mr. Mohammed DAOUD** Professor at faculty of science of Kenitra for his magnificent guidance throughout my graduate studies. Without him, this thesis would never have been possible. I appreciate his continuous support and guidance with formidable motivation and support in my studies for my Master's and Ph.D.*

*My regards also go to **Mr. Mohammed LOULIDI**, Professor at the Faculty of Science of Rabat, who accepted the presidency of the jury also agreeing to be a reporter of my modest work. I also acknowledge him for his help, discussion, encouragement, and motivation.*

*Let me also thank the rapporteurs of the thesis : I will start with **Mr. Lahoucine BAHMAD**, Professor at the Faculty of Science of Rabat. I would like to thank him warmly for accepting to be a reporter of my modest work. Yours sincerely.*

*My acknowledgment also goes to **Mr. Abderrahim El ALLATI**, PH, Faculty of Sciences*

and Techniques Al-Hoceima, for accepting to be the reporter of my thesis. I thank him for his interest and responsibility as an examiner of this work and for his bearing the hardships of traveling from Al-Hoceima to Rabat to be with the jury members.

RÉSUMÉ

Cette thèse se concentre sur le traitement de l'information quantique à l'aide d'un dispositif supraconducteur, en particulier sur la réalisation de portes quantiques et d'algorithmes dans des systèmes quantiques ouverts. Un tel dispositif est construit par des qubits supraconducteurs de type transmon couplés à un résonateur supraconducteur. Pour la réalisation des portes quantiques et des algorithmes, une approche en une seule étape est utilisée. Nous proposons des schémas plus rapides et plus efficaces pour réaliser des portes de X -rotation et des portes d'enchevêtrement pour deux et trois qubits. Au cours de ces opérations, le nombre de photons du résonateur est annulé en raison du fort champ de micro-ondes ajouté. Elles ne nécessitent pas que le résonateur soit initialement préparé dans l'état de vide et les schémas sont insensibles à la désintégration du résonateur. En outre, la robustesse de ces opérations est démontrée en incluant l'effet de la décohérence des systèmes transmon et la désintégration du résonateur dans une équation maîtresse, ce qui permet d'obtenir une grande fidélité dans la simulation quantique. En outre, en utilisant les portes de X -rotation mises en œuvre ainsi que les portes de phase, nous présentons une autre façon de mettre en œuvre l'algorithme de Grover pour deux et trois qubits qui ne nécessite pas une série de portes simples. En outre, nous démontrons en simulant numériquement l'utilisation de la tomographie des processus quantiques pour caractériser pleinement la performance d'une porte d'enchevêtrement à un seul coup pour deux et trois qubits et nous obtenons des fidélités de processus supérieures à 93%. Ces portes sont utilisées pour créer des états intriqués de Bell et de Greenberger-Horne-Zeilinger (GHZ).

Mots clés : Traitement de l'information et calcul quantique, Portes quantiques, Algorithme de recherche de Grover, Portes d'intrication, États de Bell et GHZ, circuits supraconducteurs, Haute fidélité.

ABSTRACT

This thesis focuses on quantum information processing using the superconducting device, especially, on realizing quantum gates and algorithms in open quantum systems. Such a device is constructed by transmon-type superconducting qubits coupled to a superconducting resonator. For the realization of quantum gates and algorithms, a one-step approach is used. We suggest faster and more efficient schemes for realizing X -rotation and entangling gates for two and three qubits. During these operations, the resonator photon number is canceled owing to the strong microwave field added. They do not require the resonator to be initially prepared in the vacuum state and the scheme is insensitive to resonator decay. Furthermore, the robustness of these operations is demonstrated by including the effect of the decoherence of transmon systems and the resonator decay in a master equation, and as a result high fidelity will be achieved in quantum simulation. In addition, using the implemented x -rotation gates as well as the phase gates, we present an alternative way for implementing Grover's algorithm for two and three qubits, which does not require a series of single gates. As well, we demonstrate by a numerical simulation the use of quantum process tomography to fully characterize the performance of a single-shot entangling gate for two and three qubits and obtaining process fidelities greater than 93%. These gates are used to create Bell and Greenberger-Horne-Zeilinger (GHZ) entangled states.

Keywords : Quantum information processing and computation, Quantum gates, Grover's search algorithm, Entangling gates, Bell and GHZ states, High fidelity, superconducting circuits.

RÉSUMÉ DÉTAILLÉ

Cette thèse se concentre sur la réalisation et la caractérisation de portes quantiques et d'algorithmes à l'aide d'une approche en une seule étape basée sur un dispositif quantique supraconducteur. Un tel dispositif quantique est construit en couplant des qubits supraconducteurs de type transmon à un résonateur supraconducteur, piloté par un champ classique. À l'aide de ce dispositif, nous proposons un schéma rapide pour préparer un registre quantique comprenant de nombreux états de base en superposition quantique en réalisant la porte de rotation X pour deux qubits ou plus, ne nécessitant qu'une seule opération. De plus, en utilisant la même approche, nous réalisons la porte d'intrication en une seule étape pour deux qubits ou plus. Ces portes sont utilisées pour créer un état totalement intriqué tel qu'un état de Bell à deux qubits et un état GHZ à trois qubits. En utilisant une simulation strictement numérique basée sur des hypothèses réalistes concernant les paramètres du système, nous étudions la dynamique quantique de ces portes et démontrons que ces schémas peuvent être mis en œuvre avec une grande fidélité.

De plus, en utilisant les portes de rotation X mises en œuvre, nous présentons une alternative pour mettre en œuvre l'algorithme de Grover à deux et trois qubits, qui ne nécessite pas une série de portes individuelles. Notre implémentation a montré que le schéma proposé permet de trouver efficacement l'état correct avec une fidélité élevée d'environ 90%. Ces schémas présentent les avantages suivants : (i) ils ne nécessitent pas la combinaison des portes de base, par exemple les portes individuelles et à deux qubits, (ii) le résonateur n'a pas besoin d'être initialement préparé dans l'état de vide, (iii) nos schémas sont insensibles à la dégradation de la cavité, ce qui facilite les expériences pratiques. De plus, nous démontrons, en simulant numériquement l'utilisation de la Tomographie du Processus Quantique (TPQ) pour caractériser pleinement les performances d'une porte d'interaction en une seule étape pour deux qubits ou plus, que nous obtenons des fidélités de processus supérieures à 93%.

Dans le premier chapitre, nous discuterons brièvement des bases du traitement et du calcul de l'information quantique. Cela comprend les aspects mathématiques et géométriques des bits quantiques, ainsi que la description de la façon dont ils peuvent être manipulés et de la différence entre un ordinateur quantique et son équivalent classique. Nous identifierons également un ensemble universel de portes logiques quantiques, comprenant des portes individuelles et multi-

qubits, ainsi que leur contribution à la construction d'algorithmes quantiques, tels que les algorithmes de Grover et Deutsch-Jozsa, les protocoles d'intrication quantique et la préparation d'états de superposition. Dans le deuxième chapitre, nous aborderons la mise en œuvre physique des bits quantiques en utilisant des circuits électriques pour réaliser des qubits supraconducteurs. Nous passerons en revue certains types de qubits tels que la boîte à paires de Cooper (qubit de charge) et le qubit transmon qui est utilisé dans cette thèse, ainsi que l'oscillateur LC harmonique quantique en tant que composant essentiel dans électrodynamique quantique en circuit (circuit QED). Nous décrirons également l'interaction entre les qubits supraconducteurs et la ligne de transmission supraconductrice ou l'oscillateur LC (le champ électromagnétique) à l'intérieur de la cavité de la QED des circuits, qui est une version similaire de l'électrodynamique quantique en cavité (cavité QED) classique qui sera également abordée. De plus, nous discuterons du régime dispersif nécessaire pour le traitement de l'information quantique. Enfin, nous terminerons ce chapitre en associant la circuit QED au traitement de l'information quantique, où nous identifierons les portes à qubit unique, ainsi que les portes C-Phase et iSWAP. Le chapitre III de cette thèse vise à réaliser la porte de rotation X pour deux et trois qubits, qui peut être utilisée pour préparer des états de superposition et d'autres portes appelées portes d'intrication, utilisées pour générer des états totalement intriqués tels que les états de Bell et GHZ. Leur mise en œuvre est basée sur un dispositif quantique comprenant des qubits transmon couplés capacitivement à un résonateur, piloté par un champ micro-onde, en utilisant une approche en une seule étape. La robustesse de ces portes est démontrée en prenant en compte l'effet de la décohérence des systèmes transmon et de la dégradation du résonateur dans un formalisme d'équation maîtresse. Pour des hypothèses réalistes concernant les paramètres du système transmon- résonateur, une grande fidélité sera obtenue lors de la simulation quantique. Au cours de ces opérations, le nombre de photons du résonateur est annulé en raison du fort champ de micro-ondes ajouté. Elles ne nécessitent pas que le résonateur soit initialement préparé dans l'état de vide et les schémas est insensible à la désintégration du résonateur. Enfin, nous discuterons de la faisabilité expérimentale des schémas proposés et les comparerons aux derniers résultats expérimentaux dans le domaine des dispositifs supraconducteurs.

Mots clés : Traitement de l'information et calcul quantique, Portes quantiques, Algorithme de recherche de Grover, Portes d'intrication, Etats de Bell et GHZ, circuits supraconducteurs, Haute fidélité.

LIST OF PUBLICATIONS

This thesis is based in part on the following published articles :

- Hamid Sakhouf, Mohammed Daoud, Rachid Ahl Laamara , “Quantum process tomography of the single-shot entangling gate with superconducting qubits,” [Journal of Physics B: Atomic, Molecular and Optical Physics](#) **56**, 105501 (2023).
- Hamid Sakhouf, Mohammed Daoud, Rachid Ahl Laamara , “Simple scheme for implementing the Grover search algorithm with superconducting qubits,” [Journal of Physics B: Atomic, Molecular and Optical Physics](#) **54**, 175501 (2021).
- Hamid Sakhouf, Mohammed Daoud, Rachid Ahl Laamara , “Implementation of Grover’s Search Algorithm in the QED Circuit for Two Superconducting Qubits,” [International Journal of Theoretical Physics](#) **59**, 3436–3448 (2020).

TABLE DES FIGURES

I.1	Bloch sphere representation of a qubit.	8
I.2	Quantum circuit representation for CNOT gate. Here $x, y = 0$ or 1 and \oplus denotes the addition modulo 2, while the vertical line between the control and target qubit represents the circuit diagram of CNOT gate.	13
I.3	Quantum circuit for creating the Bell state.	16
I.4	Quantum circuit for creating the GHZ state.	16
I.5	Quantum circuit for evaluating $f(x)$. U_f is the quantum circuit which transforms input states $ x\rangle_n y\rangle_m$ to $ x\rangle_n y \oplus f(x)\rangle_m$	17
I.6	Evolution of amplitudes for each state during the Grover search algorithm.	19
I.7	Geometric representation of Grover's algorithm for a single Grover iteration, G . . .	20
I.8	Quantum circuit implementing the general Deutsch-Jozsa algorithm.	22
II.1	Schematic of a Josephson tunnel junction. It consists of two superconductors separated by an insulating barrier. The two sides of the junction are characterized by the number of Cooper pairs n_1, n_2 and the phases θ_1, θ_2 . The charge $n_2 - n_1$ and phase difference $\theta_2 - \theta_1$ between the two metals are the essential parameters describing the behavior of the junction.	24
II.2	Schematic of a Josephson tunnel junction. (a) The symbol of the Josephson junction (Cross in a box) .(b) The equivalent electrical circuit of the Josephson junction. . .	25
II.3	Schematic of a SQUID. The two Josephson junctions form a loop, which is crossed by a flux magnetic field.	26

II.4	a) Schematic of the Cooper pair box consisting of a Josephson junction (blue) which connects an island (green) with a reservoir (orange). b) The Josephson junction is replaced by a SQUID in which the qubit becomes more controllable by a magnetic flux.	28
II.5	a) Circuit diagram corresponding to the Cooper pair box schematic in Fig. (II.4a). b) Circuit diagram corresponding to the Cooper pair box schematic in Fig. (II.4b).	28
II.6	Energy spectrum of the charge qubit for the ratio as a function of gate charge N_g . The E/E_C is lower, the first two levels are isolated from the third for values of N_g near the half-integer. a) the bold curve designates the energy spectrum of the Hamiltonian with $E_C = 0.2$, the fine curve with $E/E_C = 0$. b) the energy spectrum for $0 \leq N_g \leq 1$	31
II.7	The equivalent circuit of the Transmon qubit, an additional capacitance (Cs) has been added in parallel to the junction.	32
II.8	Eigenenergies for three energy levels ($k = 0, 1, 2$) of the Cooper pair box Hamiltonian (II.31) for different ratios E_J/E_C . For very large E_J/E_C , the spectrum practically becomes that of the harmonic oscillator. The system gets less sensitive to gate charge when the E_J/E_C is increased from the charging regime with $E_J/E_C = 0.5$ (a) to the transmon regime with $E_J/E_C = 50$ (c). The figure used from Ref.[66].	33
II.9	QED cavity architecture includes an electromagnetic field mode of decay rate κ coupled to a two-level system of decay rate γ and the transition time $t_{transit}$ with a coupling force g	35
II.10	An electromagnetic cavity of length L , the electric field must therefore be zero at the extremities of the cavity.	36
II.11	Two level atom.	37
II.12	Energy diagram in the resonant case.	39
II.13	Energy diagram in the dispersive regime.	40
II.14	Energy diagram in the dispersive regime.	41
II.15	Representation of the transmission line by a set of inductors in parallel with capacitors.	42
II.16	Representation of an inductor in parallel with the capacitor.	43
II.17	Circuit QED for the transmon qubit : (a) The transmon qubit is coupled to the LC resonator through a gate capacitance C_d . The two Josephson junctions, with capacitance C_J and Josephson energy E_J , are in parallel with an additional large capacitance C_B . (b) The transmon device consists of a transmon qubit coupled to a transmission line. The figure used from Ref.[43].	44

III.1	Electrical circuit diagram of a three-qubit device[119].	52
III.2	(Color online) (a) Fidelity of the two-qubit X -rotation gate as a function of the decay rate of resonator κ (a) and as a function of the coherence time T (b). The blue solid line means that our calculation was performed by using the Hamiltonian (III.7) for $j=1,2$, while the calculation referred to by the solid line was performed using the Hamiltonian (III.11) for $j=1,2$. The system parameters used in the numerical simulation are mentioned in the text.	60
III.3	(Color online) (a) Fidelity of the three-qubit X -rotation gate for different values of the cavity decay rate κ (a) and initial cavity Fock states $ n\rangle$ (b). The blue solid line means that our calculation was performed by using the Hamiltonian (III.7) for $j=1,2,3$, while the calculation referred by the solid line was performed using the Hamiltonian (III.11) for $j=1,2,3$. The system parameters used in the numerical simulation are the same as a figure (III.2) while the others are mentioned in the text.	63
III.4	(Color online) Simulated measurements of the single-shot entangling gate (Eq.III.35) (a) The occupation probabilities versus the interaction time. The system parameters used in the numerical simulation are $g/2\pi = 40$ MHz, $2\Omega_R = 9g$, $T_c = 20\mu s$, and $\kappa/2\pi = 1.5$ MHz. (b) Fidelity versus the number of the two-qubit entangling gates with environment decoherence under the Hamiltonian in equation (III.11) and without environment decoherence under the following Hamiltonian $H_{2I} = 2\Omega_R S_x + 2\lambda S_x^2$. The data parameters used are the same as in panel (b).	65
III.5	(Color online) (a) Quantum circuit for generating GHZ -state using the single-shot entangling gate(Eq.III.35) (b) The occupation probabilities as a function of the operation time T_m [132]. The system parameters used here are $g/2\pi = 20$ MHz, $2\Omega_R = 9g$, $T_c = 20\mu s$, and $\kappa/2\pi = 1.5$ MHz.	67
III.6	(Color online) (a) Numerical simulation of the fidelity as a function of the number of entangling gates under both Hamiltonians in equation (III.11) and H_{3I} . (b) A number of entangling operations of the error are caused by decoherence. ΔF denotes the difference of the fidelity for generating GHZ state with and without dissipation[132]. The data parameters used are the same as in figure (III.5a).	68
IV.1	Schematic circuit of a three-qubit Grover's algorithm[128].	72
IV.2	(Color online) The probability of finding the state after the first (a) and second (b) Grover's iteration.	73
IV.3	Schematic circuit of Grover's algorithm[128].	73
IV.4	Schematic circuit of the two-qubit Grover algorithm[128].	75

IV.5 Numerical results for the fidelities of two-qubit in Grover algorithm for the four possible oracles as the function $b = 2\lambda t$. These plots are drawn for $\Omega_R/\lambda = 13.5$ [128].	75
IV.6 Schematic circuit of the three-qubit Grover algorithm[119].	77
IV.7 Numerical results of the algorithm fidelity for the desired state $ 111\rangle$ versus $b = 2\lambda t$ for different values of $h = \Omega_R/\lambda$. Other parameters of the system are referred to in the text. (a) Fidelity F_1 for $O = cP_{000}$. (b) Fidelity F_2 for $O = cP_{001}, cP_{010}, cP_{101}$. (c) Fidelity F_3 for $cP_{011}, cP_{100}, cP_{110}$. (d) Fidelity F_4 for $O = cP_{111}$	78
IV.8 <i>QPT</i> of the single-shot two-qubit entangling gate. Absolute values of the matrix elements of the χ_{ideal} (a) and the χ_{sim} (b). The matrix elements are shown in the operator basis $\{I \otimes I, I \otimes X, I \otimes Y, ..., Z \otimes X, Z \otimes Y, Z \otimes Z\}$, where I is identity matrix and $\{X, Y, Z\}$ are the Pauli operators $\{\sigma_x, -i\sigma_y, \sigma_z\}$	81
IV.9 <i>QPT</i> of the single-shot entangling gate for three qubits. Absolute values of the matrix elements of the χ_{ideal} (a) and the χ_{sim} (b). The matrix elements are shown in the operator basis $\{I \otimes I \otimes I, I \otimes I \otimes X, ..., Z \otimes Z \otimes Y, Z \otimes Z \otimes Z\}$, where I is identity matrix and $\{X, Y, Z\}$ are the Pauli operators $\{\sigma_x, -i\sigma_y, \sigma_z\}$	83
IV.10 Performance of the single-shot entangling gate for three systems. Numerical simulation of the gate fidelity F_{mean} versus the coherence times $T \geq 0.6\mu s$. Assuming that $T = T_1 = T_2$, while the other system parameters are the same as in figure III.6. . . .	83

LIST OF ABBREVIATIONS

QIP	Quantum information processing
NMR	nuclear magnetic resonance
QED	quantum electrodynamics
CP or C-phase	conditional phase
GHZ	Greenberger-Horne-Zeilinger
CNOT	Controlled Not
QPT	Quantum process tomography
SQUID	superconducting quantum interference device
RWA	rotating wave approximation

LIST OF SYMBOLS

$i\text{SWAP}$	i-swap gate.
X, Y, Z	single-qubit Pauli operator, also defined as $\sigma_{x,y,z}$.
$\sqrt{i\text{SWAP}}$	square-root of i-swap gate.
$R_i(\theta)$	rotation around the axis i by angle θ .
H	Hadamard gate.
$Tofoli$	controlled-controlled-X gate.
$Fredkin$	controlled SWAP operation.
I_c	the critical current of the junction
Φ_0	the magnetic flux quantum
L	the Lagrangian of a Josephson junction
E_C	the charging energy of a Cooper pair
E_J	the Josephson tunneling energy
p	the canonical momentum operator
U_T	the potential energy of the SQUID
C_J	capacitance of the Josephson junction
α	anharmonicity of transmon qubit
ω_q	the qubit transition frequency
g	vacuum Rabi coupling frequency
ω_r	frequency of the resonator

T_1	qubit relaxation time
T_2	qubit dephasing time
Ω_R	Rabi frequency
ω_d	microwave field frequency
\otimes, \oplus	tensor product, direct sum

CONTENTS

Dedication	i
Acknowledgment	ii
Résumé	iv
Abstract	v
Résumé détaillé	vi
List of publications	viii
Liste of figures	xii
List of Abbreviations	xiii
List of Symbols	xiv
Contents	xviii
General Introduction	1
I Fundamental concepts of quantum information processing and computation	7
I.1 Quantum bit	7
I.1.1 Definition	7
I.1.2 Many qubits or quantum register	9
I.2 Quantum gates and circuits	9
I.2.1 Single-qubit gates	10

I.2.2	Multi-qubit gates and universality	12
I.2.3	Quantum circuit for two- and three-qubit entanglement	15
I.3	Quantum algorithms	16
I.3.1	Quantum parallelism needed in an algorithm	17
I.3.2	Grover quantum algorithm	17
I.3.3	Deutsch-Jozsa quantum algorithm	20
I.4	Chapter summary	22
II	Quantum superconducting circuits	23
II.1	Superconducting qubits	23
II.1.1	The Josephson Junction	23
II.1.2	SQUID	26
II.1.3	Charge qubit(The Cooper pair box)	27
II.1.4	Transmon qubit	31
II.2	Cavity quantum electrodynamics	34
II.2.1	Quantification of the field in a cavity	34
II.2.2	Jaynes-Cummings model	36
II.2.3	Approximation of the dipole moment and the rotating wave	37
II.2.4	Resonance regime and dispersive regime	39
II.3	Circuit quantum electrodynamics	40
II.3.1	Quantum harmonic LC oscillator	41
II.3.2	Transmission line (Coplanar waveguide)	42
II.3.3	Coupling a transmon-type superconducting qubit to a coplanar waveguide resonator	44
II.4	Quantum gates with superconducting device	46
II.4.1	Single-qubit gates	46
II.4.2	Two-qubit gates	48
II.5	Chapter summary	50
III	Realizing two- and multi-qubit quantum gates in open quantum systems via QED circuit for superconducting qubits	51
III.1	Multi-qubit device description	52
III.1.1	Multi-qubit device	52
III.1.2	Hamiltonian description and the corresponding time evolution operator	53
III.2	Open system dynamics	56

III.2.1	Master equation	56
III.2.2	Fidelity under master equation	57
III.3	Realizing X -rotation gate for multi-qubit in the open quantum systems	57
III.3.1	X -rotation gate for two transmon systems	58
III.3.1.1	Two-qubit X -rotation gate generation	58
III.3.1.2	Fidelity and discussion	59
III.3.2	X -rotation gate for three transmon systems	61
III.3.2.1	Three-qubit X -rotation gate generation	61
III.3.2.2	Fidelity and discussion	62
III.4	Single-shot entangling gate in the open quantum systems	64
III.4.1	Entangling gate for two transmon systems	64
III.4.1.1	Two-qubit entangling gate generation	64
III.4.1.2	Two-qubit entangling gate characterization	65
III.4.2	Entangling gate for three transmon systems	66
III.4.2.1	Three-qubit entangling gate generation	66
III.4.2.2	Three-qubit entangling gate characterization	66
III.5	Chapter summary	69

IV Implementing X -rotation gates in Grover's algorithm and quantum process

	tomography of the entangling gates	70
IV.1	Grover's algorithm with X -rotation gates	71
IV.1.1	Three-Qubit Grover's Search Algorithm	71
IV.1.2	Grover's Search Algorithm for n -qubit	72
IV.2	Implementing the X -rotation gate in Grover's search algorithm	74
IV.2.1	Grover's algorithm for a two-qubit X -rotation gate	74
IV.2.2	Grover's algorithm for three-qubit X -rotation gate	76
IV.3	Characterization of the single-shot entangling gate by quantum process tomography	79
IV.3.1	Quantum process tomography (QPT)	79
IV.3.2	Two-qubit entangling gate characterization	80
IV.3.3	Three-qubit entangling gate characterization	81
IV.4	Chapter summary	84

V General Conclusion and Future Directions

CHAPITRE

GENERAL INTRODUCTION

"Computers are physical objects, and computations are physical processes. What computers can or cannot compute is determined by the laws of physics alone, and not by pure mathematics."

David Deutsch

Quantum information is an emerging field that includes several specialties such as physics, engineering, chemistry, computer science, and mathematics. The main aim of this integration is to know how the realization of a quantum computer and the use of such a computer to perform specific calculations are much faster than with a computer operating in a standard way (classical computer)[1, 2]. It captures all of the operations regarding quantum information processing exploiting the properties of quantum mechanics such as the superposition of states, entanglement, and interference.

The important general idea of quantum information processing (QIP) is to realize a quantum device- so-called a quantum computer which has started just about the last century, exactly in the early 1980s when Feynman showed that a classical machine would be unable to efficiently simulate a quantum system[3], where the idea is that a classical bit can be replaced by a two-level quantum system. Similar to a classical machine which can store its information in strings of bits that can either be 0 or 1, a quantum computer uses a unit of quantum information called a quantum bit or qubit, which is a two-level quantum system. Still, unlike in classical physics, the qubit can exist in a superposition of its computational basis states $|0\rangle$ and $|1\rangle$ which can be formed by the ground

and excited states of an electron in an atom for example, which represents the phenomenon of quantum superposition. Some examples mentioned in the physical realization are spin, photons, ion traps, quantum dots, nuclear magnetic resonance (NMR), superconducting qubits, etc.

Quantum information processing and computation is an application of quantum information that includes quantum gates, quantum algorithms, quantum error-correcting codes, quantum cryptography, etc, and represents a revolutionary field of information processing. The first simple quantum algorithm using quantum mechanics to solve essentially the determining problem of whether a coin is fair or biased more efficiently than any classical algorithm was proposed by David Deutsch in 1985[4]. In addition, Peter Shor 1994 invented an efficient quantum algorithm that factorizes a large integer number[5], which is exponentially more efficient than its classical counterpart in terms of time. Another famous algorithm worth mentioning in this area was proposed by Lov Grover in 1996[6], addresses searching in an unsorted large database which is a hard mathematical problem in the classical approach. The computation time of this search algorithm equals the square root of the fastest classical algorithm time.

In the following, in the context of *QIP* the quantum algorithms have been demonstrated with many physical systems. For instance, the Deutsch-Jozsa algorithm has been realized in NMR[7, 8, 9, 10, 11, 12], trapped ion[13], photonic[14] systems, and superconducting devices[15, 16, 17], as well as for further challenging Shor's algorithm has only been demonstrated for the factorization of the number 15 with NMR techniques[18] and photons [19, 20, 21]. In the last decades, following the context of the building blocks of a quantum device, the experimental realization of quantum error correction protocols has been made in NMR[22], and then in linear optics [23], trapped ions[24, 25], and also superconducting circuits[26, 27, 28].

Another interesting quantum algorithm in terms of physical realizations and considered a good candidate for demonstrating the power of quantum information processing and computation in view of its being easy to implement is Grover's algorithm. Grover's algorithm is known as a search algorithm, which is a quantum method that is used to search through unstructured databases using iteration steps that are fewer than classical algorithms to determine the unique input to a black box function (quantum Oracle) by increasing its probability that it will be measured. This algorithm has been theoretically and experimentally realized with its two- and multi-qubit case using the NMR system[29, 30], trapped ions[31, 32, 33, 34], cavity quantum electrodynamics (cavity QED)[35, 36, 37, 38]. Recently, Grover's search algorithm was experimentally realized using a scalable trapped atomic ion system for three qubits and it was executed for one iteration[39].

In these physical systems such as NMR, trapped ions, and photonic, the properties of the

qubits are naturally occurring. In contrast, the superconducting qubits are made up of artificial electronic structures that consist of several circuit components, which are capacitors, inductors, and the Josephson junction characterized by its inductance and capacitance. Different of these elements allow the designing and engineering of their properties to a large extent, such as the energy level structure and the coupling of the qubits to their environment. Whereas some of these properties can be tuned using magnetic fields. Several types of superconducting qubits were proposed in different configurations using Josephson junctions such as flux qubit[40], phase qubit[41], charge qubit[42], as well as the transmon qubit as an interesting case in this thesis[43], which is a modified version of the charge qubit.

It is worth noticing that the experimental realization for two-qubit Grover's algorithm has been demonstrated using a quantum device[16], including transmon-type superconducting qubits coupled to a quantum electrodynamics circuit (circuit QED). Circuit QED setup as proposed by Blais et al. [44] and then realized by Wallraff et al. in the experiment[45], studying the interaction between single microwave photons and superconducting qubits behaving as artificial atoms, and a similar version of cavity quantum electrodynamics (cavity QED), which is the fundamental coupling between a photon and a two-level system. Additionally, many experimental realizations have been successfully made with superconducting qubits in QED circuit in the context of QIP : demonstration of a single qubit gate[46], generation and measurement of two- and multi-qubit entanglement[48, 49, 50, 51, 52], realizing multi-qubit quantum error correction[26, 27, 28].

Entanglement is the most interesting aspect of quantum theory[67], and is an essential resource for QIP. Therefore, the creation and demonstration of maximally entangled states are central for quantum communication and QIP, in particular, a few examples that require entangling quantum systems in Bell and Greenberger-Horne-Zeilinger (GHZ) states, quantum computation[1, 68], quantum error correction[69, 70], quantum sense[71], and quantum metrology[72]. In the past decade, significant progress has been witnessed in entanglement engineering with superconducting devices : the preparation and measurement of two-qubit entangled state(Bell states) based on the combination of single rotation and controlled-phase gates, was realized by L. DiCarlo et al. in the experiment[16]. In addition, the preparation of W- and GHZ-maximally-entangled states for three and more qubits is based on the decomposition into sequences of a single rotation and two-qubit controlled phase or iSWAP gates which were realized in the experiments[48, 49, 50].

To fully characterize the performance of these quantum algorithms and gates, it is necessary to use quantum process tomography (QPT)[1, 73, 74]. QPT is an essential tool for reliable QIP, it allows us to predict the evolution of a quantum state as it propagates through an imperfect

quantum gate. In real experiments, where the interaction between the quantum system and the environment cannot be neglected, it is not possible to describe the evolution of a quantum state by a unitary operator. Thus, QPT is a useful method for experimentally describing a complete implementation of quantum gates. This method is used to characterize the systems of one- and two-qubit quantum gates in[75, 76, 77, 78, 79, 80, 81]. QPT has been used with superconducting systems for the two-qubit entangling gate to characterize a square root i-SWAP gate[62], and for three-qubit operations to characterize Toffoli and C-Phase gates[64, 26].

Although the building blocks of quantum algorithms are constructed using basic quantum logic gates as single- and two-qubit gates[82, 83, 84, 85, 86, 87], however, building a multiqubit gate using only quantum basic gates will be difficult owing to the number of basic gates drastically increasing with the growing number of qubits. Therefore, the use of the direct implementation of a multiqubit gate offers more efficiency than the combination of basic gates. In addition, the realization of a multi-qubit gate using only a one-step operation replaces the complex combination of one- and two-qubit gates. Over the past years, using the direct implementation approach of the multiqubit gate has drawn much interest. In this context, single-shot implementation of a Toffoli gate of three qubits has been experimentally demonstrated in different physical systems[88, 89, 91]. In addition, based on superconducting qubits coupled to a resonator in circuit QED, many schemes have been previously proposed for the one-step realization of multi-qubit gates[92, 93, 94, 95, 96, 97, 98, 99, 100, 101, 102, 103].

Outline of the thesis

This thesis focuses on the realization, and characterization of quantum gates and algorithms using a one-step approach based on the superconducting quantum device. Such a quantum device is constructed by transmon-type superconducting qubits coupled to a superconducting resonator, driven by a classical field. Using it, we propose a fast scheme to prepare a quantum register involving many of the basic states in quantum superposition by realizing the X -rotation gate for two and more qubits requiring only one-step operation. In addition, using the same approach we realize the single-shot entangling gate for two and more qubits, these gates are used to create a maximally entangled state such as a two-qubit Bell-state and a three-qubit GHZ-state. Using strictly numerical simulation under realistic assumptions about system parameters, we investigate the quantum dynamics of these gates and show that these schemes can be implemented with high fidelity.

Using the implemented x -rotation gates, we present an alternative way to implement the two- and three-qubit Grover's algorithm, which does not require a series of single gates. Our implementation showed that the proposed scheme allows for efficiently finding the correct state with a high $> 90\%$ fidelity. As well, we demonstrate by numerically simulating the use of QPT to fully characterize the performance of a single-shot entangling gate for two and more qubits and obtaining process fidelity greater than 93%.

The structure of this thesis is organized as follows :

In the first chapter [I](#), we will briefly discuss some of the basics of quantum information processing and computing. This includes the mathematical and geometric properties of quantum bits as well as the description of how they can be manipulated and how a quantum computer differs from its classical counterpart. We will also identify a universal set of quantum logic gates, involving single- and multi-qubit gates, and how they contribute to building quantum algorithms, for instance, the Grover and Deutsch Jozsa algorithms, quantum entanglement protocols, and the preparation of superposition states.

In the second chapter [II](#), we will discuss the physical implementation of quantum bits using electrical circuits to realize superconducting qubits, and we will review some types of these qubits such as the Cooper-pair box (charge qubit), and the transmon qubit which is used in this thesis, as well as the quantum harmonic LC oscillator as an essential component in circuit QED. There will also be a description about the interaction between superconducting qubits and a superconducting transmission line or LC oscillator (the electromagnetic field) inside a circuit QED that is a similar version to a cavity QED which is also discussed. As well, the dispersive regime needed for QIP is discussed. Finally, we will conclude this chapter by associating circuit QED (Quantum Electrodynamics) with QIP. In this section, we will identify the single-qubit gates as well as C-Phase and iSWAP gates, which have been experimentally realized using superconducting devices[\[16, 62\]](#).

Chapter [III](#) of this thesis is aimed to realizing an X -rotation gate for two and three qubits which can be used for preparing superposition states and others called entangling gates used for generating maximally entangled states such as Bell and GHZ states, and thier implementation is based on a quantum device comprising transmon qubits capacitively coupled with a resonator driven by a microwave field using a one-step approach. The robustness of these gates is demonstrated by including the effect of the decoherence of the transmon systems and the resonator decay in a master equation formalism. For realistic assumptions about the transmon-resonator system parameters, high fidelity will be achieved on a quantum simulation. In the end, we will discuss the experimental feasibility of the proposed schemes and compare them with the latest experimental

results within superconducting devices.

In the following, based on the implemented X-rotation gates in chapter III and C-Phase gate we will propose practical and faster schemes for implementing a two- and three-qubit Grover's search with an implementation time significantly shorter than the coherences time of superconducting qubits in chapter IV. There will also be a brief discussion about some thoughts regarding the possibility of experimental realization of the proposed schemes. In addition to the characterization of the single-shot entangling gates for two and three qubits in the chapter III we here fully characterize these gates using QPT demonstrated by numerical simulation and obtaining process fidelities greater than 93%.

Finally, this thesis will end with a conclusion and perspectives.

CHAPITRE I

FUNDAMENTAL CONCEPTS OF QUANTUM INFORMATION PROCESSING AND COMPUTATION

This chapter is intended to briefly give the fundamental concepts of quantum computation based on the book of Nielsen and Chuang[1], including the mathematical and geometric properties of a qubit or a quantum bit. In addition, it describes the quantum gates for single- and multi-qubit, as well as the discussion of universal quantum gates needed to accomplish the arbitrary quantum computation. At the end of this chapter, we also discuss quantum algorithms exploiting quantum superposition and entanglement to perform specific calculations. We first discuss the quantum parallelism, which characterizes a method allowing quantum computers to evaluate a function $f(x)$ for a large number of x -values simultaneously. We will then use quantum parallelism and other laws of quantum mechanics to move on to discuss some quantum algorithms such as Grover and the Deutsch-Jozsa algorithm.

I.1 Quantum bit

In a classical computer, the fundamental unit of information is the so-called binary digit or bit and can take one of two possible values 0 or 1. These values physically correspond for instance to whether a capacitor is being charged or discharged. Similarly, in a quantum computer two-level quantum systems can form the quantum bit or qubit.

I.1.1 Definition

The fundamental unit of quantum information is the quantum bit or, more simply, qubit, which can be in states $|0\rangle$ and $|1\rangle$. These quantum states can be formed by any quantum system

with two different energy levels, for example of an appropriate system is the spin of an electron in a static magnetic field. Unlike classical computing in which the bit must be either 0 or 1, the qubit can be prepared in what is called a "quantum superposition" of both states $|0\rangle$ and $|1\rangle$ at the same time, in quantum computing. Mathematically, such a superposition state is represented by

$$|\psi\rangle = \alpha \begin{pmatrix} 1 \\ 0 \end{pmatrix} + \beta \begin{pmatrix} 0 \\ 1 \end{pmatrix}, \quad (\text{I.1})$$

where the numbers α and β are complex numbers, which satisfy the normalization condition $|\alpha|^2 + |\beta|^2 = 1$. While the orthonormal basis states $|0\rangle$ and $|1\rangle$ are known as computational basis states. The measurement outcome of the qubit is either 0, with the probability $|\alpha|^2$ or 1, with the probability $|\beta|^2$.

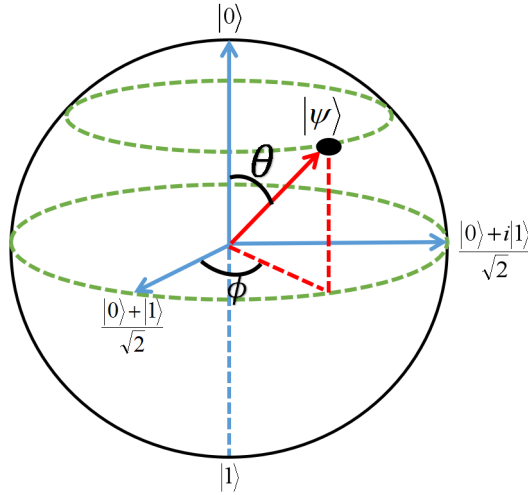


FIGURE I.1 – Bloch sphere representation of a qubit.

It is useful to geometrically represent the qubit state for a better understanding of the action of quantum operations on the state. To find such a visual interpretation, without losing any generality we may rewrite equation (I.1) as

$$|\psi\rangle = \cos\left(\frac{\theta}{2}\right) |0\rangle + e^{i\phi} \sin\left(\frac{\theta}{2}\right) |1\rangle, \quad (\text{I.2})$$

where $\theta \in [0, \pi]$ and $\phi \in [0, 2\pi]$. The ground and excited states $|0\rangle$ and $|1\rangle$ can represent the South and North poles of a sphere, respectively, and thus each point on this so-called Bloch sphere represents a superposition state (see figure I.1).

I.1.2 Many qubits or quantum register

A classical register is a set of n bits that, in a sense, stores all numbers between 0 and $2^n - 1$. A quantum register, like a classical register, just is a system comprising many qubits. In the case of three quantum bits, this yields the computational basis states involving the eight possible states $\{|000\rangle, |001\rangle, |010\rangle, |011\rangle, |100\rangle, |101\rangle, |110\rangle, |111\rangle\}$ (where $|ijk\rangle = |i\rangle \otimes |j\rangle \otimes |k\rangle$). Like a single qubit, the three-qubit state is given by the linear combination of the eight basis states

$$\begin{aligned} |\psi\rangle &= \alpha_{000} |000\rangle + \alpha_{001} |001\rangle + \alpha_{010} |010\rangle + \alpha_{011} |011\rangle + \alpha_{100} |100\rangle \\ &+ \alpha_{101} |101\rangle + \alpha_{110} |110\rangle + \alpha_{111} |111\rangle, \end{aligned} \quad (\text{I.3})$$

where α_{ijk} are the complex numbers which satisfy the normalization condition $\sum_{ijk} |\alpha_{ijk}|^2 = 1$ ($ijk = 000, 001, 010, 011, 100, 101, 110, 111$). An important property of qubits is that they can be entangled with other qubits. Three quantum systems can be entangled if the state of the total system cannot be written as a Kronecker product of its parts. In the context of quantum computing, three qubits can be entangled in two different ways by the states

$$|GHZ\rangle = \frac{1}{\sqrt{2}} (|000\rangle + |111\rangle), \quad (\text{I.4})$$

$$|W\rangle = \frac{1}{\sqrt{3}} (|001\rangle + |010\rangle + |100\rangle), \quad (\text{I.5})$$

I.2 Quantum gates and circuits

Besides storing information, we also mention that the processing of quantum information is useful to build quantum computing, in order to move information from one qubit to another. Such information processing is carried out by the action of quantum gates on qubits or quantum registers. In analogy to classical computing which through in it the circuit model is very useful for computing processes and is also used to design and construct computing hardware using different types of classical logic gates acting on some binary input, for example, the NAND, NOR, AND, and OR gates, whereas quantum computers can be interpreted in terms of a quantum circuit model comprising quantum gates, which are applied to quantum register. In quantum computers, we have two different types of quantum gates : single qubit and multi-qubit gates. Single qubit gates operate only on one qubit, while multi-qubit gates operate on two or more qubits. We will give examples of these types of operations in detail in the rest of this section.

I.2.1 Single-qubit gates

An n -qubit gate can be represented as $2^n \times 2^n$ unitary matrices. Due to the single-qubit gate operating only on one qubit, thus single-qubit gates can be represented by matrices of size 2×2 .

Rotation gates

Generally, the single quantum operation can be visualized by using the Bloch sphere (shown in figure I.1) as a rotation of the state around the x, y , and z axes. Some of the single qubit gates which are used to generate the rotation about the Bloch sphere axes can be described using Pauli matrices as follows :

$$X = \sigma_x = \begin{pmatrix} 0 & 1 \\ 1 & 0 \end{pmatrix}, \quad (\text{I.6})$$

$$Y = \sigma_y = \begin{pmatrix} 0 & -i \\ i & 0 \end{pmatrix}, \quad (\text{I.7})$$

$$Z = \sigma_z = \begin{pmatrix} 1 & 0 \\ 0 & -1 \end{pmatrix}. \quad (\text{I.8})$$

When we apply these single-qubit gates to the computational basis states $|0\rangle$ and $|1\rangle$, we easily get

$$X|0\rangle = |1\rangle, X|1\rangle = |0\rangle, \quad (\text{I.9})$$

$$Y|0\rangle = i|1\rangle, Y|1\rangle = -i|0\rangle, \quad (\text{I.10})$$

$$Z|0\rangle = |0\rangle, Z|1\rangle = -|1\rangle. \quad (\text{I.11})$$

Besides these rotation operations, we would like to mention the other important single-qubit

gates, which are also rotation operations, which are given by

$$R_x(\theta) = e^{-i\theta\sigma_x/2} = \begin{pmatrix} \cos\left(\frac{\theta}{2}\right) & -i\sin\left(\frac{\theta}{2}\right) \\ -i\sin\left(\frac{\theta}{2}\right) & \cos\left(\frac{\theta}{2}\right) \end{pmatrix}, \quad (\text{I.12})$$

$$R_y(\theta) = e^{-i\theta\sigma_y/2} = \begin{pmatrix} \cos\left(\frac{\theta}{2}\right) & -\sin\left(\frac{\theta}{2}\right) \\ \sin\left(\frac{\theta}{2}\right) & \cos\left(\frac{\theta}{2}\right) \end{pmatrix}, \quad (\text{I.13})$$

$$R_z(\theta) = e^{-i\theta\sigma_z/2} = \begin{pmatrix} e^{-i\theta/2} & 0 \\ 0 & e^{i\theta/2} \end{pmatrix}, \quad (\text{I.14})$$

where θ is the angle of rotation. Based on these gates, we can identify some other important single-qubit operations just by performing rotations of $\theta = \mp\pi$ and $\theta = \mp\pi/2$, often mentioned as π -pulses and $\mp\pi/2$ -pulses, respectively. We can identify the Pauli matrices by choosing $\theta = \pi$, $R_x(\pi) = -i\sigma_x$, $R_y(\pi) = -i\sigma_y$, $R_z(\pi) = -i\sigma_z$. Similarly, when choosing $\theta = \pi/2$ in the equations (I.12) and (I.13), these operations map a state initially prepared in the ground ($|0\rangle$) or an excited ($|1\rangle$) state into an equal superposition of the states $|0\rangle$ and $|1\rangle$ as follows

$$R_x\left(\frac{\pi}{2}\right)|0\rangle = \frac{1}{\sqrt{2}}(|0\rangle - i|1\rangle), R_x\left(\frac{\pi}{2}\right)|1\rangle = \frac{-i}{\sqrt{2}}(|0\rangle + i|1\rangle), \quad (\text{I.15})$$

$$R_y\left(\frac{\pi}{2}\right)|0\rangle = \frac{1}{\sqrt{2}}(|0\rangle + |1\rangle), R_y\left(\frac{\pi}{2}\right)|1\rangle = \frac{1}{\sqrt{2}}(|0\rangle - |1\rangle). \quad (\text{I.16})$$

In addition, it is worth mentioning that the similar single-qubit gate of these operations, the Hadamard gate enables qubit interference which is necessary for quantum algorithms and has no classical analog. It can be described by a unitary matrix

$$H = \frac{1}{\sqrt{2}} \begin{pmatrix} 1 & 1 \\ 1 & -1 \end{pmatrix}. \quad (\text{I.17})$$

On the other hand, one can usually rewrite the Hadamard gate by decomposing it into se-

quences of rotation operations around the x and y axes in the Bloch sphere in the following form :

$$H = e^{i\frac{\pi}{2}} R_x(\pi) R_y\left(\frac{\pi}{2}\right). \quad (\text{I.18})$$

Finally, we have to mention other important single qubit gates, S and T gates, which are so-called the phase gates. These gates rotate the state vector around the z-axis on the Bloch sphere by changing the dynamic phase of the state

$$S = \begin{pmatrix} 1 & 0 \\ 0 & i \end{pmatrix}, \quad (\text{I.19})$$

$$T = \begin{pmatrix} 1 & 0 \\ 0 & e^{i\frac{\pi}{4}} \end{pmatrix}. \quad (\text{I.20})$$

For more details on how to implement the rotation gates for single- and multi-qubit see chapters [II](#) and [III](#).

I.2.2 Multi-qubit gates and universality

Multi-qubit gates

In addition to single-qubit gates that can be applied to individual qubits, there are also other important multi-qubit gates known as controlled-unitary gates. In most of these gates, some qubits play a target role while some qubits play the control role. Such controlled-unitary operations are performed on the target qubit which will change depending on the state of the control qubit. One of the most famous two-qubit gates is the controlled-not operation (*CNOT*). The action of the controlled-not operation is to invert the state of the target qubit if the control qubit is $|1\rangle$, and the state of the target qubit does not change if the control qubit is $|0\rangle$. Therefore, the quantum circuit (Figure [\(I.2\)](#)) and matrix representation of this gate in the computational basis states of

two-qubits, $|0, 0\rangle$, $|0, 1\rangle$, $|1, 0\rangle$, and $|1, 1\rangle$

$$CNOT = \begin{pmatrix} 1 & 0 & 0 & 0 \\ 0 & 1 & 0 & 0 \\ 0 & 0 & 0 & 1 \\ 0 & 0 & 1 & 0 \end{pmatrix}. \quad (I.21)$$

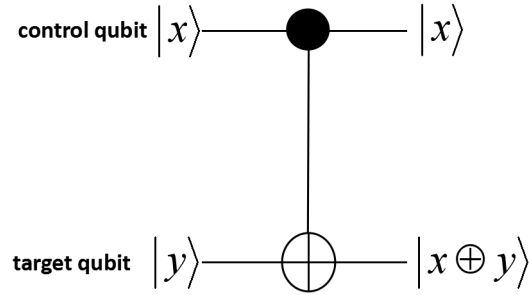


FIGURE I.2 – Quantum circuit representation for CNOT gate. Here $x, y = 0$ or 1 and \oplus denotes the addition modulo 2, while the vertical line between the control and target qubit represents the circuit diagram of CNOT gate.

This gate is often used to generate the maximally entangled state, the Bell states defined by $|\Phi^\pm\rangle = (|00\rangle \pm |11\rangle)/\sqrt{2}$ and $|\psi^\pm\rangle = (|01\rangle \pm |10\rangle)/\sqrt{2}$, and thus CNOT is an entangling gate.

Another controlled-unitary operation of a two-qubit gate is called the CPhase (CP) gate which performs a controlled-Z operation. This is done if two qubits are in $|1\rangle$. Thus, the matrix representation of this gate (CP) is given by

$$CP = \begin{pmatrix} 1 & 0 & 0 & 0 \\ 0 & 1 & 0 & 0 \\ 0 & 0 & 1 & 0 \\ 0 & 0 & 0 & -1 \end{pmatrix}. \quad (I.22)$$

We note that the CNOT gate can be realized by combining CP gate and two Hadamard gates on both qubits.

Other important two-qubit gates are $iSWAP$ and \sqrt{iSWAP} , which are perfect to generate

maximally entangled states, and are defined by

$$iSWAP = \begin{pmatrix} 1 & 0 & 0 & 0 \\ 0 & 0 & i & 0 \\ 0 & i & 0 & 0 \\ 0 & 0 & 0 & 1 \end{pmatrix} \text{ and } \sqrt{iSWAP} = \begin{pmatrix} 1 & 0 & 0 & 0 \\ 0 & \frac{1}{\sqrt{2}} & \frac{i}{\sqrt{2}} & 0 \\ 0 & \frac{i}{\sqrt{2}} & \frac{1}{\sqrt{2}} & 0 \\ 0 & 0 & 0 & 1 \end{pmatrix}. \quad (\text{I.23})$$

An example of a controlled-unitary operation for a three-qubit gate is a Toffoli gate, which is essentially a controlled-controlled-X gate, flipping the state of the target qubit only if both of the first two control qubits are in $|1\rangle$

$$Toffoli = \begin{pmatrix} 1 & 0 & 0 & 0 & 0 & 0 & 0 & 0 \\ 0 & 1 & 0 & 0 & 0 & 0 & 0 & 0 \\ 0 & 0 & 1 & 0 & 0 & 0 & 0 & 0 \\ 0 & 0 & 0 & 1 & 0 & 0 & 0 & 0 \\ 0 & 0 & 0 & 0 & 1 & 0 & 0 & 0 \\ 0 & 0 & 0 & 0 & 0 & 1 & 0 & 0 \\ 0 & 0 & 0 & 0 & 0 & 0 & 0 & 1 \\ 0 & 0 & 0 & 0 & 0 & 0 & 1 & 0 \end{pmatrix}. \quad (\text{I.24})$$

In addition, we also have another three-qubit gate that is the Fredkin gate, which performs a controlled SWAP operation, which exchanges the states of two target qubits if only the first

control qubit is in state $|1\rangle$

$$Fredkin = \begin{pmatrix} 1 & 0 & 0 & 0 & 0 & 0 & 0 & 0 \\ 0 & 1 & 0 & 0 & 0 & 0 & 0 & 0 \\ 0 & 0 & 1 & 0 & 0 & 0 & 0 & 0 \\ 0 & 0 & 0 & 1 & 0 & 0 & 0 & 0 \\ 0 & 0 & 0 & 0 & 1 & 0 & 0 & 0 \\ 0 & 0 & 0 & 0 & 0 & 1 & 0 & 0 \\ 0 & 0 & 0 & 0 & 0 & 0 & 1 & 0 \\ 0 & 0 & 0 & 0 & 0 & 0 & 0 & 1 \end{pmatrix}. \quad (I.25)$$

Universality

The concept of universality is associated with the ability to comprise any computational algorithm with a set of simple gates. For instance, in classical computing, the MAND gate is a gate that can be implemented using a combination of AND and NOT gates and thus the NAND gate is referred to as a universal gate. Similar to universal classical logic operations, there is also a set of quantum gates that are universal, such combinations of some gates can realize complex algorithms in quantum computing. However, unlike classical computing in which a single gate is necessary, the universality in quantum counterpart can only be achieved by combining the arbitrary single qubit gates and cNOT gate, as well as the set of single qubit gates and Toffoli gate. In general, at least one multi-qubit gate is required in a universal set for quantum computing.

I.2.3 Quantum circuit for two- and three-qubit entanglement

A quantum circuit is a set of gates applied to quantum registers or qubits, it is used to design and construct computing hardware. As an example, we here discuss the two quantum circuits that can be used to generate maximally entangled states, the Bell state $(|\Phi^+\rangle = (|00\rangle + |11\rangle)/\sqrt{2})$, and the GHZ-state given in the equation (I.4). In order to generate the Bell state, the single and two-qubit gates are required in the corresponding quantum circuit as shown in Fig. (I.3). This circuit is read from left to right. First, the single-qubit gate on the control qubit is applied as depicted in Fig (I.3), followed by a CNOT gate to generate the entanglement.

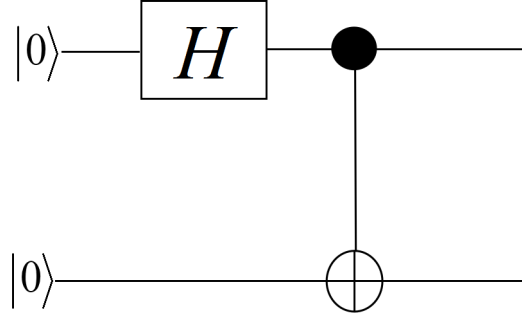


FIGURE I.3 – Quantum circuit for creating the Bell state.

In addition, the GHZ protocol can be generated by using the single qubit gate and two CNOT gates, as shown in the circuit diagram in Figure (I.4). Starting in ground state $|000\rangle$ for all three qubits, we first perform a rotation on the first qubit (with $\theta = \pi/2$) to put the whole system in state $(|000\rangle + |100\rangle)/\sqrt{2}$. To create GHZ-state, we need to map the second component of this state $|100\rangle$ to $|111\rangle$ without changing the first component. This is exactly done by applying two CNOT gates to flip the second and third qubit conditioned on the state of the first qubit. These CNOTs can be applied in the following way ; using the first qubit as the control qubit for the first gate and the second qubit as the control qubit for another gate.

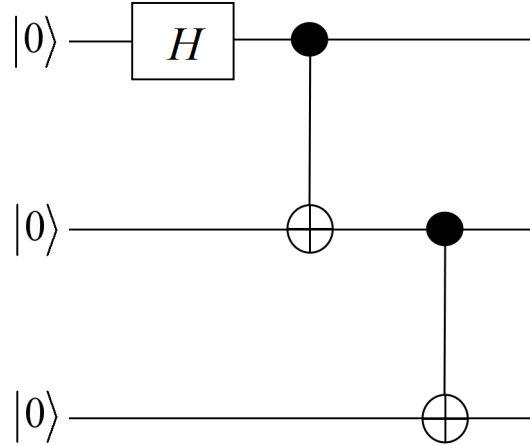


FIGURE I.4 – Quantum circuit for creating the GHZ state.

I.3 Quantum algorithms

With access to a large number of quantum gates, we can now build more complex quantum algorithms circuits by combining these gates. The power of these algorithms lies in the fundamental laws of quantum mechanics such as superposition and entanglement, which leads to performing calculations more efficiently than their classical counterparts. In this section, we will describe, in general, some quantum algorithms and their circuits diagram, they are implementable in most quantum devices.

I.3.1 Quantum parallelism needed in an algorithm

One of the important difference between quantum and classical computers is that quantum computers can store their information in superposition states. The ability of quantum computing to accomplish a quantum operation on all states at the same time, which is referred to as quantum parallelism, leads to a significant speed-up advantage over classical ones. Bellow, we explain in details how quantum parallelism works.

In general, we consider a quantum register involving $n + m$ qubits which takes n qubits as control qubits and m qubits as a target qubits. Furthermore, let us assume $f(x) : \{0, 1\}^n \rightarrow \{0, 1\}^m$ is a Boolean function and we suppose that we have an unitary transformation U_f of size $(n + m) \times (n + m)$ in which we compute the function $f(x)$ such that its action on the state $|x\rangle_n |y\rangle_m$ gives $|x\rangle_n |y \oplus f(x)\rangle_m$, using a set of quantum gates. Instead of applying U_f on each individual input state, we first create a superposition of all input states $|x\rangle_n$ using the Hadamard gate as follows

$$H^{(1)} \otimes H^{(2)} \otimes \dots H^{(n)} |0\rangle_n = \frac{1}{\sqrt{2^n}} \sum_x |x\rangle_n. \quad (\text{I.26})$$

As shown in Figure (I.5), we then apply the unitary transformation U_f on this superposition state and all qubits of the target register in the state $|0\rangle$

$$U_f \left(\frac{1}{\sqrt{2^n}} \sum_x |x\rangle_n |0\rangle_m \right) = \frac{1}{\sqrt{2^n}} \sum_x |x\rangle_n |f(x)\rangle_m. \quad (\text{I.27})$$

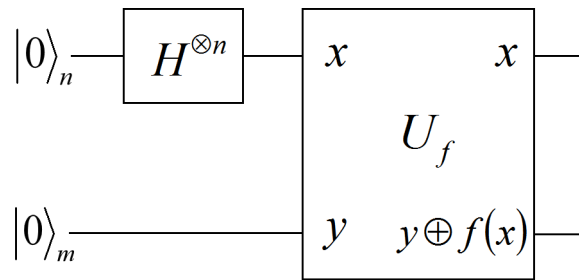


FIGURE I.5 – Quantum circuit for evaluating $f(x)$. U_f is the quantum circuit which transforms input states $|x\rangle_n |y\rangle_m$ to $|x\rangle_n |y \oplus f(x)\rangle_m$.

I.3.2 Grover quantum algorithm

Another class of quantum algorithms is for searching with quantum computing. Consider the problem of searching for a specific element through an unordered database of N elements. To classically do this, one can take up to N evaluations because all elements of the database list must

be checked. Thus, the classical algorithm uses $O(N)$ operations. However, this problem can be solved significantly more efficiently in quantum computing. Quantum search algorithm, known as Grover's algorithm, which enables one to search through an unordered list with a high probability of success, requiring only $O(\sqrt{N})$ operations. In this section, we describe Grover's algorithm steps step-by-step. We then represent the geometric visualization of this algorithm to better understand its action.

Steps and procedure

Suppose we have an unordered database of $N = 2^n$ elements (where n denotes the number of qubits), represented with a ket, $\{|0\rangle, |1\rangle, \dots, |N\rangle\}$. The general Grover algorithm implementation is divided into four steps as follows (see figure I.6) :

Step1 : Initialization

We initialize all qubits, by creating an equal superposition of all states, that were in the state $|0\rangle$. This done by applying the n -qubit Hadamard

$$|S\rangle = \frac{1}{\sqrt{2^n}} \sum_{x=1}^{2^n} |x\rangle. \quad (\text{I.28})$$

Step2 : Applying the oracle transformation

An oracle can be viewed as a black box that performs a quantum gate on a quantum register that is not easily specified by universal gates. In Grover's algorithm, an oracle can work by applying a unitary transformation U_O to the initialization qubit ($|s\rangle$) such that it flips the sign of x if and only if x is a state we are looking for or the correct state, with the following properties

$$|x\rangle \xrightarrow{U_O} (-1)^{f(x)} |x\rangle, \quad (\text{I.29})$$

where $f(x) = 1$ if x is the correct quantum state and $f(x) = 0$ otherwise. The resulting state after applying an oracle is

$$|\psi\rangle = -\alpha_x |x\rangle + \alpha_{x^*} \sum_{x^*=1, x^* \neq x}^{2^n} |x^*\rangle. \quad (\text{I.30})$$

Step 3 : Amplification

The amplification, sometimes known as the inversion about mean operation, is applied to the result quantum state after the application of an oracle, and given by

$$U_\phi = 2|S\rangle\langle S| - I. \quad (\text{I.31})$$

This stage performs a reflection of the mean, thus increasing the amplitude of the correct state. Then, the resulting state is

$$|\psi^*\rangle = (2A + \alpha_x)|x\rangle + (2A - \alpha_{x^*}) \sum_{x^*=1, x^* \neq x}^{2^n} |x^*\rangle, \quad (\text{I.32})$$

where A is the amplitude of the mean vector $|\psi\rangle$ ($A = 1/2^n \{-\alpha_x + (2^n - 1)\alpha_{x^*}\}$).

Step 4 : measurement

Finally, the algorithm output state is measured.

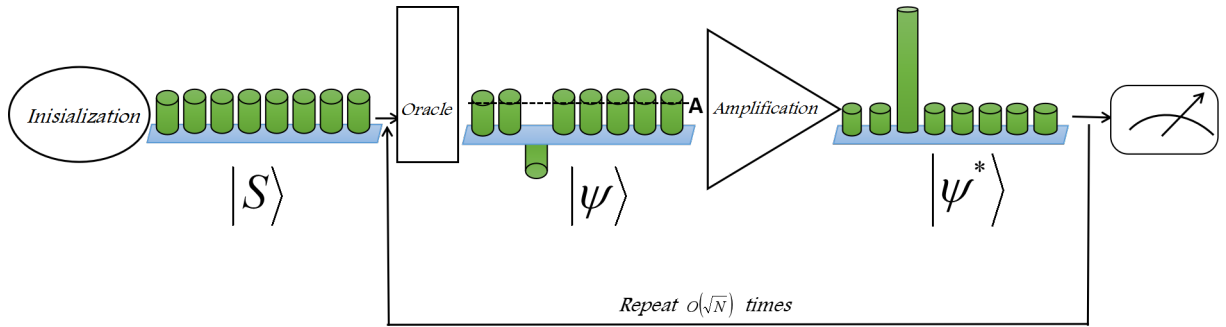


FIGURE I.6 – Evolution of amplitudes for each state during the Grover search algorithm.

Geometric visualization

We note that $G = (2|S\rangle\langle S| - I)O$, called the Grover iteration and it must be repeated many times owing to the nature of the algorithm. We will here show that this operator can be considered a rotation in the two-dimensional space spanned by the starting vector $|S\rangle$ (See Fig. I.7). We redefine the state vector in equation (II.8) as follows

$$|S\rangle = \sqrt{\frac{M}{N}}|t\rangle + \sqrt{\frac{N-M}{N}}|\bar{t}\rangle, \quad (\text{I.33})$$

with $|t\rangle$ and $|\bar{t}\rangle$ are the normalized states ($|t\rangle = \frac{1}{\sqrt{M}}|x\rangle$ and $|\bar{t}\rangle = \frac{1}{\sqrt{N-M}}\sum_{x^*}|x^*\rangle$).

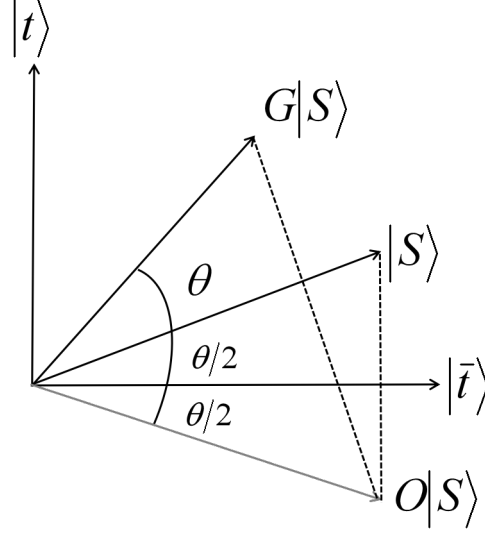


FIGURE I.7 – Geometric representation of Grover's algorithm for a single Grover iteration, G .

The effect of G can be realized by applying successively the oracle operation O that performs a reflection about the state $|t\rangle$ in the two-dimensional space defined by $|t\rangle$ and $|\bar{t}\rangle$ and then the amplification $U_\phi = 2|S\rangle\langle S| - I$ which performs a reflection in the plane defined by $|t\rangle$ and $|\bar{t}\rangle$, about the vector $|S\rangle$. Let's set $\cos(\theta/2) = \sqrt{(N-M)/N}$, and thus the equation (III.3) can be rewritten as $|S\rangle = \sin(\theta/2)|t\rangle + \cos(\theta/2)|\bar{t}\rangle$.

I.3.3 Deutsch-Jozsa quantum algorithm

One of the first and simple quantum algorithms that show that quantum computing works better than classical computing is the Deutsch-Jozsa algorithm[104], it demonstrates exponential acceleration compared to a classical algorithm. A generalization of this algorithm to functions $f(x) : \{0, 1\}^n \rightarrow \{0, 1\}$ was given by Deutsch and Jozsa and improved by Cleve, Ekert, Macchiavello, and Mosca[105]. In the Deutsch-Jozsa algorithm, the function f is either constant in which 2^n values are all either equal to 0 or to 1 or balanced in which exactly half of the values are equal to 0 and the other half to 1.

The Deutsch -Jozsa algorithm is divided in general into four steps. These steps are depicted in figure (I.8), let us follow the numbered states according to this circuit :

Step 1

Deutsch-Jozsa algorithm starts with a quantum register of n qubits, we initialize all the qubits of the first register in $|1\rangle$ and of the second register in $|1\rangle$

$$|\psi_0\rangle = |0\rangle^{\otimes n} |1\rangle. \quad (\text{I.34})$$

Step 2

We apply the Hadamard operator to each qubit of the registers, we get

$$|\psi_1\rangle = \frac{1}{\sqrt{2^n}} \sum_x |x\rangle_n \left[\frac{|0\rangle - |1\rangle}{\sqrt{2}} \right]. \quad (\text{I.35})$$

Step 3

Next step, the function f is evaluated using $U_f : |x\rangle |y\rangle \rightarrow |x\rangle |y \oplus f(x)\rangle$, giving

$$|\psi_2\rangle = \frac{1}{\sqrt{2^n}} \sum_x (-1)^{f(x)} |x\rangle_n \left[\frac{|0\rangle - |1\rangle}{\sqrt{2}} \right]. \quad (\text{I.36})$$

Step 4

The last step is to apply the Hadamard operator on a state $|x\rangle$ and the measurement.

We separately check the cases $x = 0$ and $x = 1$, we then see the Hadamard transform for a single qubit $H|x\rangle = \sum_z (-1)^{xz} |z\rangle / \sqrt{2}$, and thus for n -qubits

$$H^{\otimes n} |x\rangle_n = \frac{1}{\sqrt{2^n}} \sum_z (-1)^{xz} |z\rangle_n. \quad (\text{I.37})$$

So by using this equation and (I.36), we easily find

$$|\psi_3\rangle = \frac{1}{\sqrt{2^n}} \sum_z (-1)^{xz+f(x)} |z\rangle_n \left[\frac{|0\rangle - |1\rangle}{\sqrt{2}} \right]. \quad (\text{I.38})$$

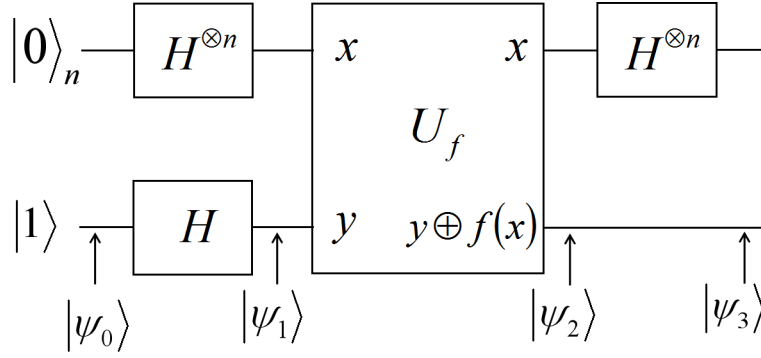


FIGURE I.8 – Quantum circuit implementing the general Deutsch-Jozsa algorithm.

I.4 Chapter summary

In this chapter, we have discussed the fundamental notions needed for quantum information processing such as the mathematical and geometric of a qubit, quantum superposition, and entanglement as well as single qubit gates. Such notions and entangling two-qubit gates are required to build any simple quantum processor. We have also seen how some two- and multi-qubit gates, for instance, the *CNOT*, *CZ*, *iSWAP*, $\sqrt{\text{SWAP}}$ and *Tofoli*, when combined with the single rotation gates, can be realized as a universal set for quantum computing. They permit the operation of some simple algorithms, such as the Grover search and Deutsch-Jozsa. Over the next chapters, we will suggest the implementation of some of these concepts with superconducting qubit devices.

CHAPITRE II

QUANTUM SUPERCONDUCTING CIRCUITS

Physically, Quantum bit or qubit implementations have taken many forms, for instance, nuclear spins, trapped-ions, photons, and superconducting qubits. In this chapter, we will describe how we use electrical circuits to realize superconducting qubits such as charge qubits and transmon qubits. An essential building block to realizing these superconducting qubits is the Josephson junction, the fundamental properties of which are discussed. We will also describe the interaction between light and matter inside the cavity QED and its analog called the circuit QED, in which the cavity is replaced by a superconducting transmission line resonator capacitively coupled to a Cooper box which plays the role of the two-level atom or the superconducting qubit in the context of quantum information. We then discuss how the coupling between transmon-type superconducting qubits and the transmission line resonator, can be used to realize the single and two-qubit gates.

II.1 Superconducting qubits

One of the most popular and promising candidates for realizing scalable universal quantum computing is superconducting qubits, based on Josephson effect. The general principle of operation of these qubits includes a Josephson junction, which is characterized by its nonlinear inductance and its capacitance. Here, we introduce the Josephson junction as the key device for realizing superconducting qubits. We then derive the Hamiltonian of the Cooper pair box (Charge qubit) and the transmon-type superconducting, using the quantization of electrical circuits to perform canonical quantization of our circuits.

II.1.1 The Josephson Junction

Josephson junctions are based on the Josephson effect [106, 107]. A Josephson junction consists of two superconductors separated by an insulating barrier which limits the flow of supercurrent

between the two superconductors, as shown in the figure(II.1). Cooper pairs can coherently tunnel from one superconductor to the other, with the supercurrent I that is given by

$$I = I_c \sin(\phi), \quad (\text{II.1})$$

where I_c is the critical current of the junction, and $\phi = \theta_2 - \theta_1$ is a phase difference across the junction, which is related to the potential V between the two superconductors according to

$$\frac{d\phi}{dt} = \frac{2\pi}{\Phi_0} V, \quad (\text{II.2})$$

where $\Phi_0 = h/2e = 2,07.10^{-15}.T.m^{-15}$ is the magnetic flux quantum.

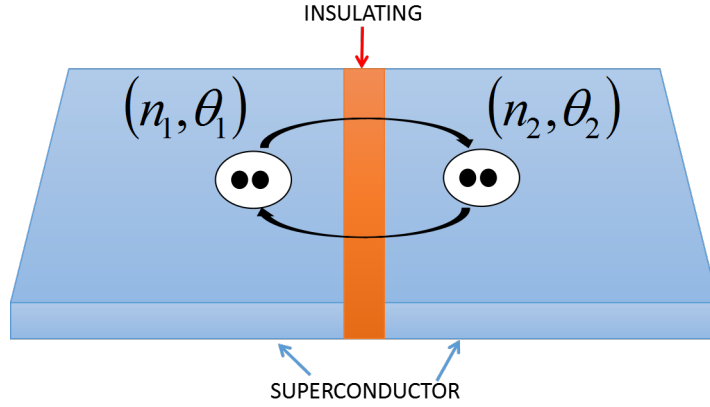


FIGURE II.1 – Schematic of a Josephson tunnel junction. It consists of two superconductors separated by an insulating barrier. The two sides of the junction are characterized by the number of Cooper pairs n_1, n_2 and the phases θ_1, θ_2 . The charge $n_2 - n_1$ and phase difference $\theta_2 - \theta_1$ between the two metals are the essential parameters describing the behavior of the junction.

Equivalent electric circuit of the Josephson junction

Physically, the Josephson junction is symbolized by a cross in a box and can be modeled as an ideal Josephson element with the Josephson energy E_J shunted by a capacitance C_J [108], as shown in Figure (II.2). We introduce the number of Cooper pairs N by $Q = 2eN$, with Q is the electrode charge, and the voltage across the junction is given by $Q = CV$. We can then determine the dynamics of a phase difference ϕ by using the Kirchhoff's rule for the circuit shown in Fig. (II.2.b) to give the differential equation

$$\begin{aligned} I_{ext} &= I_c \sin \phi + C \frac{dV}{dt} \\ &= I_c \sin \phi + \frac{h}{2e} C \ddot{\phi}. \end{aligned} \quad (\text{II.3})$$

From this equation, we readily find the Lagrangian of a Josephson junction

$$L = \frac{1}{2} \frac{C\hbar^2}{4e^2} \dot{\phi}^2 + I_c \frac{\hbar}{2e} \cos \phi + I_{ext} \frac{\hbar}{2e} \phi = K - U, \quad (\text{II.4})$$

where $K = 1/2CV^2$ is the kinetic term, and the potential energy of the system U is given by

$$U = -\frac{I_c \hbar}{2e} \cos \phi - I_{ext} \frac{\hbar}{2e} \phi. \quad (\text{II.5})$$

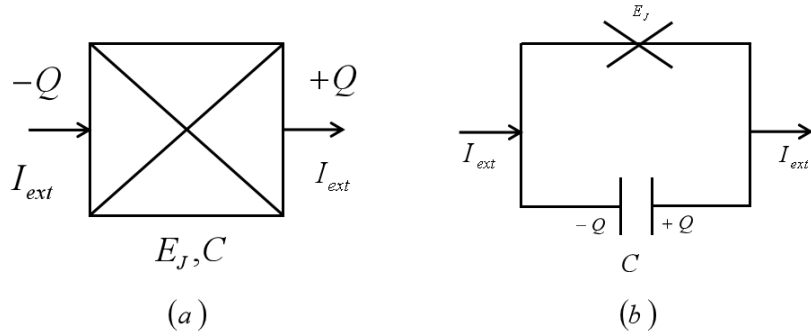


FIGURE II.2 – Schematic of a Josephson tunnel junction. (a) The symbol of the Josephson junction (Cross in a box) .(b) The equivalent electrical circuit of the Josephson junction.

The dynamics of the circuit (Hamiltonian H) is associated with the Lagrangian L through

$$\begin{aligned} H &= p\dot{\phi} - L \\ &= \frac{1}{2} \frac{E_C}{\hbar^2} p^2 - p \cos \phi - E_J \frac{I_{ext}}{I_c} \phi, \end{aligned} \quad (\text{II.6})$$

where :

- $p = -\frac{\partial H}{\partial \dot{\phi}} = \frac{C\hbar^2}{4e^2} \dot{\phi} = \frac{\hbar}{2e} Q$ is the canonical momentum operator conjugate to ϕ .
- $E_C = \frac{(2e)^2}{C}$ is the charging energy of a Cooper pair, i.e. the energy required to increase the number of Cooper pairs in the box.
- $E_J = \frac{I_0 \hbar}{2e}$ is the Josephson tunneling energy.

And the Hamiltonian equations of motion

$$\dot{\phi} = \frac{\partial H}{\partial p}, \dot{p} = -\frac{\partial H}{\partial \phi}. \quad (\text{II.7})$$

II.1.2 SQUID

There is a variant of the Josephson junction called "SQUID" [109] (Superconducting Quantum Interference Device), which consists of two ideally identical Josephson junctions in parallel coupled to a current source as shown in figure (II.3).

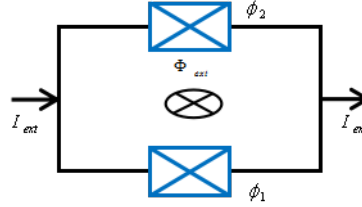


FIGURE II.3 – Schematic of a SQUID. The two Josephson junctions form a loop, which is crossed by a flux magnetic field.

According to the relation of Stokes, the magnetic flux through the loop in the presence of a magnetic field which describes the vector potential $\vec{A}(r)$ is expressed by

$$\Phi_{ext} = \oint_C \vec{A}(r) dr. \quad (\text{II.8})$$

As known, the phase variation between two points in the case of a closed superconducting loop is given by

$$\phi_2 - \phi_1 = \oint_C \vec{A}(r) dr = 2k\pi, \quad (\text{II.9})$$

and thus by combining the equations (II.8) and (II.9), the magnetic flux Φ_{ext} can be expressed as follows

$$\Phi_{ext} = \frac{\Phi_0}{2\pi} (\phi_2 - \phi_1). \quad (\text{II.10})$$

The Hamiltonian (II.6) becomes

$$H = \frac{1}{2} \frac{E_C}{\hbar^2} p^2 - U_T, \quad (\text{II.11})$$

with $U_T = U_1 + U_2$: is the potential energy of the SQUID (the sum of the Josephson energies of the two junctions), which is given by

$$U_T = -E_J (\cos(\phi_1) + \cos(\phi_2)) = -2E_J \cos\left(\frac{\phi_1 + \phi_2}{2}\right) \cos\left(\frac{\phi_2 - \phi_1}{2}\right). \quad (\text{II.12})$$

We assume that the phase $\phi = (\phi_1 + \phi_2)/2$. Then the potential term is written in the form

$$\begin{aligned} U_T &= -E_J \cos\left(\pi \frac{\Phi_{ext}}{\Phi_0}\right) \cos(\phi) \\ &= -E_J(\Phi_{ext}) \cos(\phi), \end{aligned} \quad (\text{II.13})$$

where the effective Josephson energy $E_J(\Phi_{ext}) = -E_J \cos(\pi \Phi_{ext}/\Phi_0)$ can be tuned via a magnetic flux Φ_{ext} applied through the loop of the SQUID.

II.1.3 Charge qubit(The Cooper pair box)

In the classical case, superconductivity is attributed to electron pairs, which can exist within the island : the pairs can either be inside or outside the island. However, if the tunnel barrier is large enough, as dictated by the uncertainty principle, it becomes possible for a pair to simultaneously exist both inside and outside the island, creating a superposition of 0 and 1.

The possible quantum bit, known as the "Cooper pair box," was first theoretically proposed in ref.[110] and later experimentally achieved in ref. [111]. Such the Cooper pair box consists of a superconducting island (green), which is connected via a Josephson junction (blue) with capacitance C_J and Josephson energy E_J to a large superconducting electrode (orange) as shown in figure II.4. The quantum variable is the number of superconducting pairs that are attracted to the island by a gate potential V_g applied to the gate capacitance C_g .

Electric circuit corresponding to the Cooper pair box

The superconducting circuit consists either of a Josephson junction having a Josephson energy E_J and an intrinsic capacitance C_J connected to a source of potential via a capacitance C_g as shown in the figure (II.5a) or the loop SQUID in figure(II.5b).

We apply on the figure (II.5) the same procedure that we have seen in the previous paragraphs (the Kirchhoff's rule), we can easily identify the following Lagrangian

$$L = K - U, \quad (\text{II.14})$$

where $U = -E_J \cos \phi$ is the potential energy, which is already determined in the previous sections and the kinetic energy K is the sum of the capacitive energies of the circuit, which is given by

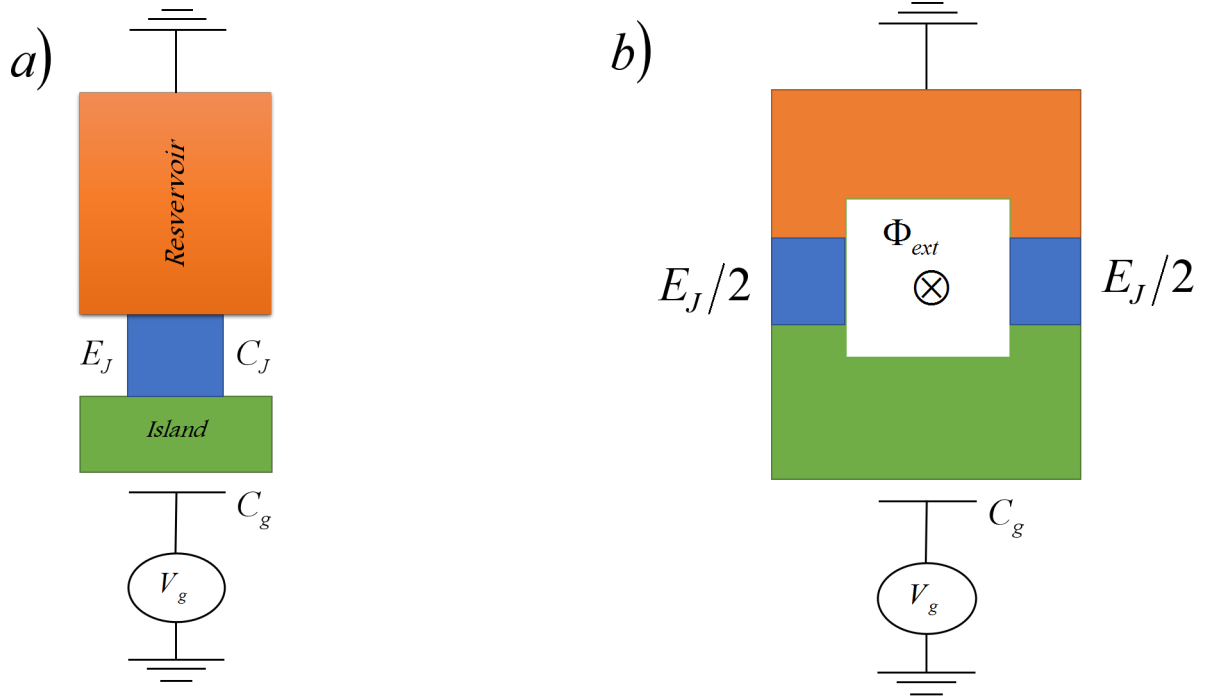


FIGURE II.4 – a) Schematic of the Cooper pair box consisting of a Josephson junction (blue) which connects an island (green) with a reservoir (orange). b) The Josephson junction is replaced by a SQUID in which the qubit becomes more controllable by a magnetic flux.

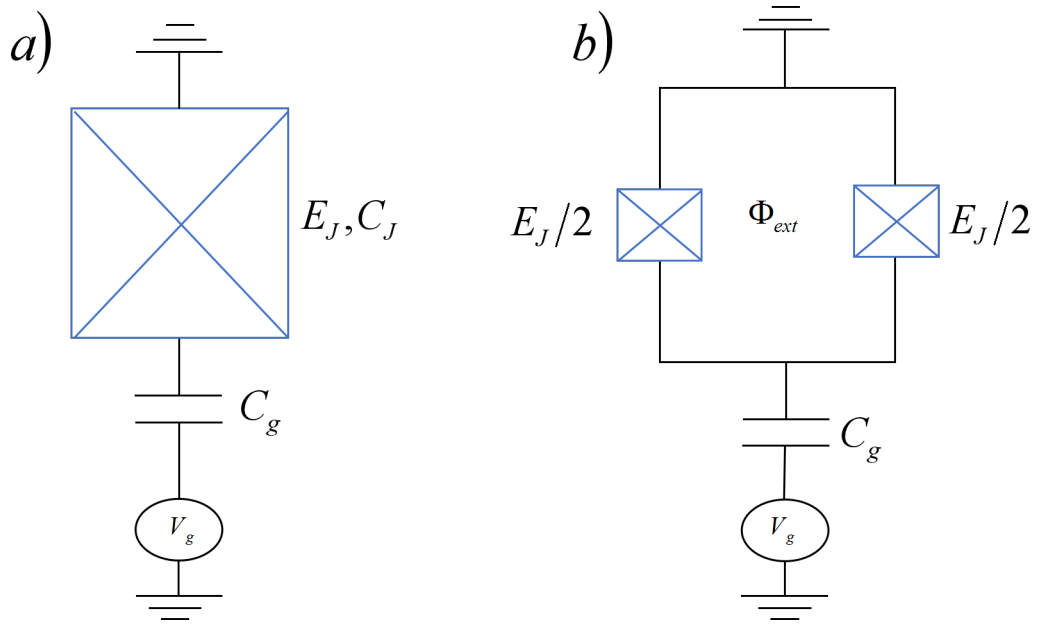


FIGURE II.5 – a) Circuit diagram corresponding to the Cooper pair box schematic in Fig. (II.4a). b) Circuit diagram corresponding to the Cooper pair box schematic in Fig. (II.4b).

$$\begin{aligned}
 K &= \frac{1}{2}C_J V_J^2 + \frac{1}{2}C_g(C_J - V_g)^2 \\
 &= \frac{C_J + C_g}{2} \left(V_J - \frac{C_g}{C_J + C_g} V_g \right)^2 + \frac{1}{2} \left(C_g - \frac{C_g^2}{C_J + C_g} \right)^2.
 \end{aligned} \tag{II.15}$$

By using the relation in equation (II.2) and omitting a constant term (independent of ϕ and $\dot{\phi}$) in equation (II.3) because it does not influence the system dynamics, the Lagrangian can be written as

$$L = \frac{C_\Sigma}{2} \left(\frac{\hbar}{2e} \dot{\phi} - \frac{C_g}{C_\Sigma} V_g \right)^2 - E_J \cos \phi, \tag{II.16}$$

where $C_\Sigma = C_J + C_g$. Here the kinetic energy can be controlled by the external gate voltage, whereas the potential energy, is however fixed by the energy E_J .

As shown in figure (II.5b), the single Josephson junction is replaced by a loop SQUID which consists of two identical junctions ($E_{J,1} = E_{J,2} = E_J/2$), in order to add additional control for potential energy via a magnetic flux. The potential term in the Lagrangian (II.16) can be replaced by the potential term (II.16), the corresponding Lagrangian is then given by

$$L = \frac{C_\Sigma}{2} \left(\frac{\hbar}{2e} \dot{\phi} - \frac{C_g}{C_\Sigma} V_g \right)^2 - E_J (\Phi_{ext}) \cos \phi. \tag{II.17}$$

The canonical momentum operator corresponding to (II.15) with respect to $\dot{\phi}$ is given by $p = \partial K / \partial \dot{\phi} = (\hbar/2e) Q$, (with $Q = (C_J + C_g) V_J - C_g V_g = -2eN$), which implies $(C_J + C_g) V_J^2 = (2e)^2 / (C_J + C_g) (N - C_g N_g / 2e)^2$.

Finally, we can identify the Hamiltonian of the following system :

$$H = \frac{E_c}{2} (N - N_g)^2 - E_J (\Phi_{ext}) \cos \phi, \tag{II.18}$$

where $E_c = (2e)^2 / (C_J + C_g)$ and $N_g = C_g V_g / 2e$.

We consider that the electrostatic energy is dominant compared to the Josephson energy ($E_C \gg E_J$), it is called the charge qubit regime. To quantitatively describe the Cooper pair box, we define the operator \hat{N} which is associated with the number of Cooper pairs in the base $|N\rangle$ as follows

$$\hat{N} = \sum_{N \in \mathbb{Z}} N |N\rangle \langle N|. \tag{II.19}$$

The phase difference ϕ across the Josephson junction presents fluctuations related to N by the

following uncertainty relation : $\Delta N \Delta \phi = 1/2$, assuming that the fluctuations of the number of excess Cooper pairs N is very small to that of ϕ , the canonical commutation relation $[N, \phi] = i$ and $N = i\partial/\partial\phi$, and thus the basis $|\phi\rangle$ can be introduced as

$$|\phi\rangle = \sum_{N \in \mathbb{Z}} e^{-iN\phi} |N\rangle, \quad (\text{II.20})$$

and by using the Fourier transform[112], the number states $|N\rangle$ can be laid to the phase difference $|\phi\rangle$ states

$$|N\rangle = \frac{1}{2\pi} \int_0^{2\pi} d\phi e^{iN\phi} |\phi\rangle. \quad (\text{II.21})$$

From equation (II.21), we notice the following identity $e^{i\phi} |N\rangle \approx |N+1\rangle$, and we have $\cos \phi = (e^{i\phi} + e^{-i\phi})/2 = (|N\rangle \langle N+1| + |N+1\rangle \langle N|)/2$. We can then write the Hamiltonian of the Cooper pair box in the matrix form

$$H = \frac{E_C}{2} \sum_N (N - N_g)^2 |N\rangle \langle N+1| - \frac{E_J}{2} \sum_N (|N\rangle \langle N+1| + |N+1\rangle \langle N|). \quad (\text{II.22})$$

We can diagonalize the Hamiltonian (II.22) and obtain the energy spectrum as a function of the gate charge N_g , which will be composed of a set of parabolas centered around the integer values of N_g . We see that for half-integer values of N_g ($N_g = N + 1/2$, $N \in \mathbb{Z}$) the state of charge is twice degenerate, more precisely the states $|N\rangle$ and $|N+1\rangle$ have the same energy. The Cooper box in the $E_C \gg E_J$ regime is a good two-level system, especially if we skew the grid voltage so that we have $N_g = 0.5$. At this point, the quantum states are the superposition of the symmetric and anti-symmetric of a state corresponding to N Cooper pairs and $N+1$ pairs of Cooper on the superconducting island, we have $|0\rangle = (|N+1\rangle - |N\rangle)/\sqrt{2}$ and $|1\rangle = (|N+1\rangle + |N\rangle)/\sqrt{2}$ as indicated in figure(II.6).

The energy levels of the Hamiltonian (II.22) being very anharmonic, we can restrict to only two levels and thus we can consider the circuit as a quantum bit.

For $N = 0$ the Hamiltonian (II.22) becomes

$$H = \frac{E_C}{2} N_g^2 |0\rangle \langle 0| - \frac{E_J}{2} (|0\rangle \langle 1| + |1\rangle \langle 0|). \quad (\text{II.23})$$

For $N = 1$

$$H = \frac{E_C}{2} (1 - N_g)^2 |1\rangle \langle 1| - \frac{E_J}{2} (|1\rangle \langle 2| + |2\rangle \langle 1|). \quad (\text{II.24})$$

From equations (II.23) and (II.24), one can determine the elements of the matrix of (II.22) in the states of charge $\{|0\rangle, |1\rangle\}$ as follows :

$$H = -\frac{E_C}{2} (1 - 2N_g) \sigma_z - \frac{E_J}{2} \sigma_x, \quad (\text{II.25})$$

where σ_z and σ_x are the Pauli matrices. The Hamiltonian of the charge qubit is therefore written in the following form

$$H = -\frac{1}{2} B_z \sigma_z - \frac{1}{2} B_x \sigma_x, \text{ with } B_z = \frac{E_C}{2} (1 - 2N_g); B_x = E_J. \quad (\text{II.26})$$

The corresponding eigenvalues and eigenstates of this Hamiltonian are given by

$$E_0 = -\frac{1}{2} \sqrt{B_z^2 + B_x^2}; E_1 = \frac{1}{2} \sqrt{B_z^2 + B_x^2}, \quad (\text{II.27})$$

$$|+\rangle = \cos \theta |\uparrow\rangle + \sin \theta |\downarrow\rangle; |-\rangle = -\sin \theta |\uparrow\rangle + \cos \theta |\downarrow\rangle, \quad (\text{II.28})$$

with the expression of θ is given by the following relation $\theta = (1/2) \tan^{-1} [2E_J/E_C (1 - 2N_g)] = (1/2) \tan^{-1} [B_x/B_z]$.

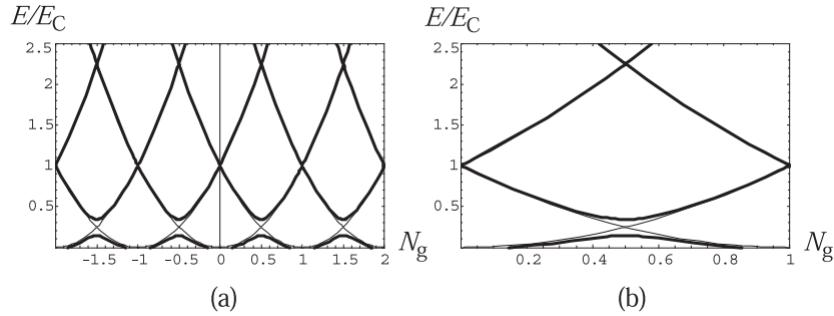


FIGURE II.6 – Energy spectrum of the charge qubit for the ratio as a function of gate charge N_g . The E/E_C is lower, the first two levels are isolated from the third for values of N_g near the half-integer. a) the bold curve designates the energy spectrum of the Hamiltonian with $E_C = 0.2$, the fine curve with $E/E_C = 0$. b) the energy spectrum for $0 \leq N_g \leq 1$.

II.1.4 Transmon qubit

The difference between the transmon qubit and the charge qubit is that the transmon qubit is independent of the gate charge by going to another regime where $E_J \gg E_C$, which is so-called the transmon regime. This is done at the level of the equivalent circuit of the superconducting qubits

by introducing the addition of a large shunting capacitance placed in parallel with the Josephson junction to increase the overall capacitance as illustrated in figure (II.7).

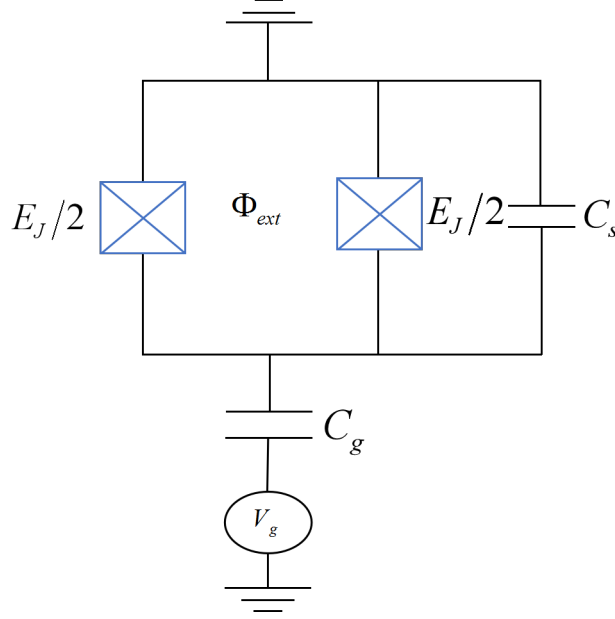


FIGURE II.7 – The equivalent circuit of the Transmon qubit, an additional capacitance (C_s) has been added in parallel to the junction.

The increased E_J/E_C ratio makes the Cooper box less sensitive to gate charge and its anharmonicity, leading to the flattening energy bands, whereas the transmon frequency can be tuned by applying the magnetic flux through the loop of SQUID. Such energy bands are illustrated in figure (II.8), where three eigenenergies E_k ($k=1,2,3$) of the Cooper pair box Hamiltonian (II.22) are shown as a function of gate charge N_g for different values of the ratio E_J/E_C . The sensitivity to charge noise is defined as the charge dispersion, which is the transition energy between two neighboring energy levels

$$\epsilon_k = E_{k,k+1}(N_g = 0.5) - E_{k,k+1}(N_g = 0). \quad (\text{II.29})$$

Owing to the charge dispersion decreases exponentially fast as the ratio E_J/E_C is increased as shown in Ref. [43]

$$\epsilon_k \propto e^{-i\sqrt{8E_J/E_C}}. \quad (\text{II.30})$$

The transmon Hamiltonian is the same as that of the hamiltonian (II.18), with only change being the charging energy E_C :

$$H = \frac{E_C}{2}(N - N_g)^2 - E_J(\Phi_{ext}) \cos \phi, \quad (\text{II.31})$$

where $E_C = (2e)^2 / (C_J + C_g + C_s)$ is the charging energy. Since $E_J/E_C \gg 1$, we can consider that the fluctuations in ϕ in the Hamiltonian (II.31), are very weak and make a development of the cosine of the tunnel energy term $-E_J(\Phi_{ext}) \cos \phi \simeq -E_J(\Phi_{ext}) + (E_J(\Phi_{ext})/2) \phi^2 - (E_J(\Phi_{ext})/24) \phi^4$. The Hamiltonian (II.31) becomes

$$H = \frac{E_C}{2}(N - N_g)^2 - E_J(\Phi_{ext}) + \frac{E_J(\Phi_{ext})}{2}\phi^2 - \frac{E_J(\Phi_{ext})}{24}\phi^4. \quad (\text{II.32})$$

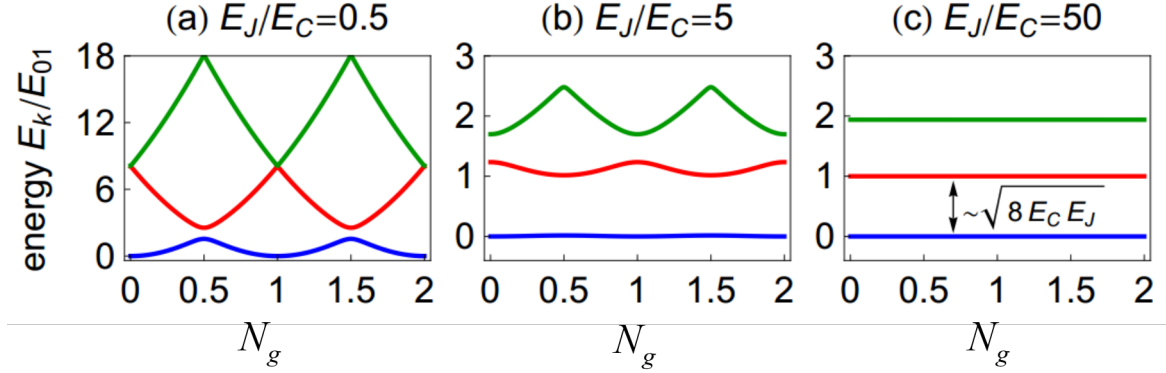


FIGURE II.8 – Eigenenergies for three energy levels ($k = 0, 1, 2$) of the Cooper pair box Hamiltonian (II.31) for different ratios E_J/E_C . For very large E_J/E_C , the spectrum practically becomes that of the harmonic oscillator. The system gets less sensitive to gate charge when the E_J/E_C is increased from the charging regime with $E_J/E_C = 0.5$ (a) to the transmon regime with $E_J/E_C = 50$ (c). The figure used from Ref.[66].

In figure (II.8), we observe that in the Transmon system, the energy levels are independent of the charging shift N_g . Therefore, we can omit this term from the Hamiltonian. Using the gauge transformation $U_t = e^{iN_g\phi}$, and thus

$$H \approx U_t H U_t^\dagger = \frac{E_C}{2} N^2 + \frac{E_J}{2} \phi^2 - E_J - \frac{E_J}{24} \phi^4, \quad (\text{II.33})$$

the first part of this Hamiltonian is clearly that of a harmonic oscillator :

$$H_1 = \frac{\sqrt{8E_J E_C}}{2} \left(\left\{ \left(\frac{E_C}{8E_J} \right)^{1/4} N \right\}^2 + \left\{ \left(\frac{E_J}{8E_C} \right)^{1/4} \phi \right\}^2 \right). \quad (\text{II.34})$$

We can then introduce the bosonic variables $b^+ = (1/\sqrt{2}) (i(8E_C/E_J)^{1/4} N + (E_J/8E_C)^{1/4} \phi)$ and $b = (1/\sqrt{2}) (-i(8E_C/E_J)^{1/4} N + (E_J/8E_C)^{1/4} \phi)$, and therefore we have $N = -(i/2) (E_J/2E_C)^{1/4} (b^+ - b)$ and $\phi = (2E_C/E_J)^{1/4} (b^+ + b)$ where $[b, b^+] = 1$, $b^+ = \sum_J \sqrt{J+1} |J+1\rangle \langle J|$. The Hamil-

tonian (II.33) becomes

$$H = \sqrt{8E_J E_C} \left(b^+ b + \frac{1}{2} \right) - E_J - \frac{E_C}{12} (b^+ + b)^4. \quad (\text{II.35})$$

The corresponding eigen-energies are separated by the energy quantum $\sqrt{8E_J E_C}$.

In the transmon regime, the charging energy determines the non-linearity of the oscillator through its anharmonicity α

$$\alpha = E_{12} - E_{01} = -E_C. \quad (\text{II.36})$$

Finally, the flat energy bands enable the assignment of a unique frequency to each energy level of the states $|J\rangle$. So the Hamiltonian is written in the form

$$H = \hbar \sum_J \omega_J |J\rangle \langle J|. \quad (\text{II.37})$$

For the first two levels, the Hamiltonian in equation (II.37) becomes

$$H = \hbar \frac{\omega_q}{2} \sigma_z, \quad (\text{II.38})$$

where $\omega_q = \omega_2 - \omega_1$ is the qubit transition frequency, $\sigma_z = |0\rangle \langle 0| - |1\rangle \langle 1|$.

II.2 Cavity quantum electrodynamics

Cavity quantum electrodynamics is the physical theory describing the interaction between light and matter schematically represented in Fig. (II.9), which studies the interaction between atoms represented by a two-level system and the quantized electromagnetic mode inside a cavity. Cavity QED is interesting in fundamental physics, as well as for applications in quantum information processing.

II.2.1 Quantification of the field in a cavity

We consider a cavity of length L of two perfect mirrors as shown in Fig. (II.10). Maxwell's equations :

$$\nabla \cdot E = 0, \quad \nabla \cdot B = 0, \quad (\text{II.39})$$

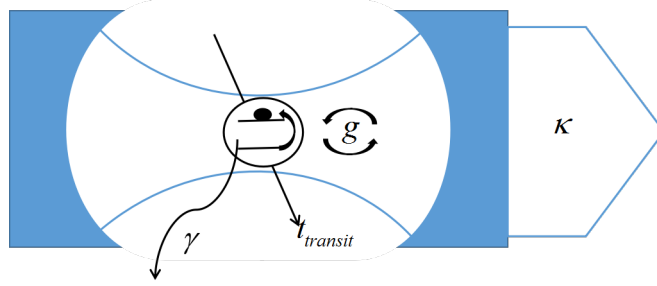


FIGURE II.9 – QED cavity architecture includes an electromagnetic field mode of decay rate κ coupled to a two-level system of decay rate γ and the transition time $t_{transit}$ with a coupling force g .

$$\nabla \times E = -\frac{\partial B}{\partial t}, \quad \nabla \times B = \mu_0 \varepsilon_0 \frac{\partial E}{\partial t}, \quad (\text{II.40})$$

where μ_0 and ε_0 are the vacuum permeability and permittivity. The electric field is polarized along the x axis, $\vec{E}(r, t) = E_x(z, t) \vec{e}_x$. The boundary conditions impose the following decomposition $E_x(z, t) = [2\omega^2/(V\varepsilon_0)]^{1/2} q(t) \sin(kz)$, with $k_n = n\pi/L$ ($n \succ 0$), $\omega_n = ck_n$, and V is the effective volume of the cavity, and $q(t)$ is the amplitude of normal mode n . From Maxwell's equations (II.39) and (II.40), we readily get the expression of the magnetic field $\vec{B}(r, t) = B_y(z, t) \vec{e}_y$, $B_y(z, t) = (\mu_0 \varepsilon_0 / k) (2\omega^2 / V \varepsilon_0) p(t) \cos(kz)$, where $p(t) = \dot{q}(t)$ is the canonical momentum operator conjugate to q . By using Poynting's theorem, we obtain the energy of the electromagnetic field in the cavity :

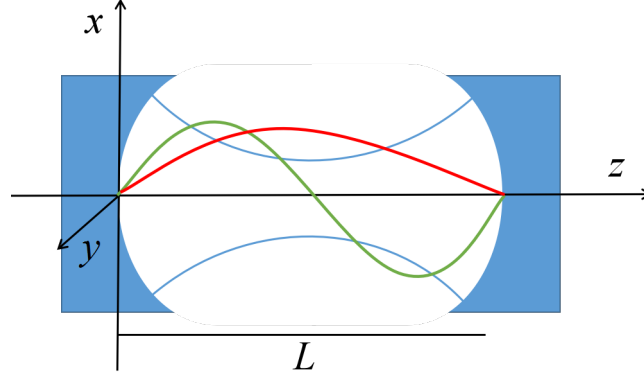


FIGURE II.10 – An electromagnetic cavity of length L , the electric field must therefore be zero at the extremities of the cavity.

$$H = \frac{1}{2} \int dV \left(\varepsilon_0 E_x^2(z, t) + \frac{1}{\mu_0} B_y^2(z, t) \right). \quad (\text{II.41})$$

We replace the expressions of the electric and magnetic field as mentioned above in this expression, then using the trigonometric relations $\sin^2(kz) = (1 - \cos(2kz))/2$, $\cos^2(kz) = (1 + \cos(2kz))/2$, we finally find the following expression

$$H = \frac{1}{2} (p^2 + \omega^2 q^2). \quad (\text{II.42})$$

By moving from the classical variables p and q to their quantum operators, which are given by

$$\tilde{p} = i\sqrt{\frac{\omega}{2}} (a^+ - a); \quad \tilde{q} = i\sqrt{\frac{1}{2\omega}} (a^+ + a). \quad (\text{II.43})$$

where \tilde{p} and \tilde{q} obey the canonical commutation relation $[\tilde{q}, \tilde{p}] = i\hbar$, the quantum Hamiltonian of the field is written in the following form

$$H = \hbar\omega \left(a^+ a + \frac{1}{2} \right). \quad (\text{II.44})$$

II.2.2 Jaynes-Cummings model

We now consider the atom, described as a two-level system whose Hamiltonian, $H_{atom} = (\hbar\Omega/2) \sigma_z$, as indicated in the diagram(II.11).

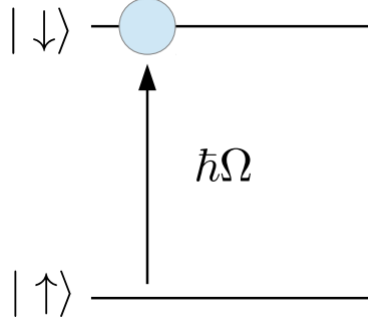


FIGURE II.11 – Two level atom.

We can now study the interaction between the two-level atom and the quantized field. The Hamiltonian system is divided into three parts

$$H = H_{atom} + H_{field} + H_{inter}, \quad (\text{II.45})$$

where H_{atom} is the Hamiltonian of a two-level atom, $H_{field} = \hbar\omega_r a^\dagger a$ is the Hamiltonian of the quantized field and H_{inter} is the interaction Hamiltonian between the atom and the quantized field.

II.2.3 Approximation of the dipole moment and the rotating wave

The coupling between an atom and an electromagnetic wave is dominated by the coupling of the electric field with the electric dipole. The interaction Hamiltonian can therefore be written as

$$H_{inter} = -\tilde{d} \cdot \tilde{E}, \quad (\text{II.46})$$

where the dipole operator is written as $\tilde{d} = d\sigma_x$, and from the expression of the electric field and equation (II.43). We therefore can write the field operator

$$\tilde{E} = \left(\frac{\omega}{V\epsilon_0} \right)^{\frac{1}{2}} \sin(kz) (a^\dagger + a). \quad (\text{II.47})$$

Finally, the interaction Hamiltonian (II.46) becomes

$$H_{inter} = \hbar g (\sigma^+ + \sigma^-) (a + a^\dagger), \quad (\text{II.48})$$

where $g = g_{rms}/\hbar$ ($g_{rms} = \sqrt{\omega/V\epsilon_0} \sin(kz)$), while $\sigma^- = |\uparrow\rangle \langle \downarrow|$ and $\sigma^+ = |\downarrow\rangle \langle \uparrow|$ are Pauli matrices expressed in terms of the ground $|0\rangle$ and excited $|1\rangle$ atom states. The Hamiltonian of the system

(II.45) then becomes

$$H = \hbar\omega_r a^\dagger a + \frac{\hbar\Omega}{2}\sigma_z + \hbar g (\sigma^+ + \sigma^-) (a^\dagger + a). \quad (\text{II.49})$$

The Jaynes-Cummings Hamiltonian can be derived from the Hamiltonian (II.49) by using the rotating wave approximation (RWA). The RWA is valid in the regime where $g \ll \omega_r, \Omega$. The terms $\sigma^+ a (\sigma^- a^\dagger)$ correspond to the processes of excitation (de-excitation) of the atom and a photon is created(annihilated) in the cavity mode. The two other terms corresponding to the excitation (de-excitation) of both the atom and the cavity field mode do not conserve energy. In the RWA regime, these two terms can be neglected. Within the framework of this approximation, we obtain the Hamiltonian corresponding to the Jaynes-Cummings model[113]

$$H = \hbar\omega_r a^\dagger a + \frac{\hbar\Omega}{2}\sigma_z + \hbar g (a\sigma^+ + a^\dagger\sigma^-). \quad (\text{II.50})$$

We can transform this expression into a more practical form, by introducing the following excitation number operator $N \simeq a^\dagger a + \sigma_z/2$, the Hamiltonian (II.50) can be rewritten as

$$H = \hbar\omega_r N + \frac{\hbar\Delta}{2}\sigma_z + \hbar g (a\sigma^+ + a^\dagger\sigma^-), \quad (\text{II.51})$$

where $\Delta = \Omega - \omega_r$ is the atom-cavity detuning. We can easily demonstrate the following commutation relation $[H, N] = 0$. The stationary states of the system without coupling ($g = 0$) are

$$|\downarrow, n\rangle = |\downarrow\rangle \otimes |n\rangle, \quad |\uparrow, n\rangle = |\uparrow\rangle \otimes |n\rangle. \quad (\text{II.52})$$

The interaction Hamiltonian H_{inter} couples these two-by-two states $|\uparrow, n\rangle$ with $|\downarrow, n+1\rangle$. Only the fundamental level $|\uparrow, 0\rangle$ is not coupled to any other state

$$H_{\text{inter}} |\uparrow, 0\rangle = 0, \quad (\text{II.53})$$

$$H_{\text{inter}} |\downarrow, 0\rangle = \hbar g |\uparrow, 1\rangle, \quad H_{\text{inter}} |\uparrow, 1\rangle = \hbar g |\downarrow, 0\rangle, \quad (\text{II.54})$$

$$H_{\text{inter}} |\downarrow, n\rangle = \hbar g \sqrt{n+1} |\uparrow, n+1\rangle, \quad H_{\text{inter}} |\uparrow, n+1\rangle = \hbar g \sqrt{n+1} |\downarrow, n\rangle. \quad (\text{II.55})$$

In the double states $\{|\downarrow, n\rangle, |\uparrow, n+1\rangle\}$, the Hamiltonian (II.51) is then written

$$H = \hbar\omega_r (n+1) \begin{pmatrix} 1 & 0 \\ 0 & 1 \end{pmatrix} + \frac{\hbar}{2} \begin{pmatrix} -\Delta & 2g\sqrt{n+1} \\ 2g\sqrt{n+1} & \Delta \end{pmatrix}. \quad (\text{II.56})$$

The eigen-energies of the Hamiltonian (II.51) are

$$E_{+,n} = \hbar\omega_r (n+1) + \frac{\hbar}{2} \sqrt{4g^2 (n+1) + \Delta^2}, E_{-,n} = \hbar\omega_r (n+1) - \frac{\hbar}{2} \sqrt{4g^2 (n+1) + \Delta^2}, \quad (\text{II.57})$$

and the corresponding states are given by

$$|+, n\rangle = \cos \theta_n |\downarrow, n\rangle + \sin \theta_n |\uparrow, n+1\rangle, |-, n\rangle = -\sin \theta_n |\downarrow, n\rangle + \cos \theta_n |\uparrow, n+1\rangle, \quad (\text{II.58})$$

while the egen-energy of the ground state $|\uparrow, 0\rangle$ is

$$\frac{-\hbar\Delta}{2}, \quad \text{and} \quad \theta_n = \left(\frac{1}{2}\right) \tan^{-1} \left(\frac{2g\sqrt{n+1}}{2}\right). \quad (\text{II.59})$$

II.2.4 Resonance regime and dispersive regime

Resonance regime ($\Delta = 0$)

In the resonant case, characterized by $\Delta = 0$, the eigenstates are the combinations of symmetric and anti-symmetric of the states $|\downarrow, n\rangle$ and $|\uparrow, n+1\rangle$ ($|\pm, n\rangle = (1/\sqrt{2})(|\uparrow, 1\rangle \pm |\downarrow, 0\rangle)$), and the interaction term lifts the degeneracy of these states. This situation is illustrated in Figure (II.12).

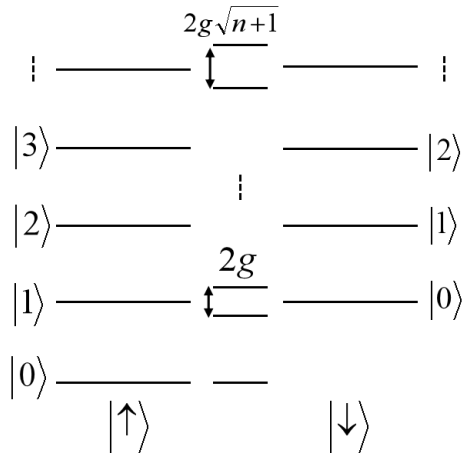


FIGURE II.12 – Energy diagram in the resonant case.

Dispersive regime ($\Delta \gg g$)

We now describe the dispersive case in which the atom is operated at a frequency for which the detuning Δ between atom and cavity are large. In this case, no exchanging excitations between atom and cavity, and the eigenstates take the form

$$|+, n\rangle \simeq |\downarrow, n\rangle + \frac{g\sqrt{n+1}}{\Delta} |\uparrow, n+1\rangle, |-, n\rangle \simeq -\frac{g\sqrt{n+1}}{\Delta} |\downarrow, n\rangle + |\uparrow, n+1\rangle. \quad (\text{II.60})$$

As shown in figure (II.13), the energies of the eigenstates are shifted by the coupling. In this regime, the energy exchange between the qubit and the resonator field is difficult. By applying the unitary transformation, $U = \exp(\lambda(a\sigma^+ - a^+\sigma^-))$ with $\lambda = g/\Delta \ll 1$, it is possible to obtain an approximate effective Hamiltonian

$$H_{eff} = U H U^\dagger \approx \hbar \left(\omega_r + \frac{g^2}{\Delta} \sigma_z \right) a^\dagger a + \frac{\hbar}{2} \left(\Omega + \frac{g^2}{\Delta} \right) \sigma_z. \quad (\text{II.61})$$

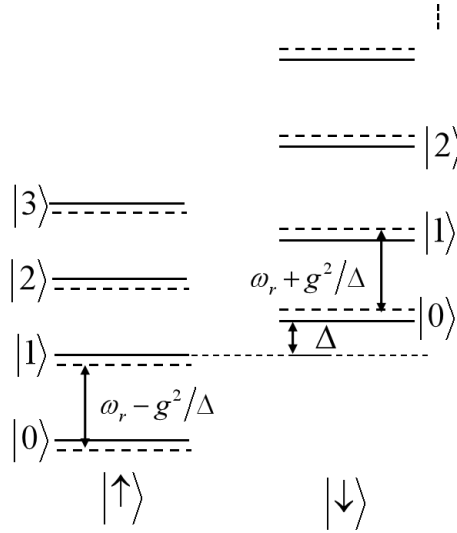


FIGURE II.13 – Energy diagram in the dispersive regime.

II.3 Circuit quantum electrodynamics

Circuit quantum electrodynamics (circuit QED) is an analog of cavity quantum electrodynamics, which is proposed by Blais[44]. Such a circuit QED is realized in an electrical circuit by coupling capacitively a superconducting qubit to a coplanar resonator (playing the role of the cavity) or the quantum harmonic LC oscillator.

II.3.1 Quantum harmonic LC oscillator

The quantum LC oscillator is the simplest quantum circuit as shown in figure (II.14), it consists of a capacitor C in series with an inductance L . By using the Kirchhoff's rule for quantum circuit shown in Fig. (II.14), we find the following equation of motion

$$L \frac{d\dot{Q}}{dt} + \frac{Q}{C} = 0. \quad (\text{II.62})$$

Using the following Euler-Lagrangian equation $d(\partial L_r / \partial \dot{Q}) / dt - \partial L_r / \partial Q = 0$, we can determine the Lagrangian of the system

$$L_r = \frac{L}{2} \dot{Q}^2 - \frac{Q^2}{2C}. \quad (\text{II.63})$$

The corresponding conjugate moment $p = \partial L_r / \partial \dot{Q} = L\dot{Q}$. Therefore, the Hamiltonian is written in the following form

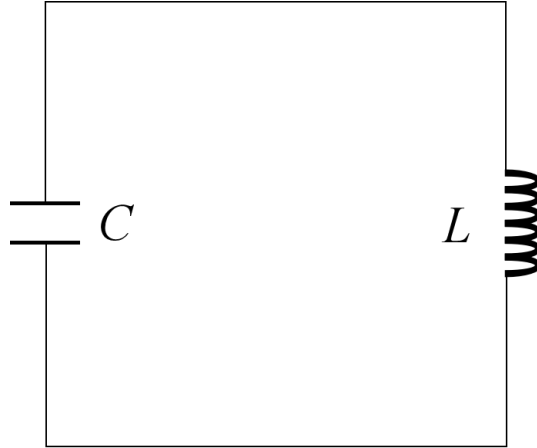


FIGURE II.14 – Energy diagram in the dispersive regime.

$$H = \frac{\Phi^2}{2L} + \frac{Q^2}{2C}. \quad (\text{II.64})$$

The flux Φ in the inductor can be chosen as a position variable, whereas the charge Q of the capacitor can be seen as its conjugate variable, $[\Phi, Q] = i\hbar$. We introduce a^+ and a to diagonalize the hamiltonian with the quantum harmonic oscillator. Q and Φ can thus be written as $a = -i\Phi / \sqrt{2\hbar\omega_r L} + Q / \sqrt{2\hbar\omega_r C}$ and $a^+ = i\Phi / \sqrt{2\hbar\omega_r L} + Q / \sqrt{2\hbar\omega_r C}$. We then plug these

expressions in equation (II.64) we get

$$H = \hbar\omega_r \left(a^\dagger a + \frac{1}{2} \right), \quad (\text{II.65})$$

where $\omega_r = 1/\sqrt{LC}$.

II.3.2 Transmission line (Coplanar waveguide)

The aim of this section is to obtain a quantum description of the electromagnetic field inside a transmission line. We use the standard approach of modeling the line as a set of inductors in parallel with capacitors as shown (II.15).

We assume inductance l and capacitance c per unit the length of the line. Each segment of the line of the length dx has an inductance ldx in parallel with a capacitance cdx , as shown in figure(II.16). We apply Kirchhoff's rule to this figure, and we find the following equation $V(x, t) = ldx\partial I(x, t)/\partial t + V(x + dx, t)$ (i.e $V(x + dx, t)/dx - V(x, t)/dx = l\partial I(x, t)/\partial t$). Finally, we find the following constitutive relation

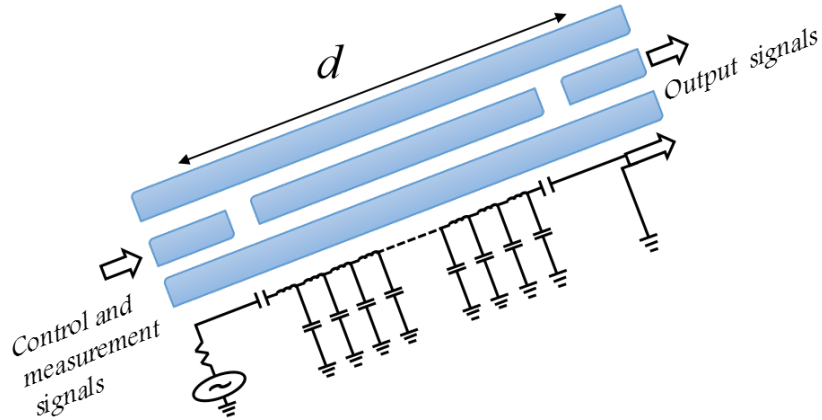


FIGURE II.15 – Representation of the transmission line by a set of inductors in parallel with capacitors.

$$l\partial_t I(x, t) + \partial_x V(x, t) = 0. \quad (\text{II.66})$$

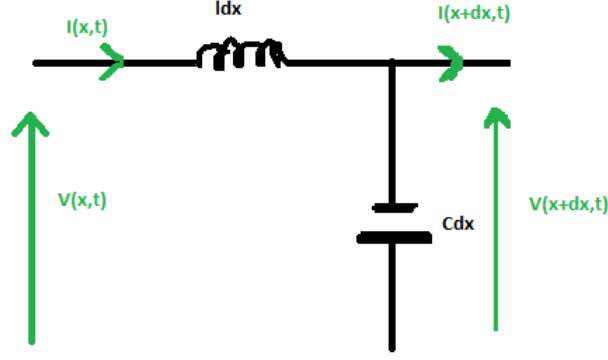


FIGURE II.16 – Representation of an inductor in parallel with the capacitor.

We choose the generalized flux as the degree of freedom instead of choosing current or voltage, the generalized flux is defined as $\Phi(x, t) = \int V(x, t) dx$. By replacing the expression of $V(x, t)$ in equation (II.66), we find the expression of the current $I(x, t) = (1/l) \partial_x \Phi(x, t)$. The Lagrangian of the system is given by

$$L_g = \int_{-\frac{d}{2}}^{\frac{d}{2}} dx L(x, t) = \int_{-\frac{d}{2}}^{\frac{d}{2}} dx \left[\frac{c}{2} (\partial_t \Phi)^2 - \frac{1}{2l} (\partial_x \Phi)^2 \right]. \quad (\text{II.67})$$

The associated Euler-Lagrange equations are those of a wave propagating at the speed $\nu = 1/\sqrt{lc}$. By using boundary conditions ($\Phi(d/2, t) = \Phi(-d/2, t) = 0$), $\Phi(x, t)$ can be written under the form

$$\Phi(x, t) = \sqrt{\frac{2}{d}} \sum_{k_0=1} \phi_{k_0}(t) \cos\left(\frac{k_0 \pi x}{d}\right) + \sqrt{\frac{2}{d}} \sum_{k_e=2} \phi_{k_e}(t) \sin\left(\frac{k_e \pi x}{d}\right). \quad (\text{II.68})$$

We replace (II.27) in (II.66), the Lagrangian L_g is then written in terms of the new variables $\phi_k(t)$ ($k = k_0, k_e$)

$$L_g = \sum_k \frac{c}{2} (\dot{\phi}_k)^2 - \frac{1}{2l} \left(\frac{k\pi}{d} \right)^2 (\phi_k)^2. \quad (\text{II.69})$$

It is the Lagrangian of the sum of decoupled harmonic oscillators. The calculation of the moments p_k combined with the variables $\phi_k : p_k = c\dot{\phi}_k$ by the Legendre transformation, then the commutation relation is $[a_k, a_{k'}^\dagger] = \delta_{k,k'}$. The Hamiltonian of the resonator is then written

$$H = \sum_k \omega_k \left(a_k^\dagger a_k + \frac{1}{2} \right), \quad (\text{II.70})$$

where $\omega_k = (k\pi/d) \nu$, $a_k = -i\sqrt{(k\pi/2\hbar)} \sqrt{c/l} \tilde{\phi}_k + \sqrt{(d/2\hbar k\pi)} \sqrt{l/c} \tilde{p}_k$ and $a_k^\dagger = i\sqrt{(k\pi/2\hbar)} \sqrt{c/l} \tilde{\phi}_k +$

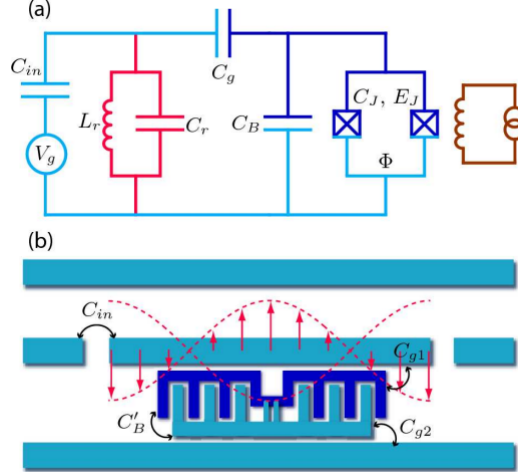


FIGURE II.17 – Circuit QED for the transmon qubit : (a) The transmon qubit is coupled to the LC resonator through a gate capacitance C_d . The two Josephson junctions, with capacitance C_J and Josephson energy E_J , are in parallel with an additional large capacitance C_B . (b) The transmon device consists of a transmon qubit coupled to a transmission line. The figure used from Ref.[43].

$$\sqrt{(d/2\hbar k\pi)} \sqrt{l/c\tilde{p}_k}.$$

II.3.3 Coupling a transmon-type superconducting qubit to a coplanar waveguide resonator

The coupling between the transmon-type superconducting qubit and the coplanar waveguide resonator is an electrostatic capacitive interaction. Such a transmon is located at the center of a transmission line resonator, as shown in Fig.(II.17b). As seen in Fig. (II.17a), the transmon qubit is capacitively coupled to the resonator in the equivalent circuit of the transmon-resonator system (figure II.17b), it is composed of two Josephson junctions, which are hijacked by two large capacitances C_g and C_B . These large capacities lead to low charge energy, $E_c = (2e)^2/C_t$ with $C_t = C_B + C_g + C_J$ which distinguishes the transmon from the charge qubit.

The coupling between the transmon and the resonator is demonstrated by following an approach similar to that used for dissipation in the cavity. The standing wave in the resonator (Fig. II.17(b)) induces tension between the two islands. We consider a capacitive coupling between these two devices, the interaction Hamiltonian takes the following form

$$H_{\text{inter}} = 2 \frac{C_g}{C_t} e V_{rms}^0 \tilde{N} (a + a^+), \quad (\text{II.71})$$

where $\omega_r = 1/\sqrt{L_r C_r}$ is the resonator frequency, and $V_{rms}^0 = \sqrt{\hbar \omega_r / C_r}$. The total Hamiltonian of the system is then written

$$H = \frac{E_c}{2}(N - N_g)^2 - E_J \cos \phi + \hbar \omega_r a^\dagger a + 2\beta e V_{rms}^0 \tilde{N} (a + a^\dagger), \quad (\text{II.72})$$

where $\beta = C_g/C_t$. We can rewrite the Hamiltonian in terms of the eigenstates of the transmon $|i\rangle$, we then obtain the generalized Jaynes-Cummings Hamiltonian

$$H = \sum_j \omega_j |j\rangle \langle j| + \hbar \omega_r a^\dagger a + \hbar \sum_{ij} g_{ij} |i\rangle \langle j| (a + a^\dagger), \quad (\text{II.73})$$

where $\hbar g_{ij} = 2\beta e V_{rms}^0 \langle i | \tilde{N} | j \rangle$ are nearest-neighbor energy levels of the coupling, with $|\langle j+1 | \tilde{N} | j \rangle| \approx \sqrt{(j+1)/2} (E_J/8E_c)^{1/2}$.

We omit the terms corresponding to a double excitation and a double desexcitation, we obtain the generalized Hamiltonian of Jaynes-Cummings

$$H = \hbar \sum_j \omega_j |j\rangle \langle j| + \hbar \omega_r a^\dagger a + \hbar \sum_i g_{i,i+1} |i\rangle \langle i+1| + h.c. \quad (\text{II.74})$$

With sufficient anharmonicity for a transmon system, we can keep only the first two levels, the Hamiltonian (II.74) becomes Jaynes-Cummings in equation (II.49).

Similar to cavity quantum electrodynamics, we will be able to describe a dispersive regime in circuit quantum electrodynamics. This is done when the detuning $\Delta = \omega_q - \omega_r$ between the transmon and resonator is large. We diagonalize the Hamiltonian (II.74), by applying the unitary transformation $D = e^{S-S^\dagger}$, with $S = \sum_i \beta_i a |i+1\rangle \langle i|$ ($\beta_i = g_{i,i+1}/(\omega_{i,i+1} - \omega_r)$). We use the "Baker-Campbell-Hausdorff[63]" relation and keeping the terms up to $g_{i,i+1}^2/\Delta_i^2$ ($\Delta_i = \omega_{i,i+1} - \omega_r$), we get

$$\begin{aligned} H_{eff} = D H D^\dagger &= \hbar \sum_j \omega_j |i\rangle \langle i| + \hbar \omega_r a^\dagger a + \hbar \sum_i \chi_{i,i+1} |i+1\rangle \langle i+1| - \hbar \chi_{01} |0\rangle \langle 0| \\ &+ \hbar \sum_{i=1} (\chi_{i-1,i} - \chi_{i,i+1}) a^\dagger a |i\rangle \langle i| + \hbar \sum_i \eta_i a a |i+2\rangle \langle i| + h.c., \end{aligned} \quad (\text{II.75})$$

where $\chi_{i,i+1} = g_{i,i+1}^2/(\omega_{i,i+1} - \omega_r)$ and $\eta_i = g_{i,i+1}g_{i+1,i+2}/[2(\omega_{i+1} - \omega_i - \omega_r)(\omega_{i+2} - \omega_{i+1} - \omega_r)]$.

The last term η_i corresponding to two-photon transitions can be neglected from $\chi_{i,i+1}$. Then, equation (II.75) becomes

$$H_{eff} = \frac{\hbar}{2} \underbrace{(\omega_{01} + \chi_{01})}_{\omega'_{01}} \sigma_z + \hbar \underbrace{\left(\omega_r - \frac{1}{2}\chi_{12}\right)}_{\omega'_r} a^\dagger a + \hbar \underbrace{\left(\chi_{01} - \frac{\chi_{12}}{2}\right)}_{\chi} \sigma_z a^\dagger a. \quad (\text{II.76})$$

Finally, the dispersive Hamiltonian can be written as

$$H_{eff} = \hbar \frac{\omega'_{01}}{2} \sigma_z + \hbar (\omega'_r + \chi \sigma_z) a^\dagger a. \quad (\text{II.77})$$

II.4 Quantum gates with superconducting device

II.4.1 Single-qubit gates

X-rotation gate for one qubit

Applying the classical field polarized according to e_x , $\vec{E}(t) = (E_0 e^{-i(\omega t + \theta)} + E_0^* e^{i(\omega t + \theta)}) \vec{e}_x$ (where E_0 and θ are the complex amplitude of the field and the frequency) introduces a dipole interaction between the transmon-type superconducting qubit and the microwave field. Within the framework of the dipole approximation, we get

$$H_{dis} = -\vec{d} \cdot \vec{E}(r, t), \quad (\text{II.78})$$

d is the dipole moment for the two-level system. Now, introducing the following relation ($|e\rangle \langle e| + |g\rangle \langle g| = 1$) then equation (II.78) becomes $H_{dis} = -(\rho_{ab} \sigma_+ + \rho_{ba} \sigma_-) E(t)$, where $\rho_{ab} = \langle a | d_x | b \rangle$ are the matrix elements of the electric dipole moment. On the other hand, we can rewrite the Hamiltonian expression as follows

$$H_{disp} = -\hbar \Omega_R (\sigma_+ + \sigma_-) (e^{-i(\omega t + \phi)} + e^{i(\omega t + \phi)}), \quad (\text{II.79})$$

with $\Omega_R = |\rho_{ab}| |E_0| / \hbar$ is the classical Rabi frequency which characterizes the exchange of energy between the qubit and the field mode. By applying the unitary transformation $U(t) = e^{-i(H_0/\hbar)t}$, where $H_0 = (\hbar \omega_0 / 2) \sigma_z$. The interaction Hamiltonian becomes

$$H_I(t) = -\hbar \Omega_R (\sigma_+ e^{i\omega_0 t} + \sigma_- e^{-i\omega_0 t}) (e^{-i(\nu t + \phi)} + e^{i(\nu t + \phi)}). \quad (\text{II.80})$$

We choose $\phi = 0$ and when $\nu = \omega_0$, we obtain the Hamiltonian corresponding to a rotation around the x -axis of the following Bloch sphere

$$H_{\sigma_x} = \hbar \Omega_R (\sigma_+ + \sigma_-) \equiv \hbar \Omega_R \sigma_x. \quad (\text{II.81})$$

The corresponding evolution operator is $U(t) = e^{-i(H_{\sigma_x}/\hbar)t}$. By using the Taylor expansion,

the matrix form is given by

$$U_{\sigma_x}(t) = \begin{pmatrix} \cos(\Omega_R t) & -i \sin(\Omega_R t) \\ -i \sin(\Omega_R t) & \cos(\Omega_R t) \end{pmatrix}, \quad (\text{II.82})$$

therefore

$$R_x(\theta) = \begin{pmatrix} \cos\left(\frac{\theta}{2}\right) & -i \sin\left(\frac{\theta}{2}\right) \\ -i \sin\left(\frac{\theta}{2}\right) & \cos\left(\frac{\theta}{2}\right) \end{pmatrix}, \quad (\text{II.83})$$

where $\theta = 2\Omega_R t$ is the angle of rotation.

Y-rotation gate for one qubit

The rotation around the y -axis in the Bloch sphere corresponds to the X -rotation with the phase difference of $\pi/2$. Therefore, we have chosen $\phi = \pi/2$ in equation (II.79), and we obtain the following interaction Hamiltonian

$$H = \hbar\Omega_R (i\sigma_- - i\sigma_+) = \hbar\Omega_R \sigma_y. \quad (\text{II.84})$$

The corresponding evolution operator is given by $U_{\sigma_y}(t) = e^{-i\Omega_R \sigma_y t}$. Therefore, the matrix form is given by

$$U_{\sigma_y}(t) = \begin{pmatrix} \cos(\Omega_R t) & -\sin(\Omega_R t) \\ \sin(\Omega_R t) & \cos(\Omega_R t) \end{pmatrix}, \quad (\text{II.85})$$

which implies

$$R_y = \begin{pmatrix} \cos\left(\frac{\theta}{2}\right) & -\sin\left(\frac{\theta}{2}\right) \\ \sin\left(\frac{\theta}{2}\right) & \cos\left(\frac{\theta}{2}\right) \end{pmatrix}. \quad (\text{II.86})$$

Z-rotation gate for one qubit

With the change of the phase, it is not possible to obtain the matrix σ_z in the equation (II.79), it is necessary to use the dispersive regime $\Delta \gg \Omega_R$. The interaction Hamiltonian is then written

$$H_{\sigma_z} = \hbar \frac{\Omega_R^2}{\Delta} \sigma_z. \quad (\text{II.87})$$

In the same way as before, we find the corresponding matrix form of the evolution operator ($U_{\sigma_z}(t) = e^{-(i/\hbar)H_{\sigma_z}t}$)

$$U_{\sigma_z}(t) = \begin{pmatrix} e^{-i\frac{\Omega_R^2}{\Delta}t} & 0 \\ 0 & e^{i\frac{\Omega_R^2}{\Delta}t} \end{pmatrix}. \quad (\text{II.88})$$

Finally, we thus find the rotation around the z -axis with $\theta/2 = (\Omega_R^2/\Delta)t$

$$R_z(\theta) = \begin{pmatrix} e^{-i\frac{\theta}{2}} & 0 \\ 0 & e^{i\frac{\theta}{2}} \end{pmatrix}. \quad (\text{II.89})$$

II.4.2 Two-qubit gates

$\sqrt{i\text{SWAP}}$ gate

The following Hamiltonian describes the capacitive coupling of the two superconducting qubits[62]

$$H_{2q} = -\frac{\omega_1}{2}\sigma_z^1 - \frac{\omega_2}{2}\sigma_z^2 + g_{qq}(\sigma_+^1\sigma_-^2 + \sigma_-^1\sigma_+^2), \quad (\text{II.90})$$

where ω_j ($j = 1, 2$) are transition frequencies between the two lowest energy states $|0\rangle_j$ and $|1\rangle_j$, and g_{qq} is the coupling frequency[62]. On resonance ($\omega_1 = \omega_2$), the frequencies will keep on resonance during an operation time. In the two-qubit basis $\{|00\rangle, |01\rangle, |10\rangle, |11\rangle\}$, the evolution operator $U_{\text{int}}(t)$ corresponding to $H_{\text{int}} = g_{qq}(\sigma_+^1\sigma_-^2 + \sigma_-^1\sigma_+^2)$ can be expressed as

$$U_{\text{int}}(t) = \begin{pmatrix} 1 & 0 & 0 & 0 \\ 0 & \cos(g_{qq}t) & -i\sin(g_{qq}t) & 0 \\ 0 & -i\sin(g_{qq}t) & \cos(g_{qq}t) & 0 \\ 0 & 0 & 0 & 1 \end{pmatrix}. \quad (\text{II.91})$$

This swapping evolution allows the implementation of a universal two-qubit gate that allows the preparation of maximally entangled two-qubit states, when switching on the interaction time $t = \pi/(4g_{qq})$, one realizes the \sqrt{iSWAP} gate, represented by the following matrix

$$U_{\text{int}}\left(\frac{\pi}{4g_{qq}}\right) = \begin{pmatrix} 1 & 0 & 0 & 0 \\ 0 & 1/\sqrt{2} & i/\sqrt{2} & 0 \\ 0 & i/\sqrt{2} & 1/\sqrt{2} & 0 \\ 0 & 0 & 0 & 1 \end{pmatrix} = \sqrt{iSWAP}, \quad (\text{II.92})$$

which forms universal set of gates together with single qubit gates. More details about the implementation with the superconducting device and characterization by QPT of this gate can be found in Ref.[62]. In addition, the combination of more than one \sqrt{iSWAP} gate with single qubit gates allows generating a three-qubit GHZ-state[49] and implementing two-qubit Grover's algorithm[114] with the superconducting devices, as well as a 10-qubit GHZ-state with a transmon device[52].

Two-qubit C-Phase gate

Another coupling is the ZZ- interaction, which arises in many experimental approach such as flux[40] and charge[42] qubits, where the coupling between qubit 1 and 2 is described by the interaction Hamiltonian

$$H_{ZZ} = \frac{E_{1,2}^{ZZ}}{4} \sigma_z^1 \otimes \sigma_z^2, \quad (\text{II.93})$$

where $E_{1,2}^{ZZ}$ is the coupling energies. The corresponding unitary time-evolution of this interaction in the two-qubit basis is given by $U_{ZZ} = \exp(-iH_{ZZ}t)$. For $t = \pi/E_{1,2}^{ZZ}$, the matrix form of U_{ZZ} can be expressed by

$$U_{ZZ} = e^{i\frac{\pi}{4}} \begin{pmatrix} 1 & 0 & 0 & 0 \\ 0 & -i & 0 & 0 \\ 0 & 0 & -i & 0 \\ 0 & 0 & 0 & 1 \end{pmatrix}. \quad (\text{II.94})$$

By combining this unitary operation with rotations around z of each qubit, $R_z^1(-\pi/2)$ and

$R_z^2(\pi/2)$, leading to the conditional-phase(c-Phase) gate[17],

$$cP_{11} = \left[R_z^1(-\pi/2) \otimes R_z^2(\pi/2) \right] U_{ZZ} = e^{i\frac{\pi}{2}} \begin{pmatrix} 1 & 0 & 0 & 0 \\ 0 & 1 & 0 & 0 \\ 0 & 0 & 1 & 0 \\ 0 & 0 & 0 & -1 \end{pmatrix}. \quad (\text{II.95})$$

Later, this gate was experimentally realized using a transmon-resonator system in the dispersive regime. It has also been implemented to run the Grover and Deutsch-Josza algorithms and create Bell states[16]. Furthermore, the combination of more than one c-Phase gate with single rotation gates has been reported to generate maximally entangled GHZ states in experimental studies with transmon qubit devices in Refs.[48, 50].

II.5 Chapter summary

In this chapter, we have reviewed some superconducting qubits such as charge and transmon qubits and discussed the coupling of transmon-type to a microwave resonator in circuit QED. We have also introduced the difference between transmon and charge regimes and some of the basic regimes of the QED circuit by making an association with its similar which is the well-known cavity QED. We have associated the quantum information processing protocols of chapter I with the transmon-cavity system discussed here by realizing the X -, Y -, and Z -rotations gates for one qubit. we have also seen some two-qubit operations, such as the c-Phase and \sqrt{iSWAP} gates, which are arisen from two-qubit interaction Hamiltonian. The remaining chapters of the thesis will detail our proposal for the realization of the X -rotation gate for two- and multi-qubit and its implementation in the Grover search algorithm, as well as the entangling gates with the transmon-cavity device, using a one-step approach.

CHAPITRE III

REALIZING TWO- AND MULTI-QUBIT QUANTUM GATES IN OPEN QUANTUM SYSTEMS VIA QED CIRCUIT FOR SUPERCONDUCTING QUBITS

The realization of two- and multi-qubit quantum gates or algorithms typically decomposes into single and two-qubit gates that have a very important practical role in quantum information processing. Such an approach has been experimentally demonstrated using superconducting devices[16, 26, 48, 49, 50, 52, 64]. However, these approaches become difficult to build if only basic gates are available because the number of single- and two-qubit operations drastically increases as the number of qubits increases[83, 115, 116]. Therefore, the direct implementation of quantum gates and algorithms acting on more than two qubits is useful and efficient method, because it requires a shorter execution time and can be executed with high fidelity than the equivalent ones. In this framework, a one-step operation for generating a GHZ-entangled state and realizing multi-qubit gates have been previously proposed in systems of superconducting qubits in Refs.[92, 93, 94, 95, 96, 97, 98, 99, 100, 101, 102, 103].

In this chapter, we will suggest an efficient and fast method to realize the X -rotation and entangling gate for two and several qubits using a one-step approach based on the transmon-resonator system. Such a system comprises transmon-type superconducting qubits capacitively coupled to a resonator, driven by a strong microwave field. This chapter will begin with a discussion of our transmon -resonator device and its physical description. Next, we suggest a fast scheme to achieve the X -rotation gate for two- and multi-qubit requiring only one-step operation. Next, we will realize the single-shot entangling gate for two and several qubits by exploiting the amount of existing entanglement between the transmon-type superconducting qubits. Finally, we end this

chapter with a conclusion.

III.1 Multi-qubit device description

III.1.1 Multi-qubit device

We here describe our quantum device used during the two last chapters of this thesis, it is comprised of transmon-type superconducting qubits capacitively coupled with a superconducting resonator with the assistance of a classical driving field. Moreover, we consider the three-qubit device, where three transmon-type superconducting qubits (Q_j for $j = 1, 2, 3$) are capacitively coupled to a microwave transmission line resonator, as shown in figure(III.1). Similar architectures have been studied in previous references [64, 117, 118]. As shown in figure(III.1), the resonator is driven by an external classical field with the frequency ω_d and it can be described by the Hamiltonian[118]

$$H_d = \varepsilon(t) \left(a^+ e^{-i\omega_d t} + a e^{i\omega_d t} \right), \quad (\text{III.1})$$

where $\varepsilon(t)$ is the slowly-varying amplitude of the microwave field.

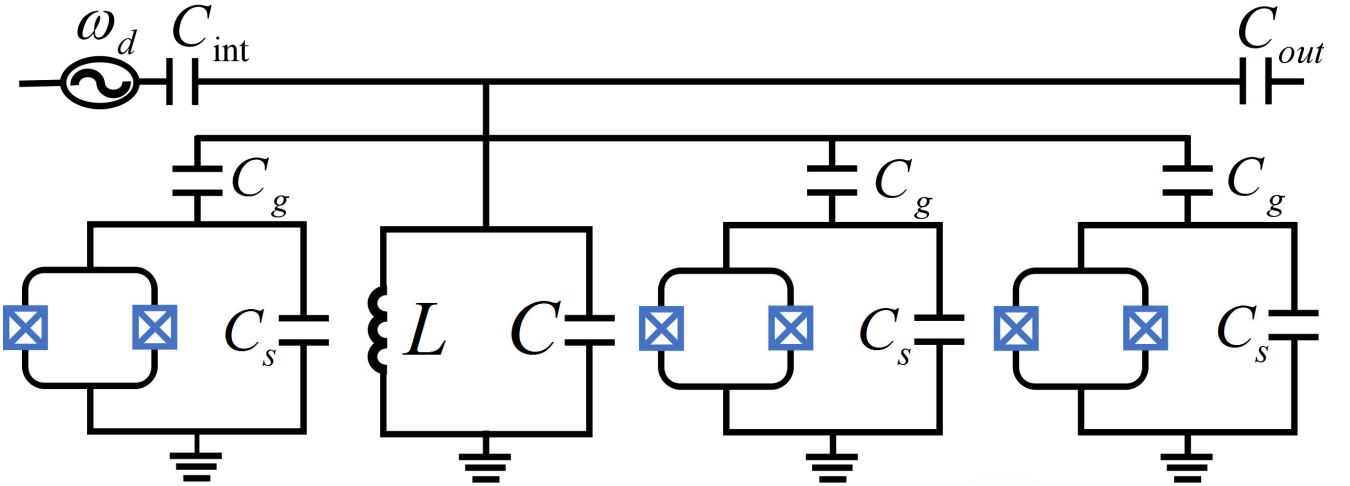


FIGURE III.1 – Electrical circuit diagram of a three-qubit device[119].

The schematic diagram in figure(III.1) consists of three transmon qubits with the transition frequency between the two adjacent states, this frequency is given by $\omega_q = \sqrt{8E_J E_c}$ (which is typically between 3 and 10 GHz) and can be controlled through the flux dependent of Josephson energy $E_J = E_{J,\max} \cos(\pi\Phi_e/\Phi_0)$ by means of an external magnetic flux Φ_e , where $\Phi_0 = h/2e$ is the magnetic flux quantum[43]. These qubits are coupled to the superconducting resonator via

identical capacitors C_g of frequency $\omega_r = 1/\sqrt{LC}$ (typically lies between 5 and 10 GHz) which is connected to input and output with capacitors C_{int} and C_{out} , respectively, and a strong microwave field is applied to the input wire of the resonator.

Important remark : During the two last chapters of this thesis and without losing any generality, we consider the transmon-type superconducting qubits identical. This is valid for tunable transmon when its frequency can be tuned using magnetic flux. In this case, we will drop off the subscript j for the system parameters.

III.1.2 Hamiltonian description and the corresponding time evolution operator

Jaynes-Cummings model and Beyond

The coupled system depicted in figure (III.1) can be described by the following Hamiltonian

$$\tilde{H} = H_{JC} + H_D, \quad (\text{III.2})$$

where H_D in equation (III.1), while H_{JC} denotes the Jaynes-Cummings Hamiltonian and is given by

$$H_{JC} = \omega_r a^\dagger a + \frac{1}{2} \sum_{j=1}^3 \omega_{q,j} \sigma_z^j + \sum_{j=1}^3 g_j (a^\dagger \sigma_-^j + a \sigma_+^j), \quad (\text{III.3})$$

where a^\dagger and (a) are the creation and annihilation operator of the resonator, respectively. $\omega_{q,j}$ are the frequencies of transmon-type superconducting qubits and g_j denotes the qubit-resonator coupling strengths, and the j subscript is used to distinguish the different elements and their parameters. The operators $\sigma_z^j = |1_j\rangle\langle 1_j| - |0_j\rangle\langle 0_j|$, $\sigma_+^j = |1_j\rangle\langle 0_j|$ and $\sigma_-^j = |0_j\rangle\langle 1_j|$ are Pauli matrices.

For a large amplitude driving field $\varepsilon(t)$, quantum fluctuations in the drive can be neglected as well as being modeled as a classical field. In this case, we can displace the resonator field operators by using the time-dependent displacement operator which will be more convenient

$$D(\alpha) = \exp(\alpha a^\dagger - \alpha^* a). \quad (\text{III.4})$$

Under this transformation, the operator a becomes $a + \alpha$ where α is a complex number that

denotes the classical part of the field. Then, the displaced Hamiltonian reads[118]

$$\begin{aligned} H &= D^+(\alpha) \tilde{H} D(\alpha) - i D^+(\alpha) \dot{D}(\alpha) \\ &= \omega_r a^+ a + \frac{1}{2} \sum_{j=1}^3 \omega_q \sigma_z^j + \sum_{j=1}^3 g \left(a^+ \sigma_-^j + a \sigma_+^j \right) - \sum_{j=1}^3 g \left(\alpha^* \sigma_-^j + \alpha \sigma_+^j \right), \end{aligned} \quad (\text{III.5})$$

where we chose $\alpha(t)$ to satisfy

$$\dot{\alpha} = -i\omega_r \alpha - i\varepsilon(t) e^{-i\omega_d t}. \quad (\text{III.6})$$

The reason for this α choice is to eliminate the direct drive on the resonator equation(III.2). When the amplitude ε is independent of time, we easily find $\alpha = -(\varepsilon/\Delta_r) e^{-i\omega_d t}$ with $\Delta_r = \omega_r - \omega_d$, and equation (III.5) becomes[93, 121, 122, 123]

$$H = H_1 + H_2 + H_3, \quad (\text{III.7})$$

where

$$H_1 = \omega_r a^+ a + \frac{1}{2} \sum_{j=1}^3 \omega_q \sigma_z^j, \quad (\text{III.8})$$

$$H_2 = \sum_{j=1}^3 g \left(a^+ \sigma_-^j + a \sigma_+^j \right), \quad (\text{III.9})$$

$$H_3 = \sum_{j=1}^3 \Omega_R \left(\sigma_-^j e^{i\omega_d t} + \sigma_+^j e^{-i\omega_d t} \right), \quad (\text{III.10})$$

where H_1 is the free Hamiltonian of the transmon systems and the resonator, H_2 is the interaction Hamiltonian between the transmon systems and the resonator and H_3 is the interaction Hamiltonian between the transmon systems and the microwave field(with $\Omega_R = \varepsilon g/\Delta_r$ is the Rabi frequency).

We choose the frequencies ω_q and ω_d to satisfy $\omega_d = \omega_q$ we get $\Delta_r = \omega_r - \omega_q$. Then the interaction Hamiltonian in the interaction picture with respect to H_1 ($H_I = e^{iH_1 t} H e^{-iH_1 t}$), is given by

$$H_I = H_0 + H_i, \quad (\text{III.11})$$

where

$$H_0 = 2\Omega_R S_x, \quad \text{with} \quad S_x = \frac{1}{2} \sum_{j=1}^3 (\sigma_-^j + \sigma_+^j), \quad (\text{III.12})$$

and

$$H_i = g \sum_{j=1}^3 (a^+ \sigma_-^j e^{i\Delta_r t} + a \sigma_+^j e^{-i\Delta_r t}). \quad (\text{III.13})$$

In the interaction picture with respect to H_0 , the Hamiltonian H_i yields ($H'_i = e^{iH_0 t} H_i e^{-iH_0 t}$)

$$\begin{aligned} H'_i &= g \left\{ e^{-i\Delta_r t} a^+ \left[S_x + \frac{1}{2} \sum_{j=1}^3 (\sigma_z^j - \sigma_-^j + \sigma_+^j) e^{-2i\Omega_R t} - \frac{1}{2} \sum_{j=1}^3 (\sigma_z^j + \sigma_-^j - \sigma_+^j) e^{2i\Omega_R t} \right] \right\} \\ &+ \text{H.c.} \end{aligned} \quad (\text{III.14})$$

In the strong driving regime when $2\Omega_R \gg g$ and $2\Omega_R \gg \Delta_r$, we can neglect from equation (III.14) the fast-oscillating terms with high frequencies. Then the Hamiltonian H can be reduced to [93, 121]

$$H'_i = g (a^+ e^{-i\Delta_r t} + a e^{i\Delta_r t}) S_x. \quad (\text{III.15})$$

The corresponding evolution operator to the Hamiltonian (III.15) can be written in the form [93, 124]

$$U'_i(t) = e^{-iA(t)S_x^2} e^{-iB(t)S_x a} e^{-iB^*(t)S_x a^+}, \quad (\text{III.16})$$

where

$$A(t) = \frac{g^2 [t + (e^{-i\Delta_r t} - 1)/i\Delta_r]}{\Delta_r}, \quad \text{and} \quad B(t) = \frac{g(e^{i\Delta_r t} - 1)}{i\Delta_r}. \quad (\text{III.17})$$

In the following, if we choose the evolution time, t , to satisfy $\Delta_r t = 2\pi$, we can obtain $B(t) = 0$ and $A(t) = g^2 t / \Delta_r$. The corresponding evolution operator to the whole system becomes independent of the resonator mode and is given by

$$U_I(t) = e^{-iH_0 t} U'_i(t) = e^{-2i\Omega_R S_x t} e^{-2i\lambda S_x^2 t}, \quad (\text{III.18})$$

where $\lambda = g^2 / 2\Delta_r$ is the effective qubit-qubit coupling strength [122]. We note that the evolution operator described by Eq. (III.18) does not include the photon operator a or a^+ of the resonator

mode. Therefore, the cavity can be initially in an arbitrary state (e.g., in a vacuum state, a coherent state, a Fock state, or even a thermal state).

Important remark : We note that the deriving evolution operator of our transmon-resonator does not necessarily need the condition $\Delta_r \gg g$, indicating that the schemes existing in the two last chapters do not necessarily work in the dispersive regime. In addition, the preceding schemes work in the dispersive regime, leading to a rather slow energy exchange between transmon systems. Therefore, our schemes do not limit any of the dispersive approximation conditions being valid.

III.2 Open system dynamics

An open quantum system is a quantum system that is coupled to its environment. Describing the evolution of the open quantum system dynamics using a Schrödinger equation approach alone will make it impossible to achieve. In this subsection, we, therefore, employ the master equation, which is a more powerful approach that can describe the full dynamics of open quantum systems.

III.2.1 Master equation

We start with the general formalism of the master equation and then apply it to the case of our transmon-resonator system discussed above. In general, the time evolution is a mixed state that can be described by the density matrix ρ , by taking into account the system dissipation. This description is governed by the master equation, which can be generally written in the Lindblad form as (more details on the master equation derivation can be found in Red.[\[125\]](#))

$$\frac{d\rho}{dt} = \frac{-i}{\hbar} [H_{sys}, \rho] + \mathcal{L}[\Lambda] \rho, \quad (\text{III.19})$$

where $\mathcal{L}[\Lambda] \rho = \frac{1}{2} \sum_i \left(L_i \rho L_i^\dagger - L_i^\dagger L_i \rho - \rho L_i^\dagger L_i \right)$ and $L_i = \sqrt{\gamma_n} \Lambda_i$ are collapse operators, with Λ_i the Lindblad operators, describing the non-unitary dynamics under a Hamiltonian of the system H_{sys} due to the coupling of the system to its environment, and γ_n are the corresponding rates.

As an example, we consider the transmon-resonator system consisting of the transmon qubits coupled to a resonator with the assistance of a classical field. Coupling with additional uncontrollable degrees of freedom leads to dissipation in the system. In the Born-Markov approximation, this dissipation can be characterized by the resonator dissipation which is described by a photon leakage rate $\kappa \simeq \omega_r/Q$, the relaxation rate $\gamma_{1,j} = 1/T_1$, and the dephasing rate $\gamma_{\varphi,j} = 1/T_1 - 1/2T_2$

for each transmon qubit. In these expressions, Q is the quality factor of the resonator, T_1 is the decoherence time, and T_2 is the dephasing time. In the presence of these processes, the master equation in Eq. (III.19) can be rewritten as

$$\frac{d\rho}{dt} = -\frac{i}{\hbar} [H', \rho] + \kappa \mathcal{L}[a] + \sum_j \gamma_{1,j} \mathcal{L}[\sigma_-^j] + \sum_j \gamma_{\varphi,j} \mathcal{L}[\sigma_z^j], \quad (\text{III.20})$$

where H' is the system Hamiltonian, which can be either H in Eq. (III.7) or H_I in Eq. (III.11). While $\mathcal{L}[\Lambda] = \Lambda \rho \Lambda^\dagger - \Lambda^\dagger \Lambda \rho / 2 - \rho \Lambda^\dagger \Lambda / 2$ with $\Lambda = a, \sigma_-^j$, or σ_z^j .

III.2.2 Fidelity under master equation

In order to characterize the performance of the quantum states or operations, it is necessary to compute the fidelity. The fidelity presents the measurement of the distance between two mixed states ρ and σ , and it is given by

$$F = \left(\text{Tr} \left[\sqrt{\sqrt{\sigma} \rho \sqrt{\sigma}} \right] \right)^2. \quad (\text{III.21})$$

In the case where one of the two states chosen pure, e.g. $\sigma = |\psi\rangle \langle \psi|$, equation (III.21) can be readily simplified to

$$\begin{aligned} F &= \text{Tr} [\rho |\psi\rangle \langle \psi|] \\ &= \langle \psi | \rho | \psi \rangle, \end{aligned} \quad (\text{III.22})$$

where ψ is the pure output state expected from the ideal unitary operation and ρ is the density operator of the system at the end of the quantum operation, obtained by numerically solving the master equation (III.20), using the QuTiP software [126, 127], which is an open-source software for simulating the open quantum systems dynamics.

III.3 Realizing X -rotation gate for multi-qubit in the open quantum systems

The X -rotation gate plays a similar role to Hadamard gate for creating quantum superposition and it is an important tool in quantum computation[1]. Therefore, the direct realization of a multi-qubit X -rotation gate can be expected to provide fast and practical ways in quantum computation in comparison with the ones provided by single qubit X -rotation gates. In addition, its realization plays a critical role in Grover's search algorithm as we will show in the next chapter. Here, we present a scheme to realize the X -rotation gate for two and three qubits with an angle $-\pi/2$ using

only a single-step operation based on the evolution operation (III.18) in the open quantum systems.

III.3.1 X -rotation gate for two transmon systems

III.3.1.1 Two-qubit X -rotation gate generation

In the two-qubit basis $\{|00\rangle, |01\rangle, |10\rangle, |11\rangle\}$, we define the two-qubit X -rotation gate with an angle $-\pi/2$

$$R_x^{\otimes 2}\left(-\frac{\pi}{2}\right) = \begin{pmatrix} 1 & i & i & -1 \\ i & 1 & -1 & i \\ i & -1 & 1 & i \\ -1 & i & i & 1 \end{pmatrix}, \quad (\text{III.23})$$

where single qubit gate $R_x^{\otimes 2}(-\pi/2)$ transform states $|0\rangle$ and $|1\rangle$ to the superposition states $(1/\sqrt{2})(|0\rangle + i|1\rangle)$ and $(i/\sqrt{2})(|0\rangle - i|1\rangle)$, respectively.

The evolution operator $U_I(t)$ of the two transmon system (Eq. (III.18)) can be expressed on the same basis as [121, 128]

$$\begin{aligned} U_I(t) &= e^{-2i\Omega_R S_x t} e^{-2i\lambda S_x^2 t} \\ &= \begin{pmatrix} \frac{1}{2} + \frac{1}{2} \cos(2\Omega_R t) e^{-2i\lambda t} & -\frac{i}{2} \sin(2\Omega_R t) e^{-2i\lambda t} & -\frac{i}{2} \sin(2\Omega_R t) e^{-2i\lambda t} \\ -\frac{i}{2} \sin(2\Omega_R t) e^{-2i\lambda t} & \frac{1}{2} + \frac{1}{2} \cos(2\Omega_R t) e^{-2i\lambda t} & -\frac{1}{2} + \frac{1}{2} \cos(2\Omega_R t) e^{-2i\lambda t} \\ -\frac{i}{2} \sin(2\Omega_R t) e^{-2i\lambda t} & -\frac{1}{2} + \frac{1}{2} \cos(2\Omega_R t) e^{-2i\lambda t} & \frac{1}{2} + \frac{1}{2} \cos(2\Omega_R t) e^{-2i\lambda t} \\ -\frac{1}{2} + \frac{1}{2} \cos(2\Omega_R t) e^{-2i\lambda t} & -\frac{i}{2} \sin(2\Omega_R t) e^{-2i\lambda t} & -\frac{i}{2} \sin(2\Omega_R t) e^{-2i\lambda t} \\ -\frac{1}{2} + \frac{1}{2} \cos(2\Omega_R t) e^{-2i\lambda t} & -\frac{i}{2} \sin(2\Omega_R t) e^{-2i\lambda t} & -\frac{i}{2} \sin(2\Omega_R t) e^{-2i\lambda t} \\ -\frac{i}{2} \sin(2\Omega_R t) e^{-2i\lambda t} & -\frac{i}{2} \sin(2\Omega_R t) e^{-2i\lambda t} & \frac{1}{2} + \frac{1}{2} \cos(2\Omega_R t) e^{-2i\lambda t} \end{pmatrix}, \end{aligned} \quad (\text{III.24})$$

where $S_x = (1/2) \sum_{j=1}^2 (\sigma_+^j + \sigma_-^j)$. In the situation where $2\lambda t = \pi$ and $2\Omega_R t = (2n+1)\pi/2$ (n is an interger), i.e., the operation time can be chosen to be $t = \pi/2\lambda$ and the Rabi frequency satisfying

$\Omega_R/\lambda = (2n + 1)/2$. Therefore, the above evolution operator (Eq. (III.22)) leads to the two-qubit X -rotation gate with the angle $-\pi/2$, writes[128]

$$U_I(t) = \begin{pmatrix} 1 & i & i & -1 \\ i & 1 & -1 & i \\ i & -1 & 1 & i \\ i & i & i & 1 \end{pmatrix} = R_x^{\otimes 2} \left(-\frac{\pi}{2} \right). \quad (\text{III.25})$$

This result depicts that the coupling between the two transmon qubits mediated by a resonator with the assistance of a strong classical field can easily achieve the two-qubit X -rotation gate. This gate is efficient as it can replace the need for two individual X -rotation gates applied to two separate qubits. Combining this gate with other two-qubit gates is crucial in forming a set of universal gates for quantum computation [1].

III.3.1.2 Fidelity and discussion

In order to examine the robustness with respect to the dissipation of our transmon-resonator system for realizing the two-qubit X -rotation gate (Eq. (III.25)), it is necessary to estimate the fidelity. The gate fidelity is given in equation (III.22), where $|\psi\rangle$ is the ideal output state without any dissipation after applying a two-qubit X -rotation gate performed on the transmon system initially in the state $|00\rangle$ and the resonator mode initially in the state $|0\rangle_r$. It is given by

$$|\psi\rangle = \frac{1}{2} (|00\rangle + i|01\rangle + i|10\rangle - |11\rangle), \quad (\text{III.26})$$

while ρ is the final density operator of the system at the end of the two-qubit X -rotation gate, obtained by solving the master equation (III.20) numerically for $j=1,2$, where $\mathcal{L}[\Lambda] = \Lambda\rho\Lambda^\dagger - \Lambda^\dagger\Lambda\rho/2 - \rho\Lambda^\dagger\Lambda/2$ with $\Lambda = a$, σ_-^1 , σ_-^2 , σ_z^1 , or σ_z^2 . In addition, we assume $\gamma_{1,1} = \gamma_{1,2} = \gamma_1$ and $\gamma_{\varphi,1} = \gamma_{\varphi,2} = \gamma_\varphi$ for simplicity.

We have numerically simulated the fidelity of the two-qubit X -rotation gate in equation (III.25) under both Hamiltonians (III.7) and (III.11) versus κ and T as depicted in figure (III.2), where the resonator mode is in the vacuum state. The fidelities of the two-qubit X -rotation gate corresponding to both Hamiltonians (III.7) and (III.11) are the almost same. From figure (III.2a), one can see that the fidelity is achieved at a high ~ 0.998 even though the resonator decay κ reaching to large values, indicating that the gate fidelity is insensitive to the resonator decay. For the numerical simulations of this figure, we have chosen the system parameters as $\omega_r/2\pi = 6.4$

GHz and $\omega_q/2\pi = 4.8\text{GHz}$, leading to $\Delta_r/2\pi = 0.896\text{GHz}$. In addition, we choose $g/2\pi = 60\text{ MHz}$ and $\Omega_R/2\pi = 200\text{MHz}$, which are readily available as $g/2\pi = 10 - 200\text{ MHz}$ and $\Omega_R/2\pi = 300\text{ MHz}$ which have been reported in references[48, 64, 117, 118, 120, 129]. We note that these values satisfy the conditions for realizing the two-qubit X -rotation gate chosen above.

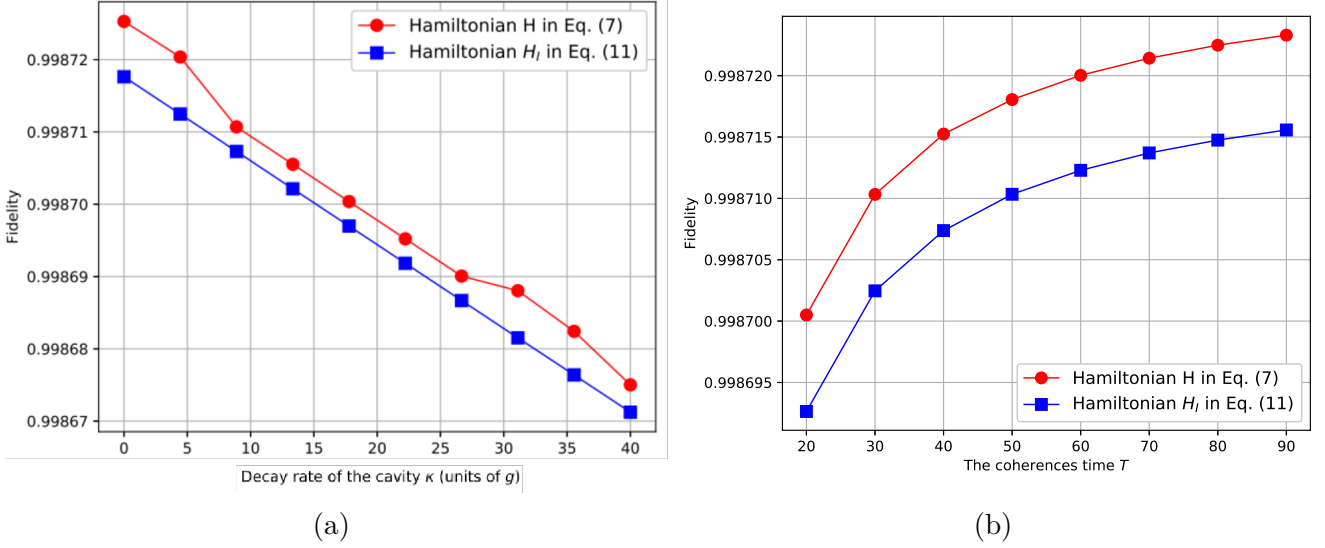


FIGURE III.2 – (Color online) (a) Fidelity of the two-qubit X -rotation gate as a function of the decay rate of resonator κ (a) and as a function of the coherence time T (b). The blue solid line means that our calculation was performed by using the Hamiltonian (III.7) for $j=1,2$, while the calculation referred to by the solid line was performed using the Hamiltonian (III.11) for $j=1,2$. The system parameters used in the numerical simulation are mentioned in the text.

In addition, the measuring of the decoherence time T_1 and dephasing time T_2 for transmon devices between 20 and 95 μs have been reported in references[45, 130, 131]. Therefore, we here choose $T_1 = 95\mu\text{s}$ and $T_2 = 70\mu\text{s}$, leading to a relaxation rate $\gamma_1/2\pi = 1.68\text{kHz}$ and dephasing rate $\gamma_\varphi/2\pi = 1.68\text{kHz}$. Furthermore, we have chosen the operation time based on the gate conditions above for $n = 0$ to be $t = \pi/(4\Omega_R) \sim 0.62\text{ns}$ (where $\lambda = 3\Omega_R$), which is much shorter than the coherence time of the transmon system and the cavity decay time. While the effect of the coherences time ~ 0.998695 on the performance of the two-qubit X -rotation gate has been explored in figure (III.2b). As shown in Fig. (III.2b), the effect of the decoherence becomes less dominant, and the fidelity of a quantum gate has achieved a high fidelity (even for a small value of the coherences time, whereas, it is clear that the gate fidelity slowly increases as the coherences time increases and it reaches to 0.99872 high value. Here, we have chosen $\kappa = 2.5\text{MHz}$ and the other parameters are the same as in panel (a).

III.3.2 X -rotation gate for three transmon systems

III.3.2.1 Three-qubit X -rotation gate generation

In the three-qubit basis $\{|000\rangle, |001\rangle, |010\rangle, |011\rangle, |100\rangle, |101\rangle, |110\rangle, |111\rangle\}$, we define the X -rotation gate for three qubits with an angle $-\pi/2$

$$\begin{aligned}
 W_3 &= R_x^{\otimes 3} \left(-\frac{\pi}{2} \right) \sigma_x^{\otimes 3} \\
 &= \frac{1}{2\sqrt{2}} \begin{pmatrix} -i & -1 & -1 & i & -1 & i & i & 1 \\ -1 & -i & i & -1 & i & -1 & 1 & i \\ -1 & i & -i & -1 & i & 1 & -1 & i \\ i & -1 & -1 & -i & 1 & i & i & -1 \\ -1 & i & i & 1 & -i & -1 & -1 & i \\ i & -1 & 1 & i & -1 & -i & i & -1 \\ i & 1 & -1 & i & -1 & i & -i & -1 \\ 1 & i & i & -1 & i & -1 & -1 & -i \end{pmatrix}, \quad (\text{III.27})
 \end{aligned}$$

where σ_x denotes the NOT gate operation for single qubit, while $\sigma_x^{\otimes 3} = \sigma_x \otimes \sigma_x \otimes \sigma_x$. The evolution operator of equation (III.18) can be expressed in the same basis as [119]

$$\begin{aligned}
 U_I(t) &= e^{-ibhS_x} e^{-ibS_x^2} \\
 &= \begin{pmatrix} A' & C' & C' & D' & C' & D' & D' & B' \\ C' & A' & D' & C' & D' & C' & B' & D' \\ C' & D' & A' & C' & D' & B' & C' & D' \\ D' & C' & C' & A' & B' & D' & D' & C' \\ C' & D' & D' & B' & A' & C' & C' & D' \\ D' & C' & B' & D' & C' & A' & D' & C' \\ D' & B' & C' & D' & C' & D' & A' & C' \\ B' & D' & D' & C' & D' & C' & C' & A' \end{pmatrix}, \quad (\text{III.28})
 \end{aligned}$$

where A' , B' , C' and D' are the elements of the evolution operator matrix $U_I(t)$ (Eq. (III.27)) given by

$$A' = \frac{1}{4}e^{-i\frac{9b}{4}} \left(\cos\left(\frac{3bh}{2}\right) + 3\cos\left(\frac{bh}{2}\right)e^{2ib} \right), \quad (\text{III.29})$$

$$B' = \frac{-i}{4}e^{-i\frac{9b}{4}} \left(\sin\left(\frac{3bh}{2}\right) - 3\sin\left(\frac{bh}{2}\right)e^{2ib} \right), \quad (\text{III.30})$$

$$C' = \frac{-i}{4}e^{-i\frac{9b}{4}} \left(\sin\left(\frac{3bh}{2}\right) + \sin\left(\frac{bh}{2}\right)e^{2ib} \right), \quad (\text{III.31})$$

$$D' = \frac{1}{4}e^{-i\frac{9b}{4}} \left(\cos\left(\frac{3bh}{2}\right) - \cos\left(\frac{bh}{2}\right)e^{2ib} \right), \quad (\text{III.32})$$

with $b = 2\lambda t$ and $h = \Omega_R/\lambda$. Taking the condition chosen above $\Delta_r t = 2\pi$, and setting $bh = \pi/2$ and $b = 8(m+1)\pi$ (m is an integer), we can choose the interaction time $t = t_R = \pi/4\Omega_R$ and $\Delta_r/\Omega_R = 8$. Then the evolution operator (Eq. III.28) leads to

$$U_I(t_R) = \exp(i\pi/2) W_3, \quad (\text{III.33})$$

where $\exp(i\pi/2)$ is an overall phase and W_3 is the single three-qubit X -rotation gate defined in equation (III.27). This gate together with single two-qubit rotation gates is very important to form a set of universal gates for quantum computation[1].

III.3.2.2 Fidelity and discussion

In order to evaluate the validity of our proposal, we calculate the fidelity of the three-qubit X -rotation gate in Eq. (III.33). It is given in equation (III.22), where $|\psi\rangle$ is the output state without dissipation system after a joint three-qubit X -rotation operation is performed on the initial state $|000\rangle|0\rangle_r$ and it is given by

$$\begin{aligned} |\psi\rangle &= \left(\frac{1}{2\sqrt{2}} \right) (-i|0_1 0_2 0_3\rangle - |0_1 0_2 1_3\rangle - |0_1 1_2 0_3\rangle + i|0_1 1_2 1_3\rangle - |1_1 0_2 0_3\rangle \\ &+ i|1_1 0_2 1_3\rangle + i|1_1 1_2 0_3\rangle + |1_1 1_2 1_3\rangle) \otimes |n\rangle_r, \end{aligned} \quad (\text{III.34})$$

while ρ is the final density of the whole system obtained by solving the master equation (III.20) (for $j = 1, 2, 3$) using the numerical simulation, where $\Lambda = a, \sigma_-^1, \sigma_-^2, \sigma_-^3, \sigma_z^1, \sigma_z^2$, or σ_z^3 and for simplicity, we assume $\gamma_{1,1} = \gamma_{1,2} = \gamma_{1,3} = \gamma_1$ and $\gamma_{\varphi,1} = \gamma_{\varphi,2} = \gamma_{\varphi,3} = \gamma_\varphi$.

We numerically calculated the fidelity of the single three-qubit X -rotation gate in equation (III.33) for different initial states of the transmon system. Due to the similarity, we only demonstrate the fidelity corresponding to the initial state $|000\rangle$ in figure (III.3) as an example.

Figure (III.3a) shows the fidelity versus the cavity decay rate κ for the operation gate defined in Eq. (III.33), when the resonator is initially in the ground state and it will remain in this state throughout the procedure. Our simulations show that the fidelities corresponding to Hamiltonians (III.7) and (III.11) are almost the same, and the gate fidelity decreases while increasing the cavity decay rate κ as expected.

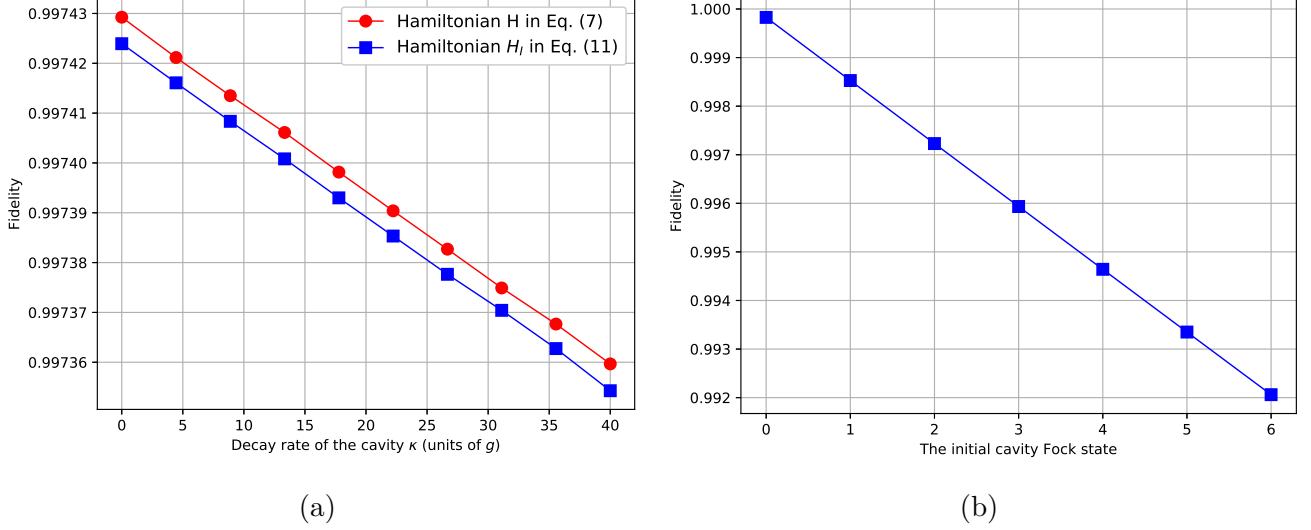


FIGURE III.3 – (Color online) (a) Fidelity of the three-qubit X -rotation gate for different values of the cavity decay rate κ (a) and initial cavity Fock states $|n\rangle$ (b). The blue solid line means that our calculation was performed by using the Hamiltonian (III.7) for $j=1,2,3$, while the calculation referred by the solid line was performed using the Hamiltonian (III.11) for $j=1,2,3$. The system parameters used in the numerical simulation are the same as a figure (III.2) while the others are mentioned in the text.

However, one can see the gate operational fidelity nearly keeps 0.997 for a large range of cavity decay. This result means that cavity decay does not influence the gate fidelity of our proposal. Additionally, the fidelity of this scheme can be further increased as the qubit–resonator coupling strength g is increased. This improvement will be clearly shown in figure (III.3b) for $n = 0$ compared with figure (III.3a). The system parameters used here are the same of the figure (III.2). For the resonator frequency chosen in the previous subsection and for the decay rate $\kappa/2\pi = 0.5$ MHz used in the numerical simulation, the required quality factor for the resonator is $Q \sim 1.28 \times 10^4$. The cavity quality factor here is achievable in experiments because the transmission line resonator (TLR) with a quality factor $Q \sim 10^3$ has been demonstrated in experiments[48, 120].

Furthermore, the fidelity of an operation gate for different initial cavity Fock state $|n\rangle$ is plotted in Fig. (III.3b), it is clear that the fidelity slightly decreases with the increase of the photon number. In contrast, we find that the fidelity can still be over 0.99 even for $n = 6$, which means the cavity state almost does not influence the gate fidelity. Finally, our presented analysis

is given throughout the two subsections implying that high-fidelity implementation of a two- and multi-qubit X -rotation gates are feasible with the present circuit QED technology.

III.4 Single-shot entangling gate in the open quantum systems

Due to its high fidelity, a single-shot entangling gate plays a key role in quantum information processing. This operation gate quickly creates a maximally entangled state and forms a universal entrance set for quantum computing. Currently, the preparation and demonstration of multi-qubit entangling gates are achieved based on the decomposition of single- and two-qubit operations, yielding lower fidelity and requiring longer execution time. Here, we propose the two- and three-qubit entangling gates to generate a maximally entangled state based on our transmon-resonator system requiring only a one-step operation, as well as we numerically investigate the system dynamics of these operation gates under realistic assumptions about the system parameters.

III.4.1 Entangling gate for two transmon systems

III.4.1.1 Two-qubit entangling gate generation

In the following, if we choose the Rabi frequency satisfying $\Omega_R t = n\pi$ in the evolution operator of two transmon systems $U_I(t)$ (Eq.(III.24)), we have the two-qubit entangling gate

$$U_I(t) = e^{-i\lambda t} \begin{pmatrix} \cos(\lambda t) & 0 & 0 & -i \sin(\lambda t) \\ 0 & \cos(\lambda t) & -i \sin(\lambda t) & 0 \\ 0 & -i \sin(\lambda t) & \cos(\lambda t) & 0 \\ -i \sin(\lambda t) & 0 & 0 & \cos(\lambda t) \end{pmatrix}, \quad (\text{III.35})$$

where the factor $e^{-i\lambda t}$ is an overall phase. Remarkably, where the transmon systems are initially in the state $|00\rangle$ and the operation time $t = \pi/4\lambda$, the gate described by equation (III.35) can fastly generate a two-qubit maximally entangled state $U_I(\pi/4\lambda) |00\rangle = (1/\sqrt{2}) (|00\rangle - i |11\rangle)$, which was realized experimentally with a superconducting transmon device using sequences of single- and two-qubit gates[16, 62].

III.4.1.2 Two-qubit entangling gate characterization

Time evolution

The result which is shown in figure (III.4) presents the time evolution of the state occupation probabilities P_{ij} as a function of the interaction time corresponding to applying a single entangling gate, assuming the transmon systems initially prepared in state $|00\rangle$ and the resonator in the vacuum state (where P_{ij} are the probabilities of finding $|ij\rangle$ with $ij = 00; 01; 10; \text{ or } 11$). These results were obtained by numerically solving the Lindblad master equation in equation (III.20) (for $j=1,2$), we here assume that $T_c = T_1 = T_2$, which is valid for tunable transmons[88].

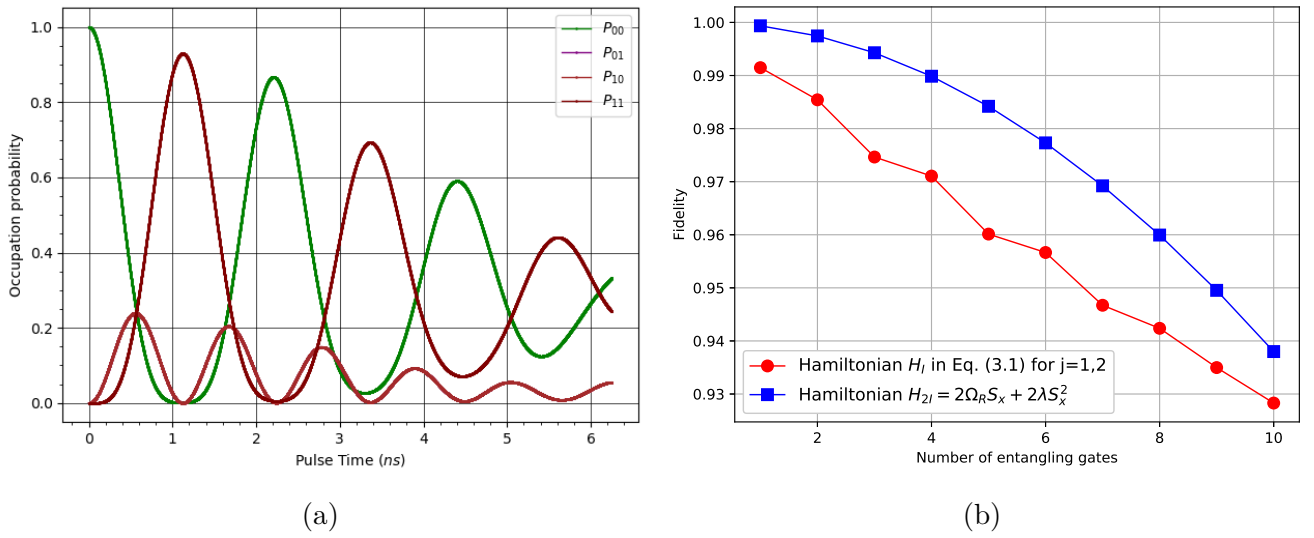


FIGURE III.4 – (Color online) Simulated measurements of the single-shot entangling gate (Eq.III.35) (a) The occupation probabilities versus the interaction time. The system parameters used in the numerical simulation are $g/2\pi = 40$ MHz, $2\Omega_R = 9g$, $T_c = 20\mu s$, and $\kappa/2\pi = 1.5$ MHz. (b) Fidelity versus the number of the two-qubit entangling gates with environment decoherence under the Hamiltonian in equation (III.11) and without environment decoherence under the following Hamiltonian $H_{2I} = 2\Omega_R S_x + 2\lambda S_x^2$. The data parameters used are the same as in panel (b).

As shown in Fig. (III.4b), the swap oscillation between $|00\rangle$ and $|11\rangle$ is nearly perfect. However, due to the environmental decoherence of our transmon-resonator system, these oscillations decrease with the increasing operation time. On the other hand, the probabilities P_{00} and P_{11} should approach 50% for an ideal entangled state. Still, in our results, these probabilities are reduced to less than 50% in equal superposition crossing points due to the effects of environmental noise. Comparing the simulated with ideal states using the equation (III.22), we find the fidelities corresponding to applying 10-entangling gates are shown in Fig. (III.4b). It is clear that from this figure the fidelities decrease as the growing number of gates, however, the Hamiltonian in Eq. (III.11) decreases more rapidly caused by the effect of the system decoherence and the resonator

decay. In addition, we note that the fidelity for one run of the entangling gate is 99.15%, which means that our scheme is efficient and faster compared to one of the maximally entangled states created from sequences of single- and two-qubit gates[16, 62].

III.4.2 Entangling gate for three transmon systems

III.4.2.1 Three-qubit entangling gate generation

Following the evolution operator in equation (III.27), in which if setting $\Delta_r t = 2\pi$ and $\Delta_r \approx g$, we can make the interaction time t and Rabi frequency Ω_R satisfy $t = T = 3\pi/4\Omega_R$ and $\Omega_R = 3\lambda$. Leading to the three-qubit entangling gate[119]

$$M(T) = e^{-i\theta} \begin{pmatrix} \tilde{A}' & 0 & 0 & 0 & 0 & 0 & 0 & \tilde{B}' \\ 0 & \tilde{A}' & 0 & 0 & 0 & 0 & \tilde{B}' & 0 \\ 0 & 0 & \tilde{A}' & 0 & 0 & \tilde{B}' & 0 & 0 \\ 0 & 0 & 0 & \tilde{A}' & \tilde{B}' & 0 & 0 & 0 \\ 0 & 0 & 0 & \tilde{B}' & \tilde{A}' & 0 & 0 & 0 \\ 0 & 0 & \tilde{B}' & 0 & 0 & \tilde{A}' & 0 & 0 \\ 0 & \tilde{B}' & 0 & 0 & 0 & 0 & \tilde{A}' & 0 \\ \tilde{B}' & 0 & 0 & 0 & 0 & 0 & 0 & \tilde{A}' \end{pmatrix}, \quad (\text{III.36})$$

where $e^{-i\theta}$ is an overall phase (with $\theta = 27\pi/8$), $\tilde{A}' = \cos(\Omega_R T/3)$ and $\tilde{B}' = -i \sin(\Omega_R T/3)$. It is worth noticing that if the transmon systems are initially prepared in the state $|000\rangle$, the operator $M(T)$ can generate a three-qubit *GHZ*-state $M(3\pi/4\Omega_R)|000\rangle = (e^{i\theta}/\sqrt{2})(|000\rangle - i|111\rangle)$. This maximally entangled state for three transmon qubits was experimentally generated with a superconducting transmon and phase device using one- and two-qubit gates[48].

III.4.2.2 Three-qubit entangling gate characterization

To generate a *GHZ*-state based on three transmon systems when the resonator mode in the state $|0\rangle_r$. We initialize all three transmon systems in their ground state $|000\rangle$, whereas assuming that the resonator remains in the vacuum state throughout the operation[See figure (III.5a)]. This assumption is valid for transmon-resonator systems[52]. We depict in Fig. (III.5b), the time evolution of probabilities P_{ijk} during the *GHZ*-state protocol versus the interaction time corres-

ponding to applying a one-entangling gate (where P_{ijk} are the probabilities to find the state $|ijk\rangle$ with $ijk = 000, 001, 010, 011, 100, 101, 110, \text{ or } 111$). We get these results by solving the Lindblad master equation in equation (III.20) (for $j=1,2,3$) for the transmon-cavity density matrix ρ using numerical simulation, we have assumed here the coherence times to be equal $T_c = T_1 = T_2$.

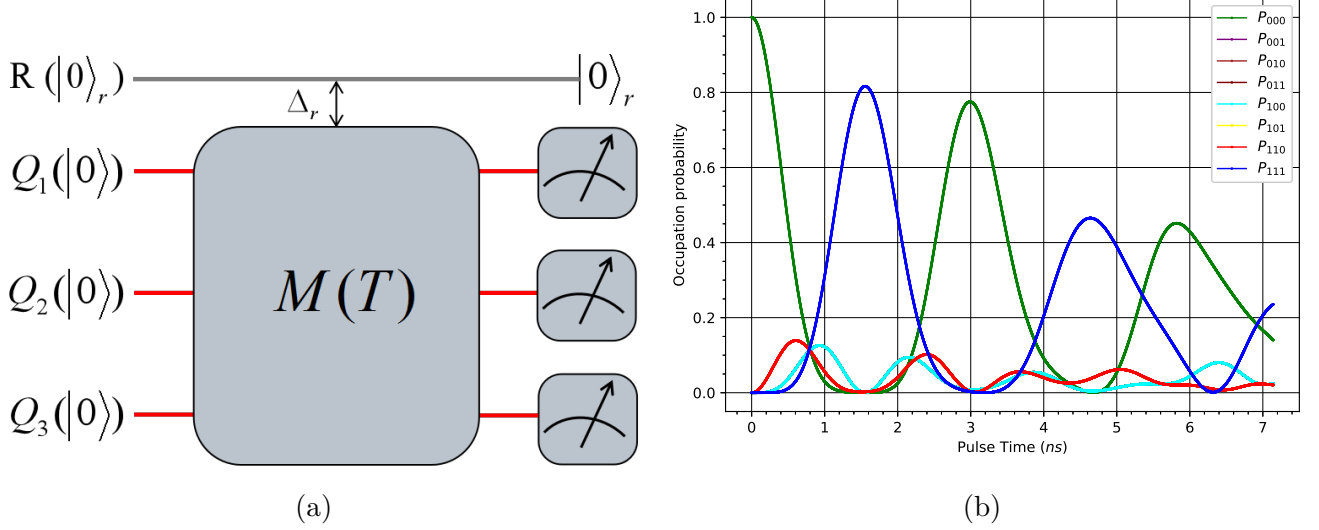


FIGURE III.5 – (Color online) (a) Quantum circuit for generating *GHZ*-state using the single-shot entangling gate (Eq. III.35) (b) The occupation probabilities as a function of the operation time T_m [132]. The system parameters used here are $g/2\pi = 20$ MHz, $2\Omega_R = 9g$, $T_c = 20\mu s$, and $\kappa/2\pi = 1.5$ MHz.

As shown in Fig (III.5b), the swap oscillation between the states $|000\rangle$ and $|111\rangle$ are almost perfect, however, we can see these oscillations decrease with the increase of the pulse time, and also the other occupation probabilities are almost visible owing to the environmental decoherence of both transmon qubits and resonator, which have been taken into account throughout our simulations. In addition, unlike an ideal *GHZ* state in which the probabilities P_{000} and P_{111} can reach 50%, from the figure (III.5b) we see these probabilities are reduced to less than 50% in crossing points due to the environmental noise.

We compare the simulated and ideal states by estimating the gate fidelity of the three-qubit entangling gate using the equation (III.22), where $|\psi\rangle$ is the output state of the system without considering the dissipation and dephasing performed on the transmon system initially prepared in the state $|000\rangle$ and the resonator mode initially in the state $|0\rangle_r$, while ρ is the simulated matrix obtained by numerically solving the equation (III.20). Figure (III.6a) shows the gate fidelity of the entangling gate with and without taking into account the decoherence of the transmon system and the cavity decay under the hamiltonians (III.11) and H_{3I} , respectively. We find the fidelity of both Hamiltonians corresponding to the applied 10-gate by estimating decreases as the number

of the three-qubit entangling gates increases, whereas, due to the environmental noise of both transmon system and resonator decay the fidelity corresponding to Hamiltonian in Eq. (III.11) decreases more rapidly as expected. Higher fidelity is achieved when a single entangling gate is applied ($\sim 99.03\%$).

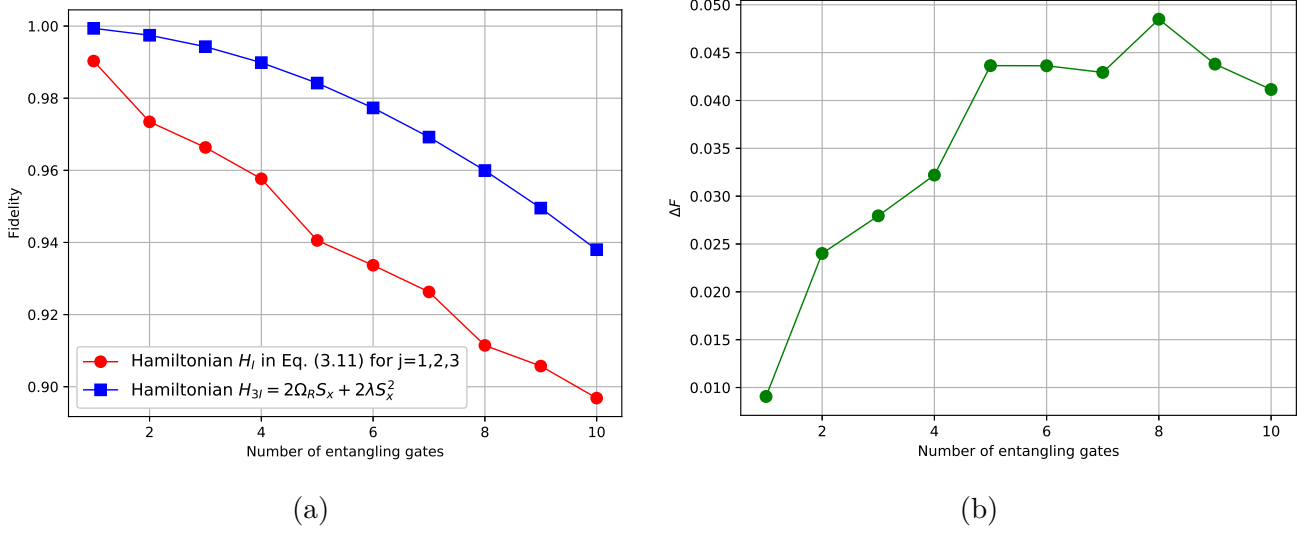


FIGURE III.6 – (Color online) (a) Numerical simulation of the fidelity as a function of the number of entangling gates under both Hamiltonians in equation (III.11) and H_{3I} . (b) A number of entangling operations of the error are caused by decoherence. ΔF denotes the difference of the fidelity for generating GHZ state with and without dissipation[132]. The data parameters used are the same as in figure (III.5a).

For more understanding of the significance of the estimated fidelities, we compare our result to the fidelity obtained from a measurement of GHZ protocols based on the sequence of one- and two-qubit gates. Three-qubit entanglement using superconducting qubits for maximally GHZ-entangled states such as phase qubits[49], containing one- and two-C-Phase-qubit operations, measured to be $F_{GHZ}=87\%$ and transmon qubits[48], containing one- and two-iSWAP-qubit operations, measured to be $F_{GHZ}= 62\%$. The lower fidelities of these protocols compared to our protocol are caused by a longer total period of operations, resulting in decomposing into sequences of one and two iSWAP or C-Phase gates, which leads to destroying the coherence of the system by environmental noise. Our protocol proposal is fast and more efficient especially for complicated quantum circuits because it contains only entangling gate implementation requiring a one-step operation.

Finally, we evaluate the influence of environmental decoherence in generating a GHZ state by comparing the fidelity with and without dissipation. Such a result is shown in Figure (III.6b), in which the difference between the two fidelities is plotted versus the number of gates. As expected, the error due to the decoherence increases with the growing number of entangling gates. The error

caused by the effects of decoherence corresponding to the one entangling gate is around 0.95%.

Important remark : It is important to note that the less sensitive to charge noise for the transmon system the bigger the price to pay which is a reduction in anharmonicity. For this reason, we need a sufficiently large anharmonicity to suppress the transitions to higher transmon levels outside of the two levels $|0\rangle$ and $|1\rangle$. We thus can discuss a rough estimate of the influence of the second excited state $|2\rangle$. In the transmon regime ($E_J \gg E_C$), an approximate estimate of the relative and absolute anharmonicity are $\alpha_r = -(8E_J/E_C)^{-1/2}$ and $\alpha = E_{01}\alpha_r$, respectively[133], with $E_{10} = \sqrt{8E_J E_C} - E_C$ denoted by the energy separation between the levels $|0\rangle$ and $|1\rangle$. We now choose $E_J/E_C = 50$, $E_C = 2\pi \times 2$ GHz, and therefore the absolute anharmonicity is given by $\alpha = -2\pi \times 1.9$ GHz. Assuming the neighbor energy levels are coupled by a microwave driven by Rabi frequency $\Omega_R = 2\pi \times 330$ MHz, the occupation probability of $|2\rangle$ is given by $P_2 \approx 2 / (4 + (\alpha/\Omega_R)^2)$ [93, 134], which is less than 8%. We thus can treat the transmon-type superconducting qubit as a two-level system even in the strong driving regime.

III.5 Chapter summary

In this chapter, based on the multi-qubit device constructed as two and more transmon-type superconducting qubits that are capacitively coupled to a resonator (LC) driven by a strong classical microwave field, we have proposed a faster and more efficient approach showing that the quantum gates or algorithms are realized using only one-step operation. Using this device and approach, we have achieved the two- and three-qubit quantum gates such as the X -rotation gate for creating superposition states and another one called the single-shot entangling gate for generating maximally entangled state. In addition, we suggested the dynamics in open quantum systems of these schemes by estimating the gate fidelities and especially the time evolution of the single-shot entangling gates. High fidelities are achieved to implement our schemes using realistic assumptions about system parameters and the gate time is significantly shorter than the lifetimes of superconducting systems and than most current implementations.

CHAPITRE IV

IMPLEMENTING X -ROTATION GATES IN GROVER'S ALGORITHM AND QUANTUM PROCESS TOMOGRAPHY OF THE ENTANGLING GATES

Searching through large and unsorted databases is a crucial problem with broad applications. The Grover search algorithm is famous and one of the most popular quantum algorithms providing a robust method for quantum computers to accomplish a database search and quadratically overcome nowadays methods in terms of time due to laws of quantum mechanics such as quantum superposition, entanglement, and interference. Additionally, Grover's algorithm is important as it is easy to achieve and is therefore considered as a good algorithm which demonstrates the power of quantum computation.

Many efforts have been devoted to theoretically and experimentally implementing this algorithm in many physical systems, for instance, Nuclear Magnetic Resonance (NMR)[29, 30], trapped ions[31, 33, 34, 135], cavity QED[35, 36, ?, 136], as well as an interesting system about a quantum device consisting of two transmon qubits coupled to a resonator[16, 114]. Recently, Figatt et al [39] experimentally implemented three-qubit Grover's search algorithm using a decomposition of a one-qubit rotation and two-qubit gates with a scalable trapped atomic ion system. The execution of this algorithm for one iteration was done using two methods of the quantum oracle, the Boolean oracle and the phase oracle, which are achieved with a high accuracy of 70.5% fidelity. In the past decades, W L Yang et al[37] used the cavity QED system for implementing Grover's algorithm for three qubits, and subsequently, M Waseem et al [137] proposed a scheme for implementing of same algorithm using four-level SQUID in cavity QED.

In this chapter, we discuss that the Grover's search algorithm can be performed using the

X -rotation gate, which is similar to Hadamard gate as discussed in chapter I. This method is able to find a specific object in an unsorted database of size N using only $O(\sqrt{N})$ operations. We then implement this algorithm using the realization of the X -rotation gate based on the transmon-resonator system for two and three qubits, this gate was realized in the previous chapter. In addition, we fully characterize the performance of the single-shot entangling gate for two and three transmon-type superconducting qubits using quantum process tomography(QPT). The QPT is a useful method for experimentally obtaining a complete implementation of the quantum gate or algorithm, it has been used with superconducting systems for the entangling gate to characterize a square root i -SWAP gate with two qubits[114, 138, 139] and for multi-qubit operations to characterize a Toffoli and C-Phase gates[26, 64], as well as with trapped ions to obtain a complete implementation of two- and three-qubit operations[81, 140, 141].

IV.1 Grover's algorithm with X-rotation gates

In this section, we first discuss Grover's search algorithm for three qubits using X -rotation gates which are similar to the Hadamard gate with a probability higher than 0.94 to find the correct state. Then we generalize the realization of this algorithm for several qubits.

IV.1.1 Three-Qubit Grover's Search Algorithm

Two quantum gates can be used to prepare the states into a quantum superposition, they play a similar role to the Hadamard gate. The first logic gate is the X -rotation gate defined in equation (I.12). While the second gate is the NOT gate defined in Eq.(I.6). So, in the special case when the rotation $\theta = -\pi/2$ is in Eq. I.12, we get

$$R_x\left(-\frac{\pi}{2}\right) = \frac{1}{\sqrt{2}} \begin{pmatrix} 1 & i \\ i & 1 \end{pmatrix}. \quad (\text{IV.1})$$

Then, we can generate the superposition states in the case of three qubits by applying the following operation

$$W_3 = R_x^{\otimes 3}\left(-\frac{\pi}{2}\right) \sigma_x^{\otimes 3}. \quad (\text{IV.2})$$

According to [6], and also the search algorithm discussed in the chapter I, the implementation of Grover's algorithm in the second step an oracle in which we can flip the sign of the desired state

$|x\rangle$ is needed. This can be expressed as

$$|x\rangle \xrightarrow{O} (-1)^{f(x)} |x\rangle, \quad (\text{IV.3})$$

where $f(x) = 1$ if x is the desired state and $f(x) = 0$ otherwise. For the three qubits case the quantum oracle writes[128]

$$O = cP_{ijk} = I - |ijk\rangle \langle ijk|, \quad (\text{IV.4})$$

where $ijk = \{000, 001, 010, 011, 100, 101, 110, 111\}$. As shown in Fig. IV.1, with three qubits initially prepared in the state $|000\rangle$, then these can be prepared in a superposition state by applying the W_3 gate given by equation (IV.2). This operation is followed by the algorithm iteration and must be applied twice. This includes the phase oracle $O = cP_{ijk}$ (Eq. (IV.3)) which allows the inversion of the amplitude of the desired state and the diffusion operator.

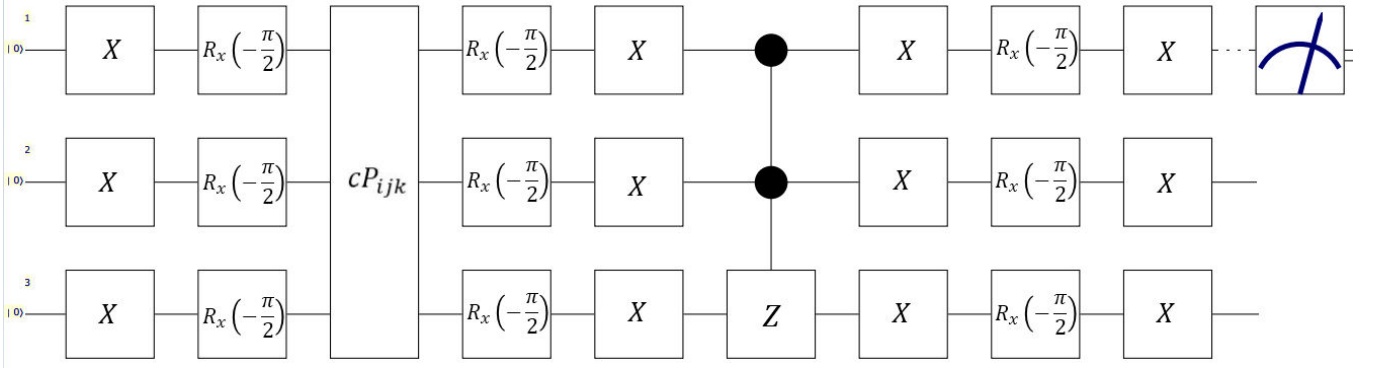


FIGURE IV.1 – Schematic circuit of a three-qubit Grover's algorithm[128].

In figure (IV.2a), it is clear that the probability of finding the desired state by applying the first iteration is $25/32$, whereas the probability of finding the desired state for the second iteration which achieves $121/128$ as depicted in Fig. (IV.2b). We note that similar results were obtained for the other states in the two Grover iterations.

IV.1.2 Grover's Search Algorithm for n -qubit

In the generalized case, searching in an unordered database of N elements (where n is the number of qubits) requires the following steps of Grover's algorithm (see Fig. IV.3) :

1. Starting with the register $|0\rangle^{\otimes n}$.
2. Applying the W_n gate, this operation can map an initial state into a superposition state

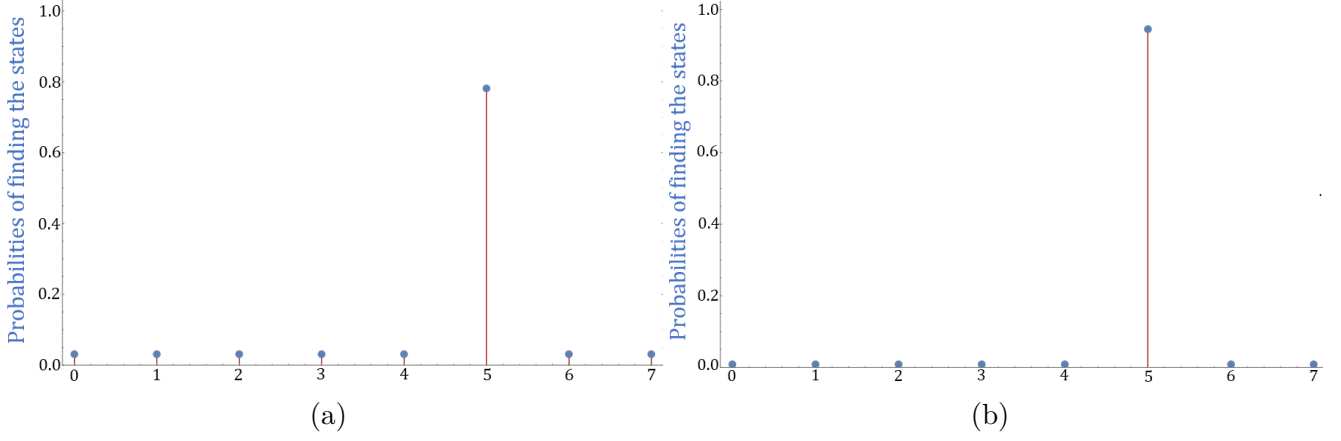


FIGURE IV.2 – (Color online) The probability of finding the state after the first (a) and second (b) Grover's iteration.

$$W_n = R_x^{\otimes n} \left(-\frac{\pi}{2} \right) \sigma_x^{\otimes n}. \quad (\text{IV.5})$$

3. Grover's algorithm iteration can be repeated nearly $(\pi/4) \sqrt{N}$ times :

- a). Applying the quantum oracle as discussed in chapter I.
- b). Applying the diffusion operator.

$$D_n = \sigma_x^{\otimes n} R_x^{\otimes n} \left(-\frac{\pi}{2} \right) \sigma_x^{\otimes n} cP_{\underbrace{111\dots 1}_n} \sigma_x^{\otimes n} R_x^{\otimes n} \left(-\frac{\pi}{2} \right), \quad (\text{IV.6})$$

with $cP_{\underbrace{111\dots 1}_n} = I_n - 2|1\rangle^{\otimes n} \langle 1|^{\otimes n}$.

4. Measurement of the final state.

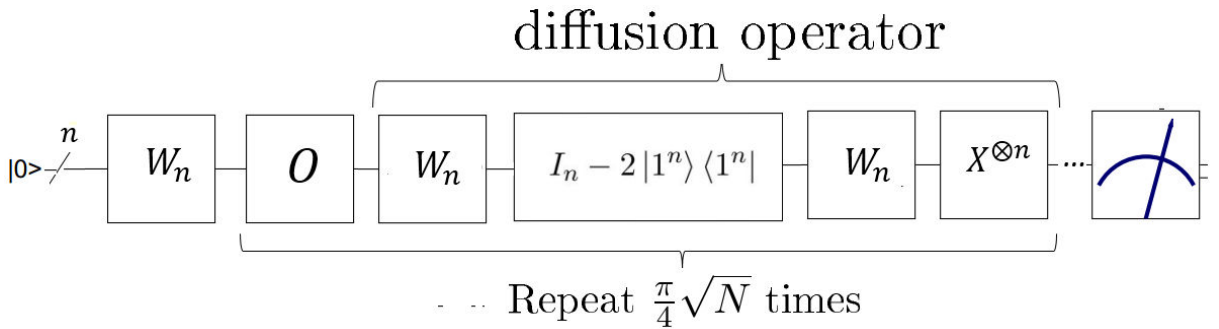


FIGURE IV.3 – Schematic circuit of Grover's algorithm[128].

IV.2 Implementing the X -rotation gate in Grover's search algorithm

In this section, we implement the Grover algorithm with a transmon-resonator system based on two and three-qubit X -rotation gates which were realized in the last chapter using the transmon-resonator system and requiring one-step operations.

IV.2.1 Grover's algorithm for a two-qubit X -rotation gate

We propose a simple scheme of two-qubit Grover's algorithm, shown in figure (IV.4), based on the two-qubit X -rotation gate realized in chapter III (Eq. III.25) and the two-qubit controlled phase gate.

$$cP_{11} = V_2^{-1}U_{11}V_2, \quad (\text{IV.7})$$

where $V_2 = I_2 \otimes W_1$ and U_{11} plays a similar role as a controlled-NOT gate and is given by

$$U_{11} = \begin{pmatrix} 1 & 0 & 0 & 0 \\ 0 & 1 & 0 & 0 \\ 0 & 0 & 0 & -i \\ 0 & 0 & i & 0 \end{pmatrix}, \quad (\text{IV.8})$$

while in order to implement the other oracle operators $cP_{ij} = V_2U_{ij}V_2^{-1}$ (with $ij = \{01, 10, 00\}$), we can also define other operators in terms of the following two-qubit operators

$$U_{01} = \begin{pmatrix} 1 & 0 & 0 & 0 \\ 0 & 1 & 0 & 0 \\ 0 & 0 & 0 & i \\ 0 & 0 & -i & 0 \end{pmatrix}, U_{10} = \begin{pmatrix} 0 & -i & 0 & 0 \\ i & 0 & 0 & 0 \\ 0 & 0 & 1 & 0 \\ 0 & 0 & 0 & 1 \end{pmatrix}, U_{00} = \begin{pmatrix} 0 & i & 0 & 0 \\ -i & 0 & 0 & 0 \\ 0 & 0 & 1 & 0 \\ 0 & 0 & 0 & 1 \end{pmatrix}. \quad (\text{IV.9})$$

To carry out the scheme as shown in Fig. IV.4, we consider the two transmon systems that are initially prepared in state $|00\rangle$. Then, we apply the $\sigma_x^{\otimes 2}$ and $U(\pi/2\lambda)$ [Eq. III.25] operations which prepare the initial states into a superposition state. The obtained state evolves the operations of

figure (IV.4) from left to right looking for the final state. We note that in our scheme only the cP_{ij} operator can change.

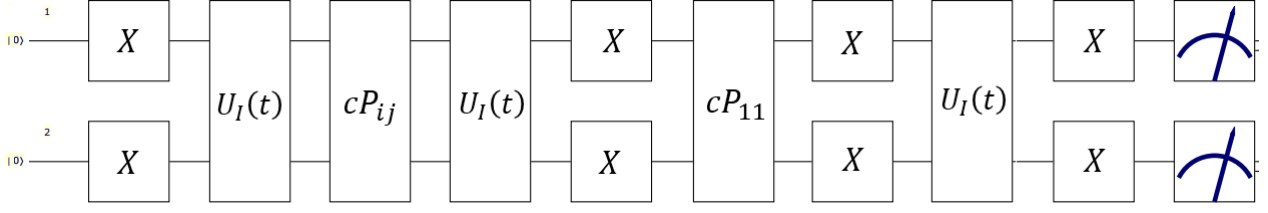


FIGURE IV.4 – Schematic circuit of the two-qubit Grover algorithm[128].

Fidelity and discussion

In order to check the validity of our algorithm for different cases of the quantum oracle shown in Fig. (IV.4), it is necessary to compute the fidelity of finding the target state $|00\rangle$ using the equation (III.22), where $|\psi\rangle$ represents the target state and ρ is the final density matrix obtained without considering the dissipation of our system. The algorithm fidelities for different possible oracles are plotted in Fig. (IV.5). The obtained numerical analysis shows that the algorithm fidelities decrease slightly with increasing values of $b = 2\lambda t$ and are still larger than 90%.

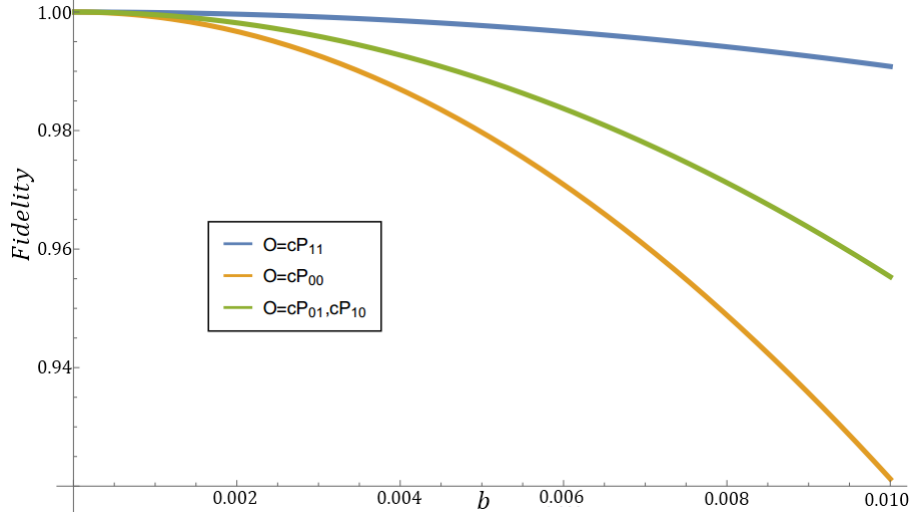


FIGURE IV.5 – Numerical results for the fidelities of two-qubit in Grover algorithm for the four possible oracles as the function $b = 2\lambda t$. These plots are drawn for $\Omega_R/\lambda = 13.5$ [128].

Now, we discuss the experimental realization of the implementation scheme algorithm in Fig. IV.4 for two transmon-type superconducting qubits capacitively coupled to a resonator using the $R_x^{\otimes 2}(-\pi/2)$ gate. The conditional phase gate of the transmon device has been already experimentally realized in Refs.[16]. The lifetime of the transmon device was measured in references[130, 131]. There, the decoherence time $T_1 = 95\mu s$ and the dephasing time $T_2 = 70\mu s$ were reported. We

assume that strong qubit-resonator coupling of $g/2\pi = 220$ MHz, which has been experimentally realized[48]. By assuming that $\Delta_r = 2g$, a direct calculation depicts that the time to perform the three $U_I(t)$ gates is $0.013\mu s$. So, the time of scheme algorithm implementation in Fig. IV.4 is much shorter than the coherence time of the transmon system(T_1 and T_2). Furthermore, we assume that the resonator is driven by a classical microwave field with the frequency of Rabi $\Omega_R/2\pi = 742.5$ MHz and should be adjusted to meet the following condition $\Omega_R/\lambda = (2n + 1)/2$ mentioned above.

IV.2.2 Grover's algorithm for three-qubit X -rotation gate

We here propose a simple scheme for implementing the three-qubit Grover's algorithm as shown in figure (IV.5), based on the three-qubit X -rotation gate and phase gate. In the computational three-qubit basis, the phase oracle was implemented by using the Toffoli gate and the single-qubit X -rotation gate[31]

$$cP_{111} = V_3 U_3 V_3^{-1}, \quad (\text{IV.10})$$

where U_3 plays a similar role to the quantum Toffoli gate, which was achieved using a direct implementation for a superconducting transmon device in Ref. [88], and is given by

$$U_3 = \begin{pmatrix} 1 & 0 & 0 & 0 & 0 & 0 & 0 & 0 \\ 0 & 1 & 0 & 0 & 0 & 0 & 0 & 0 \\ 0 & 0 & 1 & 0 & 0 & 0 & 0 & 0 \\ 0 & 0 & 0 & 1 & 0 & 0 & 0 & 0 \\ 0 & 0 & 0 & 0 & 1 & 0 & 0 & 0 \\ 0 & 0 & 0 & 0 & 0 & 1 & 0 & 0 \\ 0 & 0 & 0 & 0 & 0 & 0 & 0 & -i \\ 0 & 0 & 0 & 0 & 0 & 0 & i & 0 \end{pmatrix}. \quad (\text{IV.11})$$

$$\text{and } V_3 = \begin{pmatrix} 1 & 0 \\ 0 & 1 \end{pmatrix} \otimes \begin{pmatrix} 1 & 0 \\ 0 & 1 \end{pmatrix} \otimes W_1.$$

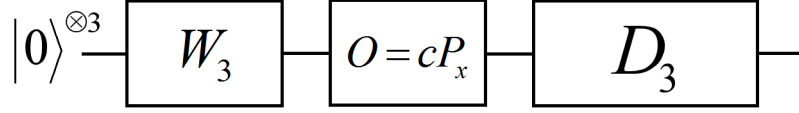


FIGURE IV.6 – Schematic circuit of the three-qubit Grover algorithm[119].

According to reference [39], we can construct the seven other quantum oracles (see Eq. (1.29) in the chapter I) as follows

$$\begin{aligned}
 cP_{000} &= \sigma_{x,3}\sigma_{x,2}\sigma_{x,1}cP_{111}\sigma_{x,1}\sigma_{x,2}\sigma_{x,3}, \\
 cP_{001} &= \sigma_{x,2}\sigma_{x,1}cP_{111}\sigma_{x,1}\sigma_{x,2}, \\
 cP_{010} &= \sigma_{x,3}\sigma_{x,1}cP_{111}\sigma_{x,1}\sigma_{x,3}, \\
 cP_{011} &= \sigma_{x,1}cP_{111}\sigma_{x,1}, \\
 cP_{100} &= \sigma_{x,3}\sigma_{x,2}cP_{111}\sigma_{x,2}\sigma_{x,3}, \\
 cP_{101} &= \sigma_{x,2}cP_{111}\sigma_{x,2}, \\
 cP_{110} &= \sigma_{x,3}cP_{111}\sigma_{x,3}.
 \end{aligned} \tag{IV.12}$$

The quantum circuit of Grover's algorithm shown in Fig. (IV.6) is read from left to right, and the three transmon systems are initially prepared in the state $|000\rangle$. We then apply the quantum gate $W_3 = iU_I(t_R)$ [Eq. III.33] to prepare these qubits in an equal superposition state. This operation is followed by an oracle cP_x , which flips the sign of the correct state's amplitude. The diffusion transform D_3 is given by

$$D_3 = -U_I(t_R)cP_{111}U_I(t_R)\sigma_x^{\otimes 3}. \tag{IV.13}$$

It is worth noting that to implement a three-qubit Grover's search algorithm by using a decomposition into sequences of quantum operations requires nearly more than fifteen one and three-qubit gates[1, 31]. This makes the quantum algorithm complex, and consequently, the gate operation time is quite long and the coherence time of the system would get destroyed by the environmental noise. However, our proposed scheme for implementing Grover's algorithm requires only the single-shot X -rotation gate as well as a three-qubit phase gate. Consequently, it is faster compared to one containing the decomposition of single-qubit gates.

Fidelity and discussion

In order to check the algorithm scheme as shown in Fig. (IV.6), we estimate the algorithm fidelity by using equation (III.22), at which $|\psi\rangle$ and ρ are the target state and the final density matrix, respectively, without taking into account system dissipation. We assume that $|111\rangle$ the target state, the fidelity of the whole scheme shown in Fig IV.6 for all possible oracles [Eqs. (IV.9) and (IV.11)] are plotted in figure (IV.7).

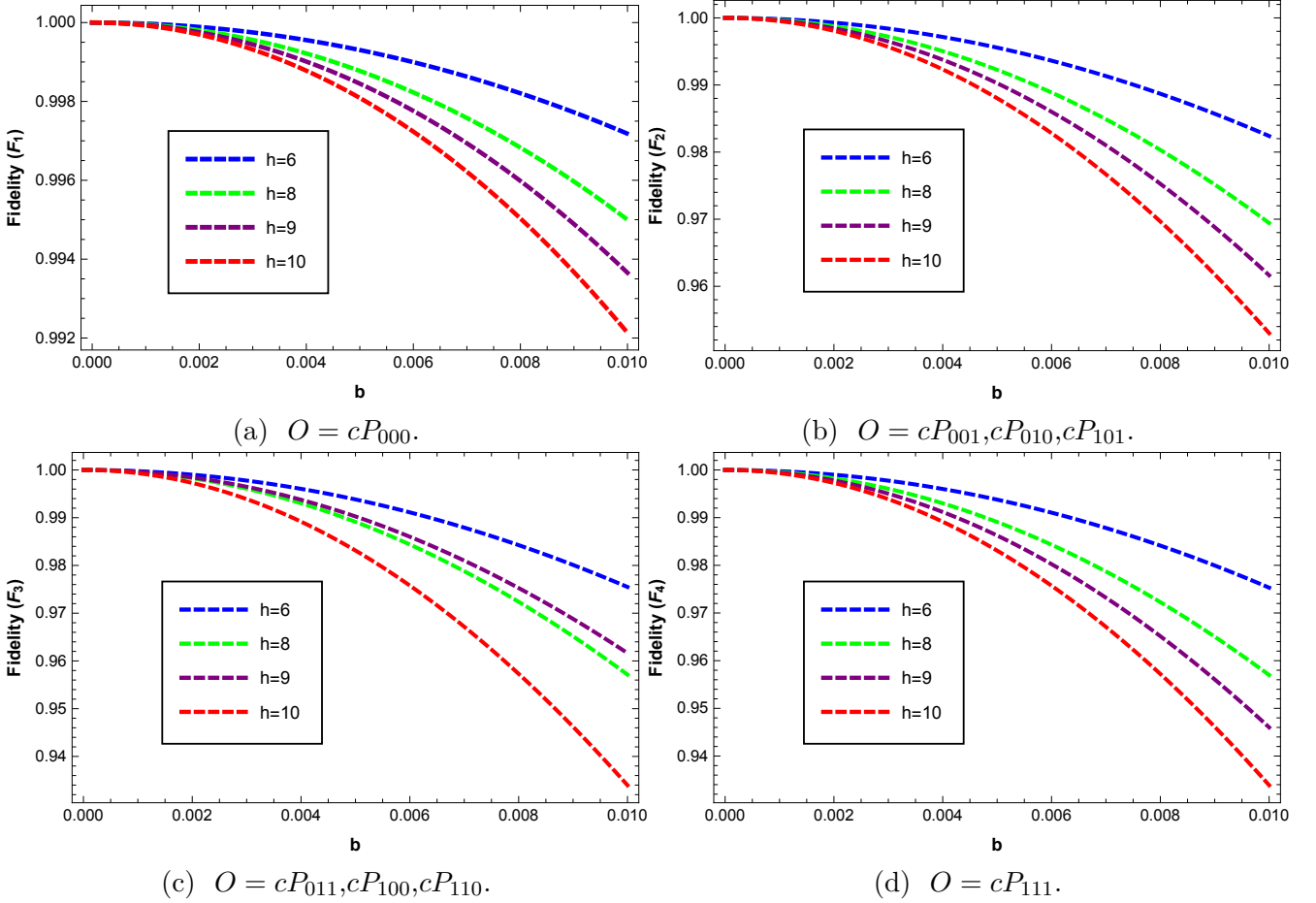


FIGURE IV.7 – Numerical results of the algorithm fidelity for the desired state $|111\rangle$ versus $b = 2\lambda t$ for different values of $h = \Omega_R/\lambda$. Other parameters of the system are referred to in the text. (a) Fidelity F_1 for $O = cP_{000}$. (b) Fidelity F_2 for $O = cP_{001}, cP_{010}, cP_{101}$. (c) Fidelity F_3 for $cP_{011}, cP_{100}, cP_{110}$. (d) Fidelity F_4 for $O = cP_{111}$.

From figure (IV.7), it is clear that our algorithm achieved a high fidelity which decreases slightly while increasing the values of b and increasing values of h . The algorithm fidelity for the ratio ($h \leq 10$) is greater than 93%. Remarkably, from figures IV.7(b) and (c) one can see that the fidelities are nearly unchanged. For the ratio $h = 9$, we get $\Omega_R/2\pi \sim 200$ MHz, $g/2\pi \sim 60$ MHz and $\Delta_r/2\pi \sim 80$ MHz, which were experimentally achieved [118]. These results indicate that the

quantum circuit consisting of the direct implementation of the three-qubit gate is efficient than those using a combination of many one and two-qubit gates. This is caused by the gate time which is quite short compared to the lifetimes of the transmon system.

We briefly discuss some additional though regarding the experimental feasibility of our proposed scheme based on our chosen values for the coherences time of transmon systems, the resonator decay time and the Rabi frequency. The interaction time of the three-qubit X -rotation gate is $t_R = 0.62$ ns. The proposed scheme in figure (IV.3) includes three gates of type $U_I(t_R)$ and two phase gates. Since we can cancel the time of the one-qubit X -rotation gate compared to the Toffoli gate, the time required for the phase gate is the same as that of the Toffoli gate. This result was reported in Ref. [87] and measured to be $t_g = 26$ ns. In the following, the implementation time of Grover's search algorithm for two iterations corresponds to ~ 100 ns, which is shorter than the coherences time of transmon systems (T_1 and T_2) and the resonator decay time used in our numerical simulations. Therefore, the experimental approach of our proposed scheme would be an important step toward quantum computing which is very complicated with the circuits QED.

IV.3 Characterization of the single-shot entangling gate by quantum process tomography

As an essential additional characterization to the results of the two- and three-qubit entangling gate in the last chapter, we here report a complete characterization of the entangling gate for two and three qubits using quantum process tomography (QPT).

IV.3.1 Quantum process tomography (QPT)

QPT is the method used to characterize a quantum logic gate, or quantum algorithm fully [1], it takes an arbitrarily given input state and transforms it into the output state $\rho_{out} = \varepsilon(\rho_{in})$. Reconstructing a completely positive linear map ε representing the process that acts on an arbitrary input state ρ , is the idea behind QPT. Any quantum process for an n -qubit system can be expressed in terms of the Kraus operators as [142, 143]

$$\rho_{out} = \varepsilon(\rho_{in}) = \sum_j^{4^n} \tilde{A}_j \rho_{in} \tilde{A}_j^\dagger, \quad (\text{IV.14})$$

where A_j are the "Kraus operators" of the process ε , which is satisfied by the condition $\sum_j^{4^n} \tilde{A}_j \tilde{A}_j^\dagger = 1$.

If we determine these operators on an operator basis A_a such that $A_i = \sum_a^{4^n} \chi_{i,a} A_a$, then the equation

(IV.14) can be rewritten as

$$\begin{aligned}
 \rho_{out} = \varepsilon(\rho_{in}) &= \sum_i^{4^n} \sum_a^{4^n} \chi_{i,a} A_a \rho_{in} \sum_b^{4^n} \chi_{i,b}^* A_b^+ \\
 &= \sum_{a,b}^{4^n} A_a \rho_{in} A_b^+ \sum_i^{4^n} \chi_{i,a} \chi_{i,b}^* \\
 &= \sum_{a,b}^{4^n} \chi_{a,b} A_a \rho_{in} A_b^+,
 \end{aligned} \tag{IV.15}$$

where $\chi_{a,b} = \sum_i^{4^n} \chi_{i,b} \chi_{i,a}^*$. Whereas equation (IV.15) is the χ -matrix representation of the process in the basis A_a , containing all the information about the quantum process.

IV.3.2 Two-qubit entangling gate characterization

χ -matrix process

Starting from the matrix in equation (III.35) describing the single-shot entangling gate for two qubits, we can show that at the interaction time, the matrix in equation (III.35) becomes

$$U_I\left(\frac{\pi}{4\lambda}\right) = \frac{e^{-i\frac{\pi}{4}}}{\sqrt{2}} \begin{pmatrix} 1 & 0 & 0 & -i \\ 0 & 1 & -i & 0 \\ 0 & -i & 1 & 0 \\ -i & 0 & 0 & 1 \end{pmatrix}, \tag{IV.16}$$

where the overall phase $e^{-i\frac{\pi}{4}}$ can be omitted. On the Pauli basis, the evolution operator $U_I(\pi/4\lambda)$ can be decomposed as $U_I(\pi/4\lambda) = (1/\sqrt{2})(I \otimes I - iX \otimes X)$. leading to readily obtaining the nonzero elements that correspond to the χ_{ideal} process matrix for the perfect $U_I(\pi/4\lambda)$ entangling gate, which are

$$\begin{cases} \chi_{ideal}^{II,II} = \chi_{ideal}^{XX,XX} = 1/2 \\ \chi_{ideal}^{II,XX} = -\chi_{ideal}^{XX,II} = i/2 \end{cases}. \tag{IV.17}$$

We note that this process matrix has only four nonzero elements on the Pauli basis, which is simpler compared to the process matrix of the *CNOT* or *iSWAP* gates, which have sixteen non-null elements on the same basis[62, 76]. As a comparison, we show the absolute values of the

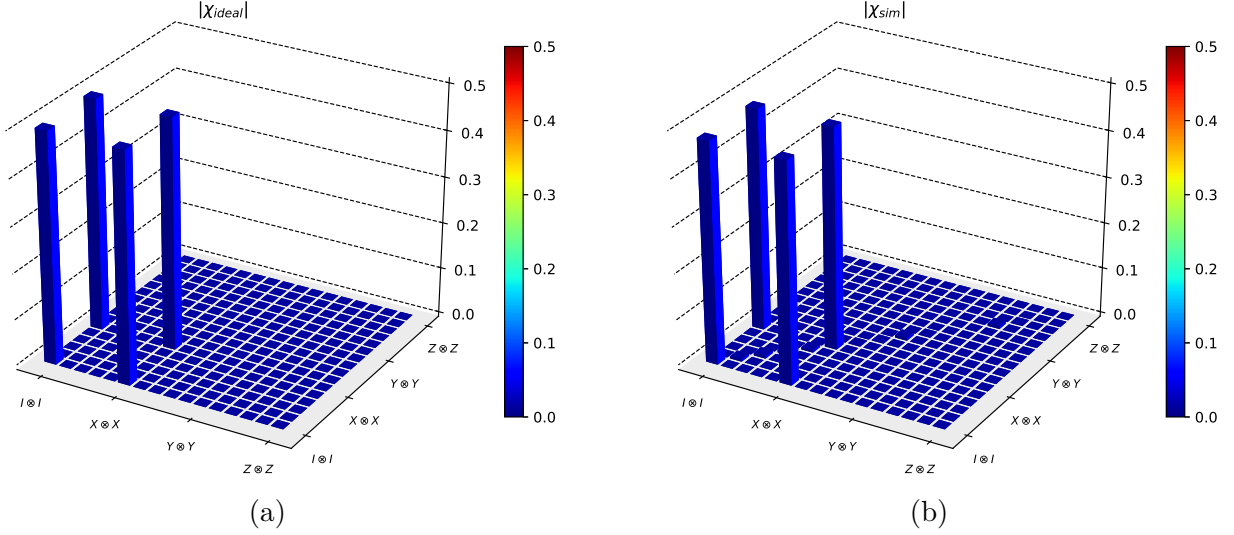


FIGURE IV.8 – *QPT* of the single-shot two-qubit entangling gate. Absolute values of the matrix elements of the χ_{ideal} (a) and the χ_{sim} (b). The matrix elements are shown in the operator basis $\{I \otimes I, I \otimes X, I \otimes Y, \dots, Z \otimes X, Z \otimes Y, Z \otimes Z\}$, where I is identity matrix and $\{X, Y, Z\}$ are the Pauli operators $\{\sigma_x, -i\sigma_y, \sigma_z\}$.

ideal and simulated χ -process matrices in figure (IV.8). Although, we can see some disagreement between the χ_{ideal} [Fig. (IV.8a)] and χ_{sim} [Fig. (IV.8b)] owing to the coupling of transmon systems to their environment. Still, the χ_{sim} process matrix for the entangling gate [Eq. (IV.16)] is in good agreement with the χ_{ideal} . Similar results have been demonstrated with trapped ions[81].

Process fidelity

To quantitatively validate the performance of the two-qubit entangling gate [Eq. IV.15] it is necessary to calculate the process fidelity or mean fidelity using the equation (III.22), with $|\psi\rangle$ as the output state obtained from the perfect unitary map and $\rho = \varepsilon[\rho_{in}]$ of our matrix process which is obtained using numerical simulation. The process fidelity corresponds to the results shown in figure (IV.8) for $T = 20\mu s$ is high 99.9% fidelity.

IV.3.3 Three-qubit entangling gate characterization

χ -matrix process

Starting from the evolution operator in equation (III.36) describing the single-shot entangling gate for three qubits, one can show that at the operation time T , the matrix in equation (III.36)

becomes

$$M(T) = \frac{e^{-i\theta}}{\sqrt{2}} \begin{pmatrix} 1 & 0 & 0 & 0 & 0 & 0 & 0 & -i \\ 0 & 1 & 0 & 0 & 0 & 0 & -i & 0 \\ 0 & 0 & 1 & 0 & 0 & -i & 0 & 0 \\ 0 & 0 & 0 & 1 & -i & 0 & 0 & 0 \\ 0 & 0 & 0 & -i & 1 & 0 & 0 & 0 \\ 0 & 0 & -i & 0 & 0 & 1 & 0 & 0 \\ 0 & -i & 0 & 0 & 0 & 0 & 1 & 0 \\ -i & 0 & 0 & 0 & 0 & 0 & 0 & 1 \end{pmatrix} \quad (\text{IV.18})$$

where the factor $\frac{e^{-i\theta}}{\sqrt{2}}$ denotes the overall phase which can be omitted. This operator in the Pauli basis yields to $U_I(T) = (1/\sqrt{2})(I \otimes I \otimes I - iX \otimes X \otimes X)$. So, therefore, by plugging this expression in Eq. (IV.14) for three qubits systems, we readily obtain the nonzero elements which correspond to the χ_{ideal} matrix for the ideal entangling gate, which are

$$\begin{cases} \chi_{ideal}^{III,III} = \chi_{ideal}^{XXX,XXX} = 1/2 \\ \chi_{ideal}^{III,XXX} = -\chi_{ideal}^{XXX,III} = i/2 \end{cases} . \quad (\text{IV.19})$$

This operation matrix contains only four non-zero matrix elements, which is similar to a two-qubit process case in the last subsection and considerably efficient and faster in terms of simplicity compared to the process analyzed of GHZ-protocol generated from the decomposition of one- and two-qubit operations with nearly sixty-four non-null elements. By comparing the simulated χ_{sim} with the ideal χ_{ideal} matrix process, we plot the absolute values corresponding to these metrics which are depicted in figure (IV.9). It is clear that the χ_{sim} process matrix of the entangling gate for three qubits [Fig. (IV.9a)] is in good agreement with the χ_{ideal} matrix process [Fig. (IV.9b)] with appearing some disagreement which is caused by the coupling of transmon qubits to their environment.

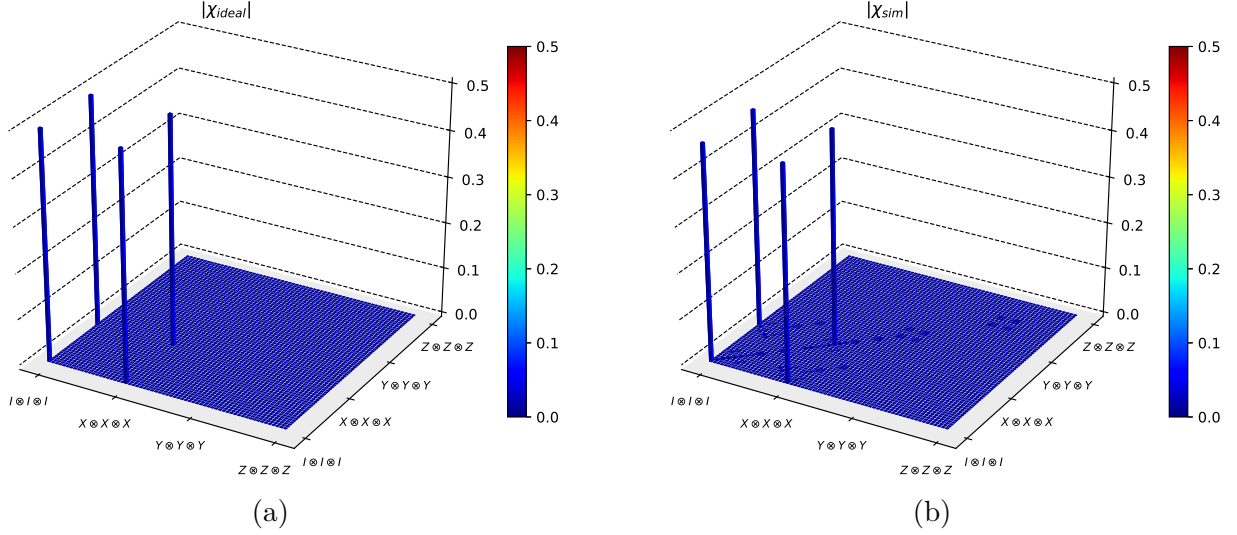


FIGURE IV.9 – QPT of the single-shot entangling gate for three qubits. Absolute values of the matrix elements of the χ_{ideal} (a) and the χ_{sim} (b). The matrix elements are shown in the operator basis $\{I \otimes I \otimes I, I \otimes I \otimes X, \dots, Z \otimes Z \otimes Y, Z \otimes Z \otimes Z\}$, where I is identity matrix and $\{X, Y, Z\}$ are the Pauli operators $\{\sigma_x, -i\sigma_y, \sigma_z\}$.

Process fidelity

In order to estimate the performance of the three-qubit entangling gate $M(T_m)$ in equation (IV.18), we calculate the mean gate fidelity using the same as in the last subsection. The numerical simulations of the process fidelity versus the coherence time T are plotted in Fig. (IV.10), we obtain the fidelity $F_{mean} = 93\%$ which corresponds to the results shown in Fig. (IV.9) for $T = 0.6\mu s$ and can be improved as the coherence time increases.

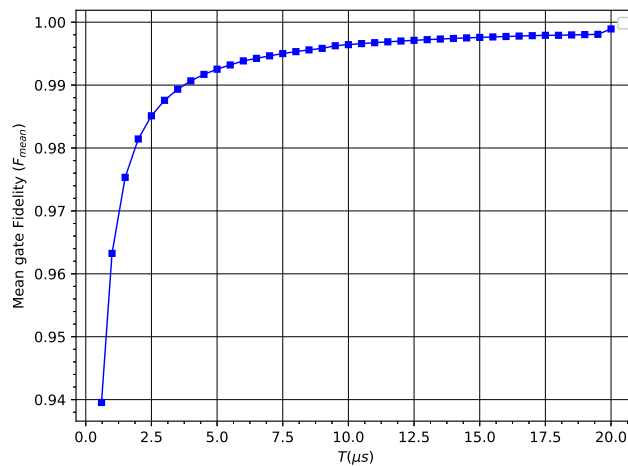


FIGURE IV.10 – Performance of the single-shot entangling gate for three systems. Numerical simulation of the gate fidelity F_{mean} versus the coherence times $T \geq 0.6\mu s$. Assuming that $T = T_1 = T_2$, while the other system parameters are the same as in figure III.6.

IV.4 Chapter summary

In summary, we have generally discussed Grover's search algorithm using the X -rotation gate instead Hadamard gate, this algorithm still meets the requirements of the full Grover algorithm in Ref. [39] as we have demonstrated by the numerical simulations. Using X -rotation gate realized with a transmon-resonator system and requiring only one-step operations as well as the phase gate, we have proposed a practical implementation scheme of a two- and three-qubit Grover's algorithm with an operation time significantly shorter than the coherence time of the used superconducting qubits and resonator decay time. The advantage of this scheme is that it does not need an ancillary qubit and the series of single-qubit gates is also not required. In addition, we have numerically demonstrated the complete characterization of the entangling gate for two and three qubits using a QPT and showed that with higher fidelity.

CHAPITRE V

GENERAL CONCLUSION AND FUTURE DIRECTIONS

Quantum information processing and quantum computation have been a promising and very active area of research, especially in the few years, in quantum science and technology, since the physicist Richard Feynman proposed the idea of simulating quantum systems to build a quantum computer[3]. Recent progress in circuit QED, in which superconducting qubits play the role of atoms in cavity QED, makes it one of the most promising candidates for the realization of quantum information processing (QIP). While to this day, quantum computing with superconducting circuits has been experimentally achieved based on basic single and two-qubit gates, for instance, two-qubit quantum algorithms[16, 114], generation and detection of three and multi-qubit entanglement[48, 49, 50], the implementation of a Toffoli gate for three qubits[64], and realization of three- and multi-qubit quantum error correction[26, 27, 28]. Experimentally, these kinds of realization and implementation approaches led to lower fidelities and required longer execution time due to they are mainly limited by the coherence time of the quantum system, although these fidelities are good to demonstrate simple quantum operations often with up to three qubits, they are too low to allow experiments with more than three qubits to be carried out.

To reduce the excitation time and experimental complications, an efficient approach that will be an alternative is a direct implementation which is an interesting and important topic of a multi-qubit gate and algorithms. In this context, the implementation of a Three-qubit Toffoli gate using a one-step approach is achieved with a high fidelity with up 99%[88, 89, 91]. In this thesis, we have focused on different aspects of quantum computation and, more particularly, realizing quantum gates and algorithms with transmon-type superconducting qubits in open quantum systems using an efficient and alternative approach which is one-step operation.

Before going into the detailed discussion of realizing quantum gates and algorithms with our transmon-resonator system, we have dedicated chapter I of this dissertation to give the basic

concepts of quantum information theory. In Chapter II, we reviewed some superconducting qubits, especially giving a detailed description of the transmon qubit used in this work. We have discussed the basis of the coupling between the transmission line or LC oscillator with transmon-type superconducting qubits in circuit QED. Such circuit QED was associated with a number of key concepts from cavity QED, including some regimes such as the dispersive coupling regime, which is useful for QIP. Furthermore, we also have highlighted the realization of single-qubit gates as well as universal quantum gates for two qubits in the QED circuit needed to build algorithms and create maximally entangled states such as Bell and GHZ states.

In chapter III of this thesis, we have derived the time evolution operator describing our quantum device which involves multi-transmon-type superconducting qubits coupled to one resonator driven by a microwave field. Then, using it, we have suggested a simple and more efficient scheme to realize X -rotation and entangling gates for two and three qubits using a one-step approach. We have demonstrated the robustness of these schemes by simulating the system dynamics in a realistic situation using the master equation for the transmon-resonator system, taking into account the effect of the decoherence of the transmon qubits as well as the resonator decay and a high fidelity is achieved with up to 99%. Finally, these schemes have the following advantages : (i) do not require the combination of the basic gates, for instance, single- and two-qubit gates, (ii) the resonator does not require to be initially prepared in the vacuum state, (iii) our scheme is immune to cavity decay, which makes practical experiments easier. Therefore, we have exploited these schemes to implement Grover's algorithm and we also have fully characterized the single-shot entangling gates using QPT in Chapter IV.

As an essential goal in the future, we will try to implement a high-fidelity universal and multi-qubit gate and also create multiqubit GHZ state based on quantum devices, not only for ones consisting of superconducting qubits coupled to one resonator[16, 26, 88, 89, 91, 114], but for many multi-level systems described as distributed in many cavity systems[144, 145], using the presented approach in this thesis. In addition, this perspective also goes to quantum information processing and its implementation with other physical systems such as superconducting circuits, ion traps, and quantum dots, in cases where the information is encoded in the quantum states of atoms in cavity QED, etc.

Another essential building block of quantum computers is the realization of quantum error correction. In this context, many experiments have been made by realizing schemes of the most basic quantum error correction[1, 22, 23, 24, 25]. One of the most promising fault-tolerant quantum error correction schemes was done using superconducting qubits[146, 147], which are based on two-dimensional surface codes. Recently, quantum error detection code has been experimen-

tally demonstrated based on a physical device consisting of a grid of superconducting coplanar waveguide resonators and four transmon qubits coupled to each of them[26, 27, 28]. The working principle of surface codes would be an interesting step forward for trying to demonstrate simple realizations of such transmon-resonator grid structures.

Finally, we hope that the analysis of the proposed approaches followed throughout this dissertation and their validation using strictly numerical simulations have proven helpful to stimulate experimental activities in the near future in quantum science and technology.

BIBLIOGRAPHIE

- [1] M. A. Nielsen and I. L. Chuang, Quantum Computation and Quantum Information (Cambridge Univ. Press, Cambridge, 2000).
- [2] P. Kaye, R. Laflamme and M. Mosca, An Introduction to Quantum Computing (Oxford Univ. Press, 2007).
- [3] R. P. Feynman. “Simulating physics with computers.” *Int. J. Theor. Phys.*, 21, 467–488 (1982).
- [4] D. Deutsch. “Quantum theory, the Church-Turing principle and the universal quantum computer.” *Proceedings of the Royal Society of London. Series A, Mathematical and Physical Sciences*, 400, 97–117 (1985).
- [5] P. W. Shor. “Algorithms for quantum computation : Discrete logarithms and factoring.” In “*Proceedings, 35th Annual Symposium on Foundations of Computer Science, Santa Fe,*” 124. IEEE Computer Society Press (1994). Cited on page 2.
- [6] Grover, L.K. : Quantum mechanics helps in searching for a needle in a haystack. *Phys. Rev. Lett.* 79, 325–328 (1997).
- [7] J.A. Jones, M. Mosca, Implementation of a quantum algorithm on a nuclear magnetic resonance quantum computer, *J. Chem. Phys.* 109, 1648(1998).
- [8] N. Linden, H. Barjat, R. Freeman, An implementation of the Deutsch–Jozsa algorithm on a three-qubit NMR quantum computer, *Chem. Phys. Lett.* 296, 61–67(1998).
- [9] K. Dorai Arvind, A. Kumar, Implementing quantum-logic operations, pseudopure states, and the Deutsch–Jozsa algorithm using noncommuting selective pulses in NMR, *Phys. Rev. A* 61, 042306(2000).
- [10] J. Kim, J.-S. Lee, S. Lee, C. Cheong, Implementation of the refined Deutsch–Jozsa algorithm on a three-bit NMR quantum computer, *Phys. Rev. A* 62, 022312 (2000).
- [11] T. Mahesh, K. Dorai Arvind, A. Kumar, Implementing logic gates and the Deutsch–Jozsa quantum algorithm by two-dimensional NMR using spin- and transition-selective pulses, *J. Magn. Reson.* 148, 95–103(2001).

- [12] O. Mangold, A. Heidebrecht, M. Mehring, NMR tomography of the three-qubit Deutsch–Jozsa algorithm, *Phys. Rev. A* 70, 042307 (2004).
- [13] S. Gulde, M. Riebe, G.P.T. Lancaster, C. Becher, J. Eschner, H. Häffner, F. Schmidt-Kaler, I.L. Chuang, R. Blatt, Implementation of the Deutsch–Jozsa algorithm on an ion-trap quantum computer, *Nature* 421, 6918(2003).
- [14] S. Takeuchi. “Experimental demonstration of a three-qubit quantum computation algorithm using a single photon and linear optics.” *Phys. Rev. A*, 62, 032301– (2000). Cited on page 3.
- [15] X.-H. Zheng, M. Yang, P. Dong, Z.-L. Cao, Implementing Deutsch–Jozsa algorithm using superconducting qubit network, *Mod. Phys. Lett. B* 22, 3035–3042(2008).
- [16] L. DiCarlo, J. M. Chow, J. M. Gambetta, L. S. Bishop, B. R. Johnson, D. I. Schuster, J. Majer, A. Blais, L. Frunzio, S. M. Girvin, and R. J. Schoelkopf. “Demonstration of two-qubit algorithms with a superconducting quantum processor.” *Nature*, 460, 240–244 (2009).
- [17] Jerry Moy Chow, *Quantum Information Processing with Superconducting Qubits*, 2010.
- [18] L. M. K. Vandersypen, M. Steffen, G. Breyta, C. S. Yannoni, M. H. Sherwood, and I. L. Chuang. “Experimental realization of Shor’s quantum factoring algorithm using nuclear magnetic resonance.” *Nature*, 414, 883 (2001).
- [19] B. P. Lanyon, T. J. Weinhold, N. K. Langford, M. Barbieri, D. F. V. James, A. Gilchrist, and A. G. White. “Experimental demonstration of a compiled version of Shor’s algorithm with quantum entanglement.” *Phys. Rev. Lett.*, 99, 250505 (2007).
- [20] C.-Y. Lu, D. E. Browne, T. Yang, and J.-W. Pan. “Demonstration of a compiled version of Shor’s quantum factoring algorithm using photonic qubits.” *Phys. Rev. Lett.*, 99, 250504 (2007).
- [21] A. Politi, J. C. F. Matthews, and J. L. O’Brien. “Shor’s quantum factoring algorithm on a photonic chip.” *Science*, 325, 1221 (2009).
- [22] D. G. Cory, M. D. Price, W. Maas, E. Knill, R. Laflamme, W. H. Zurek, T. F. Havel, and S. S. Somaroo. “Experimental quantum error correction.” *Phys. Rev. Lett.*, 81, 2152–2155 (1998).
- [23] T. B. Pittman, B. C. Jacobs, and J. D. Franson. “Demonstration of quantum error correction using linear optics.” *Phys. Rev. A*, 71, 052332 (2005).
- [24] J. Chiaverini, D. Leibfried, T. Schaetz, M. Barrett, R. Blakestad, J. Britton, W. Itano, J. Jost, E. Knill, C. Langer, R. Ozeri, and D. Wineland. “Realization of quantum error correction.” *Nature*, 432, 602–605 (2004).

-
- [25] P. Schindler, J. T. Barreiro, T. Monz, V. Nebendahl, D. Nigg, M. Chwalla, M. Hennrich, and R. Blatt. "Experimental repetitive quantum error correction." *Science*, 332, 1059–1061 (2011).
 - [26] M. D. Reed, L. DiCarlo, S. E. Nigg, L. Sun, L. Frunzio, S. M. Girvin, and R. J. Schoelkopf. "Realization of three-qubit quantum error correction with superconducting circuits." *Nature*, 482, 382–385 (2012).
 - [27] C. K. Andersen, A. Remm, S. Lazar, S. Krinner, N. Lacroix, G. J. Norris, M. Gabureac, C. Eichler, and A. Wallraff. "Repeated Quantum Error Detection in a Surface Code." *Nature Physics* 16, 875 (2020).
 - [28] Zhao, Youwei, et al. "Realization of an error-correcting surface code with superconducting qubits." *Phys. Rev. Lett* 129, 030501(2022).
 - [29] I.L.Chuang,N. Gershenfeld, ,M. Kubinec. " Experimental implementation of fast quantum searching." *Phys. Rev. Lett.* 80, 3408–3411 (1998).
 - [30] I.L. Chuang, L.M.K. Vandersypen, X. Zhou, D.W. Leung,S. Lloyd. "Experimental realization of a quantum algorithm." *Nature* 393, 143–146 (1998)
 - [31] M. Feng. "Grover search with pairs of trapped ions." *Phys. Rev. A* 63, 052308 (2001).
 - [32] K.-A. Brickman,P.C. Haljan, , P.J. Lee, M. Acton,L. Deslauriers, C. Monroe. "Implementation of Grover’s quantum search algorithm in a scalable system." *Phys. Rev. A* 72, 050306 (2005).
 - [33] Z.Y. Xu, M. Feng,"Addendum to “Grover search with pairs of trapped ions”." *Phys. Rev. A* 78, 014301 (2008).
 - [34] W.L. Yang, H. Wei, F. Zhou, W.L. Chang, M. Feng. "Solution to the satisfiability problem using a complete Grover search with trapped ions." *J. Phys. B : Atomic, Molecular and Optical Phys.* 42, 145503 (2009).
 - [35] F. Yamaguchi, P. Milman, M. Brune, J.M. Raimond, , S. Haroche. " Quantum search with two-atom collisions in cavity QED." *Phys. Rev. A* 66, 010302 (2002).
 - [36] H. Wang, S. Zhang, K.H. Yeon. "Implementation of Grover quantum search via cavity quantum electrodynamics." *J. Korean Phys. Soc.* 53, 3144–3150 (2008).
 - [37] W.L. Yang, C.Y. Chen, M. Feng. "Implementation of three-qubit Grover search in cavity QED." *Phys. Rev. A* 76, 054301 (2007).
 - [38] M. Hua, M.J. Tao, F.G. Deng. "Fast universal quantum gates on microwave photons with all-resonance operations in circuit QED." *Sci. Rep.* 5, 9274 (2015).
 - [39] C. Figgatt, D. Maslov, K. A. Landsman , N. M. Linke, S. Debnath and C. Monroe. "Complete 3-Qubit Grover search on a programmable quantum computer." *Nat. Commun.* 8, 1918(2017).

- [40] T. P. Orlando, J. E. Mooij, L. Tian, C. H. van der Wal, L. S. Levitov, S. Lloyd, and J. J. Mazo. "Superconducting persistent-current qubit." *Phys. Rev. B* 60, 15398 (1999).
- [41] M. Ansmann, H. Wang, R. C. Bialczak, M. Hofheinz, E. Lucero, M. Neeley, A. D. O'Connell, D. Sank, M. Weides, J. Wenner, A. N. Cleland, and J. M. Martinis. "Violation of Bell's inequality in Josephson phase qubits." *Nature*, 461, 7263(2009).
- [42] Y. Makhlin, G. Scöhn, and A. Shnirman, "Josephson-junction qubits with controlled couplings," *Nature* 398, 305-307(1999).
- [43] J. Koch, T. M. Yu, J. Gambetta, A. A. Houck, D. I. Schuster, J. Majer, A. Blais, M. H. Devoret, S. M. Girvin, and R. J. Schoelkopf. "Charge-insensitive qubit design derived from the Cooper pair box." *Phys. Rev. A* 76, 042319 (2007).
- [44] A. Blais, R.-S. Huang, A. Wallraff, S. M. Girvin, and R. J. Schoelkopf. "Cavity quantum electrodynamics for superconducting electrical circuits : An architecture for quantum computation." *Physical Review A*, 69, 062320 (2004).
- [45] A. Wallraff, D. I. Schuster, A. Blais, L. Frunzio, R.-S. Huang, J. Majer, S. Kumar, S. M. Girvin, and R. J. Schoelkopf. "Strong coupling of a single photon to a superconducting qubit using circuit quantum electrodynamics." *Nature*, 431, 162–167 (2004).
- [46] P. J. Leek, J. M. Fink, A. Blais, R. Bianchetti, M. Göppl, J. M. Gambetta, D. I. Schuster, L. Frunzio, R. J. Schoelkopf, and A. Wallraff. "Observation of Berry's phase in a solid-state qubit." *Science*, 318, 1889 (2007).
- [47] P. J. Leek, M. Baur, J. M. Fink, R. Bianchetti, L. Steffen, S. Filipp, and A. Wallraff. "Cavity quantum electrodynamics with separate photon storage and qubit readout modes." *Phys. Rev. Lett.* 104, 100504 (2010).
- [48] L. DiCarlo, M. D. Reed, L. Sun, B. R. Johnson, J. M. Chow, J. M. Gambetta, L. Frunzio, S. M. Girvin, M. H. Devoret, and R. J. Schoelkopf. "Preparation and measurement of three-qubit entanglement in a superconducting circuit." *Nature*, 467, 574–578 (2010).
- [49] M. Neeley, R. C. Bialczak, M. Lenander, E. Lucero, M. Mariani, A. D. O'Connell, D. Sank, H. Wang, M. Weides, J. Wenner, Y. Yin, T. Yamamoto, A. N. Cleland, and J. M. Martinis. "Generation of three-qubit entangled states using superconducting phase qubits." *Nature*, 467, 570–573 (2010).
- [50] Youpeng Zhong, et al. "Deterministic multi-qubit entanglement in a quantum network." *Nature* 590, 7847 (2021).

-
- [51] M. Baur, A. Fedorov, L. Steffen, S. Filipp, M. P. da Silva, and A. Wallraff. "Benchmarking a quantum teleportation protocol in superconducting circuits using tomography and an entanglement witness." *Phys. Rev. Lett.*, 108, 040502 (2012).
 - [52] Chao Song, et al. "10-qubit entanglement and parallel logic operations with a superconducting circuit." *Phys. Rev. Lett.* 119, 180511(2017).
 - [53] A. Khromova, Ch. Piltz, B. Scharfenberger, T. F. Gloger, M. Johanning, A. F. Var'ón, and Ch. Wunderlich. "Designer spin pseudomolecule implemented with trapped ions in a magnetic gradient." *Phys. Rev. Lett.* 108, 220502 (2012).
 - [54] T. P. Harty, M. A. Sepiol, D. T. C. Allcock, C. J. Ballance, J. E. Tarlton, D. M. Lucas, High-Fidelity Trapped-Ion Quantum Logic Using Near-Field Microwaves, *Phys. Rev. Lett.* 117, 140501 (2016).
 - [55] S. Weidt, J. Randall, S. C. Webster, K. Lake, A. E. Webb, I. Cohen, T. Navickas, B. Lekitsch, A. Retzker, W. K. Hensinger, Trapped-Ion Quantum Logic with Global Radiation Fields, *Phys. Rev. Lett.* 117, 220501 (2016).
 - [56] B. Hacker, S. Welte, G. Rempe, S. Ritter. "A photon–photon quantum gate based on a single atom in an optical resonator." *Nature* 536, 7615 (2016).
 - [57] B.-J. Liu, Z.-H. Huang, Z.-Y. Xue, X.-D. Zhang. "Superadiabatic holonomic quantum computation in cavity qed." *Phys. Rev. A* 95, 062308(2017).
 - [58] L.m.H. Sárkány, J. Fortágh, D. Petrosyan. "Long-range quantum gate via Rydberg states of atoms in a thermal microwave cavity." *Phys. Rev. A* 92 ? 030303(2015)
 - [59] J. L. O'Brien, G. J. Pryde, A. Gilchrist, D. F. V. James, N. K. Langford, T. C. Ralph, and A. G. White, "Quantum process tomography of a controlled-not gate," *Phys. Rev. Lett.* 93, 0805025(2004).
 - [60] T. R. Tan, J. P. Gaebler, R. Bowler, Y. Lin, J. D. Jost, D. Leibfried, D. J. Wineland. "Demonstration of a dressed-state phase gate for trapped ions", *Phys. Rev. Lett.* 110, 263002 (2013).
 - [61] Hongwei Chen, Dawei Lu, Bo Chong, Gan Qin, Xianyi Zhou, Xinhua Peng, Jiangfeng Du. "Experimental demonstration of probabilistic quantum cloning". *Phys. Rev. Lett.* 106, 180404 (2011).
 - [62] A. Dewes, F. R. Ong, V. Schmitt, R. Lauro, N. Boulant, P. Bertet, D. Vion, D. Esteve. "Characterization of a Two-Transmon Processor with Individual Single-Shot Qubit Readout." *Phys. Rev. Lett.* 108, 057002 (2012).

-
- [63] B.C. Hall, Lie Groups, Lie Algebras, and Representations : An Elementary Introduction, Springer, New York, 2015.
 - [64] A. Fedorov, L. Steffen, M. Baur, M. P. da Silva, and A. Wallraff. "Implementation of a toffoli gate with superconducting circuits." *Nature*, 481, 170–172 (2012).
 - [65] M. Mariani, H. Wang, R. C. Bialczak, M. Lenander, E. Lucero, M. Neeley, A. D. O'Connell, D. Sank, M. Weides, J. Wenner, T. Yamamoto, Y. Yin, J. Zhao, and A. N. Cleland. "Photon shell game in three-resonator circuit quantum electrodynamics." *Nat Phys*, 7, 287–293 (2011).
 - [66] Matthias Baur, Realizing Quantum Gates and Algorithms with Three Superconducting Qubits, 2012.
 - [67] E. Schrödinger, *Naturwissenschaften* 23, 807, (1935); *ibid.* 23, 823 (1935); *ibid.* 23, 844 (1935).
 - [68] J. Gruska, Quantum computing, (McGraw-Hill, New York, 1999).
 - [69] D. P. DiVincenzo and P. W. Shor, Fault-Tolerant Error Correction with Efficient Quantum Codes, *Phys. Rev. Lett.* 77, 3260 (1996).
 - [70] J. Preskill, Reliable quantum computers, *Proc. R. Soc. London A* 454, 385 (1998).
 - [71] C.H. Bennett and S. Wiesner, *Phys. Rev. Lett.* 69, 2881 (1992).
 - [72] V. Giovannetti, S. Lloyd, and L. Maccone, "Quantum-enhanced measurements : Beating the standard quantum Limit." *Science* 306, 1330 (2004).
 - [73] Ariel Bendersky, Fernando Pastawski, Juan Pablo Paz. "Selective and efficient estimation of parameters for quantum process tomography." *Phys.Rev. Lett.* 100, 190403 (2008).
 - [74] Christian Tomás Schmiegelow, Miguel Antonio Larotonda, Juan Pablo Paz. "Selective and efficient quantum process tomography with single photons." *Phys. Rev. Lett.* 104, 123601(2010).
 - [75] J. L. O'Brien, G. J. Pryde , A. Gilchrist, D. F. V. James , N. K. Langford , T. C. Ralph and A. G. White. "Quantum Process Tomography of a Controlled-NOT Gate." *Phys. Rev. Lett.* 93, 080502(2004).
 - [76] A. M. Childs, I. L. Chuang and D. W. Leung. "Realization of quantum process tomography in NMR." *Phys. Rev. A* 64, 012314(2001).
 - [77] M. Neeley, M. Ansmann , R. C. Bialczak , M. Hofheinz, N. Katz , E. Lucero , A. O'Connell , H. Wang , A. N. Cleland and J. M. Martinis. "Process tomography of quantum memory in a Josephson-phase qubit coupled to a two-level state" *Nat. Phys.* 4, 523-526(2008).
 - [78] N. Kiesel , C. Schmid , U. Weber, R . Ursin, H. Weinfurter. "Linear optics controlled-phase gate made simple" *Phys. Rev. Lett.* 95, 210505(2005).
-

-
- [79] M. Riebe, K. Kim, P. Schindler, T. Monz , P. O. Schmidt, T. K. K"orber , W. H"ansel, H. H"affner , C. F. Roos, R. Blatt. "Process tomography of ion trap quantum gates" Phys. Rev. Lett. 97, 220407(2006).
 - [80] C. D. Herold, S. D. Fallek , J. T. Merrill, A. M. Meier , K. R. Brown , C. E. Volin, J. M. Amini. "Universal control of ion qubits in a scalable microfabricated planar trap." New J. Phys. 18, 023048(2016).
 - [81] N. Navon, N. Akerman , S. Kotler , Y. Glickman, R. OzeriPhys. "Quantum process tomography of a Mølmer-Sørensen interaction." Rev. A 90, 010103(2014).
 - [82] T. P. Harty, D. T. C. Allcock, C. J. Ballance, L. Guidoni, H. A. Janacek, N. M. Linke , D. N. Stacey, and D. M. Lucas. "High-fidelity preparation, gates, memory, and readout of a trapped-ion quantum bit." Phys. Rev. Lett. 113, 220501 (2014).
 - [83] D. P. DiVincenzo. "Elementary gates for quantum computation." Phys. Rev. A 51, 1015-1022 (1995).
 - [84] K. R. Brown, A. C. Wilson, Y. Colombe , C. Ospelkaus, A. M. Meier, E. Knill, D. Leibfried, and D. J. Wineland. "Single-qubit-gate error below 10^{-4} in a trapped ion." Phys. Rev. A 84, 030303 (2011).
 - [85] J. P. Gaebler, T. R. Tan, Y. Lin, Y. Wan, R. Bowler, A. C. Keith, S. Glancy, K. Coakley, E. Knill, D. Leibfried, and D. J. Wineland. "High-Fidelity Universal Gate Set for ${}^9\text{Be}^+$ Ion Qubits." Phys. Rev. Lett. 117, 060505 (2016).
 - [86] C. J. Ballance, T. P. Harty, N. M. Linke, M. A. Sepiol and D. M. Lucas. "High-fidelity quantum logic gates using trapped-ion hyperfine qubits." Phys. Rev. Lett. 117, 060504 (2016).
 - [87] P. Krantz, M. Kjaergaard, F. Yan, T. P. Orlando, S. Gustavsson and W. D. Oliver. "A quantum engineer's guide to superconducting qubits.." Applied Physics Reviews 6, 021318(2019).
 - [88] Ehsan Zahedinejad, Joydip G hosh, Barry C. Sanders. "High-Fidelity Single-Shot Toffoli Gate via Quantum Control." Phys. Rev. Lett. 114, 200502 (2015).
 - [89] Aneirin J. Baker, Gerhard B. P. Huber, Niklas J. Glaser, Federico Roy, Ivan Tsitsilin, Stefan Filipp, Michael J. Hartmann. "Single shot i-Toffoli gate in dispersively coupled superconducting qubits." Appl. Phys. Lett. 120, 054002 (2022).
 - [90] Yosep Kim, et al. "High-fidelity three-qubit i Toffoli gate for fixed-frequency superconducting qubits." Nature Physics 18, 783-788(2022).
 - [91] S. E. Rasmussen, K. Groenland, R. Gerritsma, K. Schoutens, N. T. Zinner. "Single-step implementation of high-fidelity n-bit Toffoli gates." Phys. Rev. A 101, 022308(2020).
-

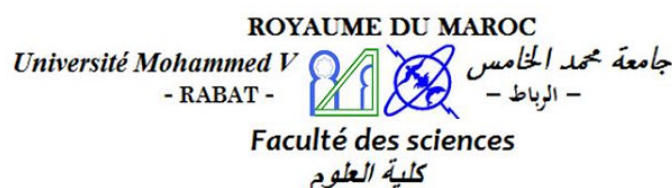
-
- [92] C. P. Yang, and S. Han. "C. P. Yang, and S. Han. " Phys. Rev. A 72, 032311(2005)." Phys. Rev. A 72, 032311(2005).
 - [93] Chui-Ping Yang, Yu-xi Liu, and Franco Nori. "Phase gate of one qubit simultaneously controlling qubits in a cavity." Phys. Rev. A 81, 062323(2010).
 - [94] Chui-Ping Yang, Shi-Biao Zheng, and Franco Nori. "Multiqubit tunable phase gate of one qubit simultaneously controlling n qubits in a cavity." Phys. Rev. A 82, 062326(2010).
 - [95] Chui-Ping Yang, Qi-Ping Su, and Jin-Ming Liu. "Proposal for realizing a multiqubit tunable phase gate of one qubit simultaneously controlling n target qubits using cavity QED" Phys. Rev. A 86, 024301(2012).
 - [96] Chui-Ping Yang, Qi-Ping Su, Feng-Yang Zhang, and ShiBiao Zheng. "Single-step implementation of a multiple-target-qubit controlled phase gate without need of classical pulses." Optics Letters 39, 3312(2014).
 - [97] R. J. Spiteri, M. Schmidt, J. Ghosh, E. Zahedinejad, and B. C. Sanders. "Quantum control for high-fidelity multi-qubit gates." New J. Phys. 20, 113009 (2018).
 - [98] Biaoliang Ye, Zhen-Fei Zheng, and Chui-Ping Yang. "Multiplex-controlled phase gate with qubits distributed in a multicavity system". Phys. Rev. A 97, 062336(2018).
 - [99] Ying-Dan Wang, Stefano Chesi, Daniel Loss, and Christoph Bruder. "One-step multiqubit Greenberger-Horne-Zeilinger state generation in a circuit QED system." Phys. Rev. B 81, 104524(2010)
 - [100] Samuel Aldana, Ying-Dan Wang, and C. Bruder. "Greenberger-Horne-Zeilinger generation protocol for N superconducting transmon qubits capacitively coupled to a quantum bus." Phys. Rev. B 84, 134519 (2011).
 - [101] Z. H. Peng, Yu-xi Liu, Y. Nakamura, and J. S. Tsai. "Fast generation of multiparticle entangled state for flux qubits in a circle array of transmission line resonators with tunable coupling." Phys. Rev. B 85, 024537(2012).
 - [102] Chui-Ping Yang, Qi-Ping Su, Shi-Biao Zheng, and Franco Nori. "Entangling superconducting qubits in a multi-cavity system." New J. Phys. 18, 013025 (2016).
 - [103] Xin Liu, Qinghong Liao, Guangyu Fang, and Shutian Liu. "Dynamic generation of multi-qubit entanglement in the ultrastrong-coupling regime." Sci Rep. 9, 2919 (2019).
 - [104] D. Deutsch and R. Jozsa. "Rapid solution of problems by quantum computation." Proceedings : Mathematical and Physical Sciences, 439, 553–558 (1992).

- [105] B. Perez-Garcia, M. McLaren, S. K. Goyal, R. I. HernandezAranda, A. Forbes, and T. Konrad. "Quantum computation with classical light : Implementation of the Deutsch–Jozsa algorithm." *Phys. Lett. A* 380, 1925 (2016).
- [106] B. D. Josephson. "Possible new effects in superconductive tunnelling." *Physics Letters*, 1, 251–253 (1962).
- [107] P. Anderson and J. Rowell. "Probable observation of the josephson superconducting tunnelling effect." *Phys. Rev. Lett.*, 10, 230 (1963).
- [108] D. E. McCumber. "Effect of ac impedance on dc voltage-current characteristics of superconductor weak-link junctions." *J. Appl. Phys.* 39, 3113–3118 (1968).
- [109] Breuer, Heinz-Peter, and Francesco Petruccione. *The theory of open quantum systems*. Oxford University Press on Demand, 2002.
- [110] M. Büttiker. "Zero-current persistent potential drop across smallcapacitance josephson junctions." *Phys. Rev. B*, 36, 3548–3555 (1987).
- [111] V. Bouchiat, D. Vion, P. Joyez, D. Esteve, and M. H. Devoret. "Quantum coherence with a single Cooper pair." *Phys. Scr.* T76, 165–170 (1998).
- [112] M. Tinkham. *Introduction to Superconductivity*. McGraw-Hill International Editions (1996).
- [113] E. Jaynes and F. Cummings. "Comparison of quantum and semiclassical radiation theories with application to the beam maser." *Proceedings of the IEEE*, 51, 89–109 (1963).
- [114] Andreas Dewes, Romain Lauro, Florian R. Ong, Vivient Schmitt, Perola Milman, Patrice Bertet, Denis Vion, and Daniel Esteve. "Quantum speeding-up of computation demonstrated in a superconducting two-qubit processor." *Phys. Rev. B* 85, 140503((2012)
- [115] M. Mötönen, J. J. Vartiainen, V. Bergholm, and M. M. Salomaa, Quantum Circuits for General Multiqubit Gates, *Phys. Rev. Lett.* 93, 130502 (2004).
- [116] V. V. Shende and I. L. Markov. "On the CNOT-cost of TOFFOLI gates." *Quantum Inf. Comput.* 9, 461 (2009).
- [117] V. M. Stojanovic, A. Fedorov, A. Wallraff, and C. Bruder. "Quantum-control approach to realizing a Toffoli gate in circuit QED." *Phys. Rev. B* 85, 054504 (2012).
- [118] Alexandre Blais, Jay Gambetta, A. Wallraff, D. I. Schuster, S. M. Girvin, M. H. Devoret, and R. J. Schoelkopf. "Quantum-information processing with circuit quantum electrodynamics." *Phys. Rev. A* 75, 032329(2007).
- [119] H Sakhouf, M Daoud and R Ahl Laamara. "Simple scheme for implementing the Grover search algorithm with superconducting qubits." *J. Phys. B : At. Mol. Opt. Phys.* 54 175501(2021).

-
- [120] J. M. Fink, R. Bianchetti, M. Baur, M. Goppl, L. Steffen, S. Filipp, P. J. Leek, A. Blais and A. Wallraff. "Dressed collective qubit states and the Tavis-Cummings model in circuit QED." *Phys. Rev. Lett.* 103, 083601(2009).
 - [121] Z. J. Deng, M. Feng, and K. L. Gao. "Simple scheme for the two-qubit Grover search in cavity QED." *Phys.Rev. A* 72, 034306(2005).
 - [122] Shi-Biao Zheng. "Generation of entangled states for many multilevel atoms in a thermal cavity and ions in thermal motion." *Phys. Rev. A* 68, 035801(2003).
 - [123] GuiLong Gao, GenChang Cai, ShouSheng Huang, LongYing Tang, WenJing Gu, MingFeng Wang, NianQuan Jiang. " $1 \rightarrow N$ quantum controlled phase gate realized in a circuit QED system." *Sci. China Phys. Mech. Astron.* 55, 1422-1426(2012).
 - [124] A. Sørensen and K. Mølmer. "Quantum computation with ions in thermal motion." *Phys. Rev. A* 62, 022311 (2000).
 - [125] S. Haroche and J.-M. Raimond. *Exploring the Quantum : Atoms, Cavities and Photons.* Oxford University Press, 2006.
 - [126] J. R. Johansson, P. D. Nation, and F. Nori, "QuTiP : An open-source Python framework for the dynamics of open quantum systems", *Comp. Phys. Comm.* 183, 1760 (2012).
 - [127] J. R. Johansson, P. D. Nation, and F. Nori, "QuTiP 2 : A Python framework for the dynamics of open quantum systems", *Comp. Phys. Comm.* 184, 1234 (2013).
 - [128] H. Sakhouf, M. Daoud, R.A. Laamara. "Implementation of Grover's Search Algorithm in the QED Circuit for Two Superconducting Qubits." *Int J Theor Phys* 59, 3436–3448 (2020).
 - [129] M. Baur, S. Filipp, R. Bianchetti, J.M. Fink, M. Goppl, L. Steffen, P.J. Leek, A. Blais, A. Wallraff. "Measurement of Autler-Townes and Mollow transitions in a strongly driven superconducting qubit." *Phys. Rev. Lett.* 102, 243602 (2009).
 - [130] D. I. Schuster, A. A. Houck, J. A. Schreier, A. Wallraff, J. M. Gambetta, A. Blais, L. Frunzio, B. Johnson, M. H. Devoret, S. M. Girvin, et al. "Resolving photon number states in a superconducting circuit." *Nature* 445, 515 (2007).
 - [131] Jerry M. Chow, Jay M. Gambetta, Easwar Magesan, David W. Abraham, Andrew W. Cross, B.R. Johnson, Nicholas A. Masluk, Colm A. Ryan, John A. Smolin, Srikanth J. Srinivasan, and M. Steffen. "Implementing a strand of a scalable fault-tolerant quantum computing fabric." *Nat. Commun.* 5, 4015 (2014).
 - [132] Hamid Sakhouf, Mohammed Daoud, and Rachid Ahl Laamara. "Quantum process tomography of the single-shot entangling gate with superconducting qubits." *J. Phys. B : At. Mol. Opt. Phys.* 56, 105501(2023).
-

- [133] J. Koch, T. M. Yu, J. Gambetta, A. A. Houck, D. I. Schuster, J. Majer, A. Blais, M. H. Devoret, S. M. Girvin, and R. J. Schoelkopf. "Suppressing charge noise decoherence in superconducting charge qubits." *Phys. Rev. A* 76, 042319 (2007).
- [134] Chui-Ping Yang. "Quantum information transfer with superconducting flux qubits coupled to a resonator." *Phys. Rev. A* 82, 054303(2010). .
- [135] K. A. Brickman, P. C. Haljan, P. J. Lee, M. Acton, L. Deslauriers, and C. Monroe. "Implementation of Grover's quantum search algorithm in a scalable system." *Phys. Rev. A* 72, 050306 (2005).
- [136] T. Sleator and H. Weinfurter. "Realizable universal quantum logic gates." *Phys. Rev. Lett.* 74, 4087 (1995)
- [137] M. Waseem, R. Ahmed, M. Irfan, and S. Qamar. "Three-qubit Grover's algorithm using superconducting quantum interference devices in cavity-QED." *Quantum Inf. Process.* 12, 3649-3664(2013).
- [138] R. C. Bialczak, M. Ansmann, M. Hofheinz, E. Lucero, M. Neeley, A. D. O'Connell, D. Sank, H. Wang, J. Wenner, M. Steffen, A. N. Cleland and J. M. Martinis. "Quantum process tomography of a universal entangling gate implemented with Josephson phase qubits." *Nature Phys.* 6, 409(2010).
- [139] A. G. Kofman and A. N. Korotkov. "Two-qubit decoherence mechanisms revealed via quantum process tomography." *Phys. Rev. A* 80, 042103(2009).
- [140] Holly N Tinkey, Adam M Meier, Craig R Clark, Christopher M Seck , and Kenton R Brown. "Quantum process tomography of a Mølmer-Sørensen gate via a global beam." *Quantum Sci. Technol.* 6, 034013(2021).
- [141] T. Monz, K. Kim, W. Hansel, M. Riebe, A. S. Villar, P. Schindler, M. Chwalla, M. Hennrich, and R. Blatt. "Realization of the quantum Toffoli gate with trapped ions." *Phys. Rev. Lett.* 102, 040501 (2009).
- [142] I. L. Chuang and M. A. Nielsen. "Prescription for experimental determination of the dynamics of a quantum black box." *J. Mod. Opt.* 44, 2455 (1997).
- [143] G. M. D'Ariano and P. Lo Presti. "Quantum tomography for measuring experimentally the matrix elements of an arbitrary quantum operation." *Phys. Rev. Lett.* 86, 4195-4198(2001).
- [144] Tong Liu, Qi-Ping Su, Yu Zhang, Yu-Liang Fang, and Chui-Ping Yang. "Generation of quantum entangled states of multiple groups of qubits distributed in multiple cavities." *Phys. Rev. A* 101, 012337 (2020)

- [145] Chui-Ping Yang, Qi-Ping Su, Yu Zhang, and Franco Nori. "Implementing a multi-target-qubit controlled-NOT gate with logical qubits outside a decoherence-free subspace and its application in creating quantum entangled states." *Phys. Rev. A* 101, 032329 (2020).
- [146] D. P. DiVincenzo. "Fault-tolerant architectures for superconducting qubits." *Phys. Scr.*, 2009, 014020 (2009).
- [147] A. Y. Kitaev. "Fault-tolerant quantum computation by anyons." *Annals of Physics*, 303, 2 – 30 (2003).



CENTRE D'ETUDES DOCTORALES - SCIENCES ET TECHNOLOGIES

Abstract

This thesis focuses on quantum information processing using the superconducting device, especially, on realizing quantum gates and algorithms in open quantum systems. Such a device is constructed by transmon-type superconducting qubits coupled to a superconducting resonator. For the realization of quantum gates and algorithms, a one-step approach is used. We suggest faster and more efficient schemes for realizing X -rotation and entangling gates for two and three qubits. During these operations, the resonator photon number is canceled owing to the strong microwave field added. They do not require the resonator to be initially prepared in the vacuum state and the scheme is insensitive to resonator decay. Furthermore, the robustness of these operations is demonstrated by including the effect of decoherence of transmon systems and the resonator decay in a master equation, high fidelity will be achieved on quantum simulation. In addition, Using the implemented x -rotation gates as well as phase gates, we present an alternative way for implementing Grover's algorithm for two and three qubits, which does not require a series of single gates. As well, we demonstrate by numerically simulating the use of quantum process tomography to fully characterize the performance of a single-shot entangling gate for two and three qubits and obtaining the process fidelities greater than 93%. These gates are used to create Bell and Greenberger-Horne-Zeilinger (GHZ) entangled states.

Keywords : Quantum information processing and computation, Quantum gates, Grover's search algorithm , Entangling gates, Bell and GHZ states , High fidelity, superconducting circuits.

Résumé

Cette thèse se concentre sur le traitement de l'information quantique à l'aide d'un dispositif supraconducteur, en particulier sur la réalisation de portes quantiques et d'algorithmes dans des systèmes quantiques ouverts. Un tel dispositif est construit par des qubits supraconducteurs de type transmon couplés à un résonateur supraconducteur. Pour la réalisation des portes quantiques et des algorithmes, une approche en une seule étape est utilisée. Nous proposons des schémas plus rapides et plus efficaces pour réaliser des portes de X -rotation et des portes d'enchevêtrement pour deux et trois qubits. Au cours de ces opérations, le nombre de photons du résonateur est annulé en raison du fort champ de micro-ondes ajouté. Elles ne nécessitent pas que le résonateur soit initialement préparé dans l'état de vide et les schémas est insensible à la désintégration du résonateur. En outre, la robustesse de ces opérations est démontrée en incluant l'effet de la décohérence des systèmes transmon et la désintégration du résonateur dans une équation maîtresse, ce qui permet d'obtenir une grande fidélité dans la simulation quantique. En outre, en utilisant les portes de X -rotation mises en œuvre ainsi que les portes de phase, nous présentons une autre façon de mettre en œuvre l'algorithme de Grover pour deux et trois qubits qui ne nécessite pas une série de portes simples. En outre, nous démontrons en simulant numériquement l'utilisation de la tomographie des processus quantiques pour caractériser pleinement la performance d'une porte d'enchevêtrement à un seul coup pour deux et trois qubits et nous obtenons des fidélités de processus supérieures à 93%. Ces portes sont utilisées pour créer des états intriqués de Bell et de Greenberger-Horne-Zeilinger (GHZ).

Keywords : Quantum information processing and computation, Quantum gates, Grover's search algorithm , Entangling gates, Bell and GHZ states , High fidelity, superconducting circuits.

Année Universitaire : 2022/2023